Long-baseline Sterile Neutrino Searches in the NOvA Experiment

Thesis submitted to
Cochin University of Science and Technology
in partial fulfillment of the requirements
for the award of the degree of

DOCTOR OF PHILOSOPHY
under the Faculty of Science

by

Sijith E
Department of Physics
Cochin University of Science and Technology
Kochi - 682022

March 2020

Long-baseline Sterile Neutrino Searches in the NOvA Experiment
Ph. D. thesis in the field of High Energy Physics

Author

Sijith E
Department of Physics
Cochin University of Science and Technology
Kochi - 682022
sedayath@fnal.gov, sijithnambiar@gmail.com

Research Supervisors

Dr. Ramesh Babu T
(Supervising Guide)

Dr. Alexander I Himmel
(Joint Guide)

Front cover : NOvA Detector PVC Cell

"All truths are easy to understand once they are discovered; the point is to discover them."

-Galileo Galilei

CERTIFICATE

Certified that the work presented in this thesis entitled "**Long-baseline Sterile Neutrino Searches in the NOvA Experiment"** is based on the bonafide record of research work done by Sijith E., under our guidance in the Department of Physics, Cochin University of Science and Technology, Cochin 682 022 and at Fermi National Accelerator Laboratory, Batavia, IL, USA, 60510 in partial fulfillment of the requirements for the award of degree of Doctor of Philosophy and has not been included in any other thesis submitted for the award of any degree. All the relevant corrections and modifications suggested by the audience during the pre-synopsis seminar and recommendations by doctoral committee of the candidate have been incorporated in the thesis.

Kochi
March, 2020

Dr. Ramesh Babu T
(Supervising Guide)

Batavia, IL
March, 2020

Dr. Alexander I Himmel
(Joint Guide)

DECLARATION

I hereby declare that the work presented in this thesis is based on the original research work done by me under the guidance of Dr. Ramesh Babu T, Department of Physics, Cochin University of Science and Technology, Cochin-682022, India, and Dr. Alexander I Himmel, Fermi National Accelerator Laboratory, Batavia, IL, USA-60510 and has not been included in any other thesis submitted previously for the award of any degree.

Kochi
March, 2020

Sijith E

Contents

Acknowledgements

I would like to thank each and every kind person who helped me directly or indirectly to reach at this point. First and foremost, I would like to thank my supervisor Dr. Ramesh Babu T, without his constant support and encouragement I could not have completed my research. I would like to thank my Fermilab supervisor, Dr. Alexander I Himmel for motivating me a lot. He contributed a lot in shaping the experimental physicist in me. Thank you for spending time for me in his busy schedule. I would like to thank Dr. Louise Suter, who was my sterile group convener. She was so kind to spend time to discuss various aspects of the analysis and was unhesitatingly helping me whenever I was in need.

I am very thankful to Prof. Brajesh Chandra Choudhary, the spokesperson of IIFC-Fermilab collaboration, for providing me all necessary support to do research at Fermilab. He treated me like his own student and supported me a lot. I would like to thank Dr. Alexandre Bruno Sousa, Dr. Adam Aurisano and Dr. Gavin Davies for supporting me as my NC/sterile group conveners. I really enjoyed working with Dr. Gavin Davies and his constant support and fruitful suggestions helped me to complete my analysis. I gratefully remember awesome talks with Dr. Sousa about neutrinos and beyond. I am very thankful to Dr. Adam Aurisano for introducing me to the NC/sterile analysis. I thank Dr. Michel Wallbank for working with me. I would like to thank Dr. Peter Shanahan and John W. Cooper for the nice hospitality and helps they provided me at Fermilab.

I also want to thank the Department of Science and Technology, India, Fermilab and NOvA collaborators and all members of collaborating Indian Institutions, for their help and support. My special acknowledgement to late Dr. Rajendra raja for making this collaboration possible for CUSAT. I am thankful to Prof. Titus K Mathew and Dr. M.R Anantharaman for the support they have provided as my co-principle investigators in the DST project. I am thankful to the Prof. M. K Jayaraj, previous department heads, all the teaching and non-teaching staff of CUSAT physics department.

I would like to thank my Fermilab friends whose company was a great relaxation in the middle of the stressful analysis deadlines. I am thankful to my friends and fellow research scholars at CUSAT physics department, whose support was a great help for me. Finally, I would like to thank my

mother, father, sister for the shower of love and care on me. I would like to thank my wife for her love and immense patience.

Abstract

Experimental high energy physics constitutes the experimental investigation of the fundamental building blocks of matter and radiation and their interactions. These fundamental building blocks are classified as bosons and fermions. Neutrinos are fermions that come under the lepton category. According to the Standard Model of particle physics, they are massless, neutral particles that interacts with matter only through weak force and comes in three different flavors. Neutrinos exhibit a characteristic property, known as the neutrino oscillation. Neutrino oscillation is the the change of neutrino from one flavor to another flavor as they propagates in space. This phenomenon is only possible if the neutrinos are massive.

The reported anomalous result from LSND and MiniBooNE experiments demanded the existence of a fourth kind of neutrino, at the same time, LEP experimental result confirms that only three active neutrino can exist. So if they exists, this fourth kind of neutrino can't interact through weak force or they can be called as sterile neutrino. Some of the experiments favored the existence of sterile neutrinos, at the same time, there are some other experiments that disfavors their existence. So the search for the sterile neutrinos is very active in the field of experimental neutrino physics.

NOvA is a long-baseline experiment with two functionally identical detectors, a Near Detector (ND) at Fermilab and a Far Detector at Ash River, Minnesota which is 810 km far away from the ND. They are off-axis detectors that lie 14.6 mrad off from the beam axis. This enables the detector to receive a neutrino beam with energy peak at 2 GeV. The NOvA experiment is designed to run with both the neutrino beam and antineutrino beam and NOvA has the potential to search for the existence of sterile neutrinos. This thesis is based on the sterile neutrino search by looking at the depletion of the neutral-current (NC) energy spectrum of neutrinos at the FD. Since NC events are not sensitive to three flavor oscillation, any depletion of NC events at the FD indicates the existence of sterile neutrinos.

Chapter–1

This chapter consists of a brief summary of neutrino physics. This includes the stories of the discovery of neutrinos, it's flavors and the idea of neutrino mass. Neutrino oscillation and a theoretical formulation of

the neutrino oscillation probability is also included. A section that talks about the current landscape of neutrino oscillation is also supplemented. Last section talks about anomalous experimental results that demands the existence of neutrinos beyond the standard model prediction and the formulation of the neutrino oscillation probability with four-flavor hypothesis. This chapter ends with a brief introduction of the neutral-current (NC) disappearance analysis in NOvA.

Chapter–2

This is a small chapter that introduces NOvA detector. It has a dedicated section for NuMI beam and explains how the neutrino and antineutrino beams are produced. It also explains the significance of the off-axis position of NOvA detectors.

Chapter–3

Calibration of the detectors and the event reconstruction are explained in this chapter. It starts with a section that explains the need for calibrating NOvA detectors. The absolute calibration, relative calibration and timing calibration are explained in this chapter. Attenuation correction and threshold corrections are also detailed as a sub-section of the attenuation calibration. The NOvA event reconstruction is explained step-by-step in this chapter, that includes the density based clustering, hough transform, vertex finding algorithm using elastic arms and Fuzzy-k prong reconstruction.

A brief note on the NOvA simulation is added as the second part of this chapter. These simulation includes flux simulation, interaction simulation and detector simulation.

Chapter–4

This chapter is dedicated to the particle identification (PID) used in the NOvA NC disappearance analysis. The primary event selector in the NOvA ND is the computer vision based particle identifier termed as CVN, which primarily separates the neutral current (NC) events from the charged current (CC) events. Since our FD is at the ground surface, it is subjected to a huge cosmic background. TMVA based Cosmic rejection BDT is used as a PID in the NOvA FD, along with the CVN. Training, testing and implementation of cosmic rejection BDT is explained here.

The invariant mass of π^0 can be used as a standard candle for the calibration of NOvA detectors. In the FD, we used π^0's with cosmic origin to find its invariant mass. A separate section is dedicated to elaborate this

analysis which is carried out by the author.

Chapter–5

This chapter explains the event selection procedure used in both neutrino and antineutrino analysis. It explains different layers of selection cut applied to reduce the background events to get the pure NC sample for the analysis. The efficiency and purity of the selection is plotted.

Chapter–6

The systematic uncertainties in both neutrino and antineutrino analyses are explained in this chapter. Details are given for how each systematic uncertainty is quantified. The major and minor systematic uncertainties in both analyses are listed.

Chapter–7

The neutrino and antineutrino long-baseline NC disappearance analyses are explained in detail. The extrapolation technique used for both analyses are explained in detail. The data/MC ratio of the ND is used to correct the FD prediction. This helped us to reduce the systematic uncertainty that effect both detectors similarly. Next section is talking about the cross-checks like the side-band studies that are used to determine the robustness of the predicted spectra. In this study, events outside our analysis region is compared with the data and MC distributions to see how well we modeled our prediction.

Chapter–8

This thesis is based on the NC disappearance sterile neutrino search at the FD with 8.85×10^{20} POT (Protons-On-Target) equivalent of neutrino data and 12.5×10^{20} POT equivalent of antineutrino data. This chapter explains the last stage of the analysis; looking at the data spectrum to see how well it matches with the simulated spectrum. The fitting procedure implemented to draw the contour in θ_{24} and θ_{34} plane is explained here. A brief note on the Feldman-Cousins contour correction technique is included.

Chapter–9

Conclusions and a note on future plans for the long-baseline sterile neutrino searches in NOvA are put here, with a mention of the ND-FD joint fit analysis.

Publications

- M. A Acero,..., S. Edayath et al., (NOvA Collaboration), Search for multi-messenger signals in NOvA coincident with LIGO/Virgo detections (Submitted to PRD, arXiv:2001.07240 (20 January 2020))
- M. A Acero,..., S. Edayath et al., (NOvA Collaboration), First measurement of neutrino oscillation parameters using neutrinos and antineutrinos by NOvA, (Phys. Rev. Lett.123, 151803 (2019))
- M. A Acero,..., S. Edayath et al., (NOvA Collaboration), Observation of seasonal variation of atmospheric multiple-muon events in the NOvA Near Detector (Phys. Rev. D 99, 122004 (2019))
- M. A Acero,..., S. Edayath et al., (NOvA Collaboration), New constraints on oscillation parameters from ν_e appearance and ν_μ disappearance in the NOvA experiment, (Phys. Rev. D 98, 032012 (2018))
- P. Adamson,..., S. Edayath et al., (NOvA Collaboration), Search for active-sterile neutrino mixing using neutral-current interactions in NOvA (Phys. Rev. D 96, 072006)
- P. Adamson,..., S. Edayath et al., (NOvA Collaboration), Constraints on Oscillation Parameters from ν_e Appearance and ν_μ Disappearance in NOvA (Phys. Rev. Lett. 118(2017) No-23, 231801)
- P. Adamson,..., S. Edayath et al., (NOvA Collaboration), Measurement of the neutrino mixing angle θ_{23} in NOvA (Phys. Rev. Lett. 118(2017) No-15, 151802)
- M. A Acero,..., S. Edayath et al., (NOvA Collaboration), Measurement of Neutrino-Induced Neutral-Current Coherent π^0 Production in the NOvA Near Detector (arXiv:1902.00558v3 (28 May 2019))
- Sijith Edayath et al., Sterile neutrino search in the NOvA Far Detector (arXiv:1710.01280v1 (3 Oct 2017))

Conference Talks & Posters

- Sijith E, "Long-baseline Sterile Neutrino Searches in the NOvA Experiment", DAE-BRNS High Energy Physics Symposium 2018 at IIT Chennai (Conference Talk).
- Sijith E, "Long Base-Line Sterile Neutrino Searches in NOvA", Fermilab Users Meeting, Fermilab, USA (June 6-8, 2018) (Poster).
- Sijith E, "Planned Improvements to the NOvA sterile neutrino NC Disappearance analysis" American Physical Society Meeting , at Columbus, Ohio (April 2018) (Conference Talk).
- Sijith E, "Search for the Sterile Neutrino in the NOvA Experiment", 10th International Neutrino Summer School 2017 (INSS 2017), August 7, 2018, Fermilab, USA (Poster).
- Sijith E et al., "Sterile Neutrino Search in the NOvA Far Detector", American Physical Society DPF Meeting, Fermilab, USA, August 2017 (Poster).
- Sijith E, "Sterile Neutrino search in the NOvA Far Detector", New Perspectives, June 5- 6 , Fermilab, USA (2017) (Conference Talk).
- Sijith E, "Sterile neutrino search in the NOvA Far-Detector through Neutral current disappearance channel", New Perspectives 2017, Fermilab, USA (Conference Talk).
- Sijith E, "Cosmic pi0 mass reconstruction in the NOvA Far Detector", American Physical Society Meeting , at Washington D.C. (2017) (Conference Talk).

List of Tables

List of Figures

1

Neutrinos - Introduction

Neutrinos are one of the profuse particles in the universe. They are also mysterious, as they interact feebly with the matter, it is extremely difficult to detect them. Moreover, they travel nearly with the velocity of light and billions of neutrinos are passing through our body in every second. The neutrinos can have solar, astrophysical, cosmic, or reactor origin. This "ghost" particle first came into light when Wolfgang Pauli proposed it in 1930 as a solution to the β–decay puzzle [1].

The β–decay puzzle was one of the major scientific challenges in the early 20th century. The observed continuous energy spectrum of β–decay (electrons emitted from an atomic nucleus) did not agree with the general energy-momentum conservation principle. If β–decay was just a process in which an atomic nucleus with mass A and atomic number Z transforms into a new nucleus with atomic number $Z+1$ and mass number A by the emission of an electron, then the emitted electron should have definite energy. But the observed β–decay spectra is continuous [2] with a maximum value equal to

$$Q = [(M_{A,Z} - M_{A,Z+1}) - m_e]\, c^2. \tag{1.1}$$

Where $M_{A,Z}$ is the mass of the initial nucleus, $M_{A,Z+1}$ mass of the final nucleus, m_e is the mass of the emitted electron and Q is the total energy released in this process.

W. Pauli put forward a solution for the β–decay puzzle by proposing a hypothetical neutral particle that participates in the β–decay by sharing some of the energy from the emitted electron. Italian physicist Enrico Fermi also formulated a theory to explain β–decay [3, 4]. His formulation was inspired by W. Pauli's idea. He considered the nucleus a bound state of protons and neutrons. The introduction of neutrons explained the ob-

served nuclear spin. The theory proposed that the β–decay happens when a neutron (n) inside a nucleus decays into a proton (p), an electron (e^-) and a particle that is analogous to the particle proposed by earlier by W. Pauli.

$$n \rightarrow p + e^- + \overline{\nu}. \tag{1.2}$$

The hypothetical particle was assumed to be tiny, neutral and having a spin 1/2. He named the particle as "neutrino" (in Italian, the word "neutrino" stands for "little neutral one") and was represented by the Greek letter "ν" (where $\overline{\nu}$ is its antiparticle). With the help of this formulation, he could explain the continuous β-decay spectra and thus the energy conservation law was rescued. The undetectable neutrino shares the energy of the emitted electron this leads to the observed continuous electron energy spectrum.

1.1 Neutrinos and their Flavors

In a Nobel prize-winning discovery by Reines and Cowan in 1956 [5], the neutrino produced in a nuclear reactor was first detected through an inverse β-decay process. Since the neutrino was produced along with an electron, it was termed as an electron neutrino.

After 6 years, a group of scientists in Brookhaven National Laboratory discovered a different kind of neutrino [6]. That neutrino was distinct on having different flavor from the neutrino discovered by Reines and Cowan [7]. This neutrino was produced along with the muon, not with the electron. So that kind of neutrino was named as muon neutrino. The 1998 Nobel Prize was awarded to Leon Lederman, Schwartz and Steinberger for confirming the existence of muon neutrino. Now there are three known charged lepton generations: the electron, muon and tau leptons. Analogous to the three generations of charged leptons, the existence of three generations of neutrinos was assumed for the sake of symmetry. The Fermilab experiment DONUT (Direct Observation of NU Tau) discovered the tau neutrino in 2000 [8]. By fitting the predicted number of active neutrinos to the CERN Large Electron-Positron collider experiment data, the existence of only three neutrino flavor was confirmed [9].

1.2 Neutrino Oscillation - The Identity Exchange

Neutrinos exist in three distinct flavors: electron (ν_e), muon (ν_μ) and tau (ν_τ). The standard model of particle physics treats neutrinos as massless particles. In the 1950s, Burno Pontecorvo proposed the idea that neutrinos could have mass [10, 11]. With a basic quantum mechanical treatment, he explained how a neutrino that travels a distance can be transformed into a new species. The existence of neutrino mass is essential to formulate the neutrino oscillation [12]. Extending the Pontecorvo's formulation, Maki, Nakagawa, and Sakata put forward a formulation for the neutrino oscillation. They treated neutrino oscillation as a pure quantum mechanical process and expressed the neutrino flavor eigenfunctions as a superposition of neutrino mass eigenfunctions [13]. When a neutrino interacts with a particle, it would be in its flavor eigenstate. But when it propagates from one point to another point in space, the neutrino would be in its mass eigenstate. We will discuss neutrino oscillation in detail in Sec. 1.4. Two big ongoing puzzles in particle physics were explained with the help of the neutrino oscillation phenomena.

1.2.1 Solar Neutrino Puzzle

The Homestake experiment gave the first experimental evidence for the neutrino oscillation. The detector principle was based on the electron neutrino capture by chlorine [14].

$$\nu_e + {}^{37}\mathrm{Cl} \rightarrow {}^{37}\mathrm{Ar} + e^-. \tag{1.3}$$

The argon produced as a result of this interaction was used as a probe for finding the number of electron neutrino interactions that occurred. A huge tank, having an approximate volume of 400 m^3, filled with C_2Cl_4 was placed around 1.5 km below the ground in Homestake gold mine. Ray Davis and John Bahcall measured the rate of solar electron neutrinos. The experiment was sensitive to the ν_e's from the solar ^{8}B decay [15]. They observed a deficit of neutrino interactions in the detector while comparing with the predicted event rate [16]. This deficit in experimentally observed event rate was termed as "solar neutrino problem" or "solar neutrino puzzle" [17], Many other experiments that were using

other detector techniques also reported this deficit. The Japanese neutrino experiment, Kamiokande used the water Cherenkov detector and the Photomultiplier Tubes (PMTs) is one example. Soviet-American Gallium Experiment (SAGE) [18] and the Gallium Experiment (GALLEX) [19] are some other examples.

1.2.2 The Atmospheric Neutrino Puzzle

High energy cosmic ray particles collide with atmospheric gases to form hadronic shower. These showers are mostly pions with a small kaon component. Since they are unstable particles, they decay to form secondary particles. Pions decay into muons and muon neutrinos. These muons eventually decays to electrons and electron neutrinos. Kaons can also decay into neutrinos. The predominant pion decay is illustrated below:

$$\pi^- \rightarrow \mu^- + \overline{\nu}_\mu, \tag{1.4}$$

$$\mu^- \rightarrow \nu_\mu + \overline{\nu}_e + e^-. \tag{1.5}$$

The atmospheric neutrino experiments measured a ratio of the total number of muon neutrinos to the total number of electron neutrinos [20], which was calculated to be 2. The atmospheric neutrino experiments like the Irvine-Michigan-Brookhaven (IMB) [21] detector, Kamiokande-II [22] and Soudan-2 [23] showed a deficit in experimental value while comparing with the prediction. This is known as the atmospheric neutrino puzzle.

1.2.3 Solving the Puzzles

The theoretical formulation of neutrino oscillation was published by that time [10] and that was the key idea used to solve the solar and atmospheric neutrino puzzles. The observed data deficit was explained as, some of the neutrinos change their flavor while traveling to the detector. Neutrinos will be in the flavor eigenstate as they are produced and then they propagate as mass eigenstates. The flavor eigenstates are responsible for their interaction with other particles.

1.3 Neutrino Mass as a Key to Beyond Standard Model

The immediate consequence of the neutrino oscillation is the assumption that neutrinos possess mass. Neutrino mass is the key idea that leads us to a regime beyond the standard model predictions.

1.3.1 Standard Model of Particle Physics

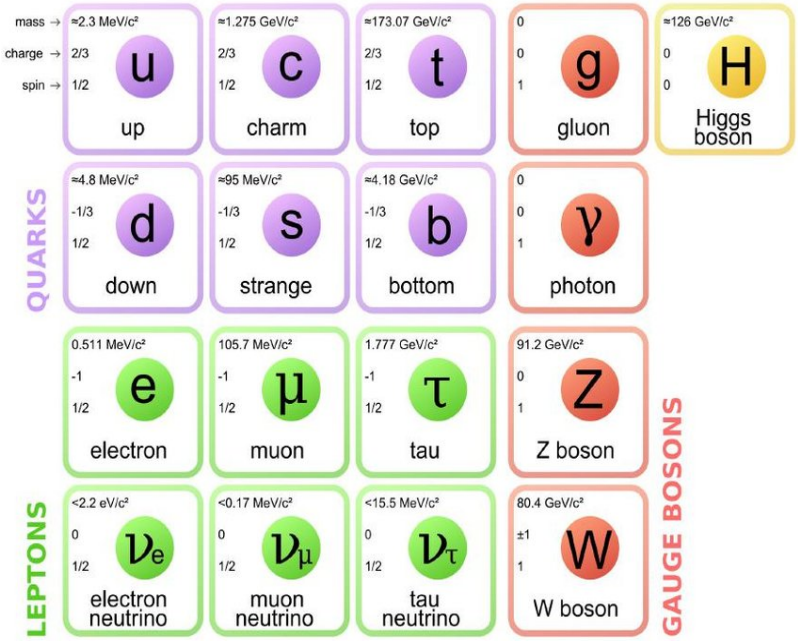

Figure 1.1: A representation of the standard model of particle physics. All particles and force carriers are categorized as quarks, leptons and gauge bosons respectively. This figure is adapted from Ref. [24].

The standard model reveals the fundamental building blocks of the universe as shown in Fig. 2.1. It is a very successful theory in the sense that it is capable of providing an explanation to almost all of the high energy physics phenomena that have been observed in the laboratory. It was successful in predicting many particles that were observed later in various experiments. But it has some limitations too, such as its inability to

explain neutrino oscillations which makes us think beyond the standard model [25]. The standard model divides all the matter and interaction forces between them into two categories – fermions and bosons. All constituent particles of matter belong to a category called fermions. These fermions interact with each other by the exchange of force carriers namely bosons. These fermions include particles called quarks and leptons. A total of 6 quarks and 6 leptons are included in this collection. Higg's bosons are responsible for providing mass to other particles. The electrons, muons and tau particles along with their corresponding neutrinos form the leptons. Four fundamental force carriers are also included. Photons are responsible for the electromagnetic force, gluons for the strong force and the $W^{\pm}$ and Z^0 bosons for the weak force.

Among these, the three neutrinos namely electron neutrino (ν_e), muon neutrino (ν_μ) and tau neutrino (ν_τ) interact only by the weak interaction.

1.3.2 A Brief History of the Weak Interaction

The story of the theory of weak interaction starts from Fermi's formulation of β-decay. He postulated that the weak interaction take part in the β-decay as contact interactions of fermions such as an electron, proton, neutron, and neutrino. The matrix element for the β-decay can be written as,

$$M = G\left(\bar{\psi}_n \gamma^\mu \psi_p\right)\left(\bar{\psi}_\nu \gamma_\mu \psi_e\right). \tag{1.6}$$

Where G is coupling constant and ψ_i is Dirac spinor with i=n, p, ν, and e are particle taking part in the interaction. This formulation needed a modification when parity was found to be not conserved in the weak interaction. This was first reported by Chein Shiung Wu and collaborators while studying the decay of Cobalt-60 [26].

This demands some modifications to the Fermi's theory. The modification is done by introducing a V–A type potential into the Lagrangian of the weak interaction, where V denotes vector current and A stands for the axial vector current [27, 28]. Later Sheldon Glashow, Abdus Salam, and Steven Weinberg modified the theory in order to address the non-renormalizable behavior in the relativistic quantum field theory regime [29]. The new renormalizable V–A theory introduced heavy bosons such as $W^{\pm}$, Z^0 as the carriers of weak interaction between particles. The masses of the exchange bosons $W^{\pm}$ and Z^0 were first measured at the UA1 [30] and UA2 [31] experiments at the $p\bar{p}$ collider at CERN.

1.3.3 Going Beyond the Standard Model - Neutrino Mass

In the standard model, quarks and charged leptons are treated as massive Dirac particles where as neutrinos are treated as massless Dirac particle. The Lagrangian for a Dirac field can be written as,

$$L = \bar{\psi}\left(i\gamma^{\mu}\partial_{\mu} - m\right)\psi. \tag{1.7}$$

Here ψ is the Dirac spinor field and $\bar{\psi}$ is its adjoint. When the neutrino mass is zero, the Lagrangian can be written as,

$$L = \bar{\psi}\left(i\gamma^{\mu}\partial_{\mu}\right)\psi. \tag{1.8}$$

From this, the Weyl equation of motion can be obtained as,

$$i\gamma^{\mu}\partial_{\mu}\psi = 0. \tag{1.9}$$

A general fermion field can be represented $\psi = \psi_L + \psi_R$, where ψ_L is the left chiral field and ψ_R is the right chiral[1] field. For particles with non-zero mass, the mass term in the Dirac Lagrangian (the last term in the Eqn. 1.7) can be written in terms of ψ_L and ψ_R as,

$$m\bar{\psi}\psi = m\left(\bar{\psi_L}\psi_R + \bar{\psi_R}\psi_L\right). \tag{1.10}$$

Which gives us the flexibility that if the mass of the particle is zero, then it is not necessary for the ψ_R and ψ_L to exist simultaneously.

This makes room for us to accommodate the experimental result of not observing any right-handed neutrino. If such a right-handed neutrino is present, it should not be capable of interacting with other particles through weak, strong or electromagnetic interaction– termed as the sterile neutrino [32]. The "minimally extended standard model" rewrite the right-handed neutrino into the formalism. From Eqn. 1.10, it is clear that the existence of right-handed neutrinos is necessary to have the Dirac mass for the neutrinos. Mass in the standard model is generated by interaction with the Higg's field.

There is a possibility that neutrinos can be its own antiparticles. The theoretical explanation comes along with the introduction of neutrino as a

[1] A chirality matrix is defined as $\gamma^5 = i\gamma^0\gamma^1\gamma^2\gamma^3$, where γs are the Dirac γ matrices. It has properties: $\gamma^5\psi_{\mathrm{R}} = \psi_{\mathrm{R}}$ and $\gamma^5\psi_{\mathrm{L}} = -\psi_{\mathrm{L}}$

Majorana particle. The Majorana particle on charge conjugation operation becomes the same particle. This implies that the Majorana particles are their own antiparticles. The *see-saw mechanism* gives a reasonable explanation for the observed smallness of neutrino mass. If the left-handed neutrino is light, then the right-handed neutrino will be massive. Since the right-handed neutrino does not interact with matter, it can be massive leaving the light interactive left-handed neutrinos. This subsection is adapted from the Ref.[25].

1.4 Neutrino Oscillation Formalism

According to the Maki-Nakagawa-Sakata neutrino oscillation formulation [13], neutrinos interact with matter in its flavor eigenstate. Each of these flavor eigenstate can be written as a linear combination of the mass eigenstates. We represent a neutrino flavor eigenstate as $|\,\nu_a\rangle$. Each neutrino emerges out from a charged current interaction (mediated by $W^{\pm}$ boson) with a lepton counterpart accompanying it. In order to conserve the lepton quantum number, electrons are produced with electron neutrino, muons with muon neutrino and tau neutrino with tau particle. If we take $|\,\nu_l\rangle$ as the mass eigenstate of the free Hamiltonian each flavor eigenstate, $|\,\nu_a\rangle$ can be written as,

$$|\,\nu_a\rangle = \sum_l U^*_{al}\,|\,\nu_l\rangle. \tag{1.11}$$

Here U_{al} is the elements of an unitary matrix, using which we can implement the change of basis, ie. we can represent a flavor eigenstate as a linear combination of mass eigenstates and also a mass eigenstate as a linear combination of flavor eigenstates. This matrix is known as the PMNS matrix, named after Pontecorvo, Maki, Nakagawa, and Sakata. We now consider the simplest case of neutrino oscillation that happens in the vacuum. Here neutrinos are treated as plane waves. Suppose at a time t=0, a neutrino is created at a particular point $x = 0$, in the flavor eigenstate, $|\,\nu_a\rangle$. Since this is a superposition of mass eigenstates, this state evolves with time in vacuum in terms of mass eigenstates, $|\,\nu_l\rangle$ as follows:

$$|\,\nu_a(t)\rangle = \sum_l U^*_{al} e^{-i(E_l t - p_l.x)}\,|\,\nu_l\rangle. \tag{1.12}$$

The plane wave travels with a velocity very close to the light velocity. Following the natural units in the formalism ($\hbar = c = 1$), after plane wave

travels a distance $x = L$ in a time t, we can replace t with L and the $p_l.x$ in the exponent the of Eqn. 1.12 can be replaced with $p_l L$. With the assumption that all neutrino mass eigenstate possess same energy ($E = E_l$), p_l can be simplified as, $p_l = \sqrt{E^2 - m_l^2} \approx E - m_l^2/(2E)$. With this the Eqn. 1.12 can be written as,

$$|\,\nu_a(L)\rangle = \sum_l U_{al}^* e^{-im_l^2 L/(2E)}\,|\,\nu_l\rangle. \tag{1.13}$$

Since the PMNS matrix is unitary, $|\,\nu_l\rangle$ can be written in terms of flavor eigenstates, $|\,\nu_b\rangle$ by inverting Eqn. 1.11 and we obtain

$$|\,\nu_l\rangle = \sum_b U_{bl}\,|\,\nu_b\rangle \tag{1.14}$$

where $b = e, \mu, \tau$. Substituting Eqn. 1.14 in Eqn. 1.13 we can get

$$|\,\nu_a(L)\rangle = \sum_{b=e,\mu,\tau} \left(\sum_l U_{al}^* e^{-im_l^2 L/(2E)} U_{bl} \right) |\,\nu_b\rangle. \tag{1.15}$$

In order to find the probability of a neutrino flavor a to transform into another flavor b after traveling a distance L, we can take inner product of $|\,\nu_b\rangle$ and $|\,\nu_a(L)\rangle$, and we obtain

$$\langle\nu_b\,|\,\nu_a(L)\rangle = \sum_b \sum_l U_{al}^* U_{bl} e^{-im_l^2 L/(2E)} \langle\nu_a\,|\,\nu_b\rangle. \tag{1.16}$$

With the help of orthogonality relation for flavor eigen states, the flavor transition amplitude is obtained as,

$$\langle\nu_b\,|\,\nu_a(L)\rangle = \sum_l U_{al}^* U_{bl} e^{-im_l^2 L/(2E)}. \tag{1.17}$$

The modulus square of the flavor transition amplitude, $\langle\nu_b\,|\,\nu_a(L)\rangle$ gives us the transition probability:

$$P\left(\nu_a \to \nu_b\right) = |\langle\nu_b\,|\,\nu_a\left(L\right)\rangle|^2 = \sum_{l,j} U_{al}^* U_{bl} U_{aj} U_{bj}^* e^{-i(m_l^2 - m_j^2)L/(2E)}. \tag{1.18}$$

This can be rearranged as,

$$P\left(\nu_a \to \nu_b\right) = \sum_{l,j} U_{al}^* U_{bl} U_{aj} U_{bj}^* + \sum_{l,j} U_{al}^* U_{bl} U_{aj} U_{bj}^* (e^{-i(m_l^2 - m_j^2)L/(2E)} - 1). \tag{1.19}$$

Using the properties of unitary matrices, $\sum_j U_{aj}U^*_{bj} = \delta_{ab}$ and the relation $\Delta^2_{lj} = m^2_l - m^2_j$, Eqn.(1.19) can be written as,

$$P\left(\nu_a \to \nu_b\right) = \delta_{ab} + \sum_{l=1,j=1}^{n} U^*_{al}U_{bl}U_{aj}U^*_{bj}(e^{-i\Delta m^2_{lj}L/(2E)} - 1). \qquad (1.20)$$

We now have to make use of some identity to further simplify Eqn. 1.20. At first, $l = j$ makes the second term on the right hand side of Eqn. 1.20 equals to zero and $l < j$ will be the complex conjugate of $i > j$. Using $\Re(z)$ to denote the real part of a complex number, z the Eqn. 1.20 becomes

$$P\left(\nu_a \to \nu_b\right) = \delta_{ab} + 2\sum_{i>j} \Re\left(U^*_{al}U_{bl}U_{aj}U^*_{bj}(e^{-i\Delta m^2_{lj}L/(2E)} - 1)\right). \qquad (1.21)$$

We can further simplify the Eqn. 1.21 with the definition,

$$\zeta = U^*_{al}U_{bl}U_{aj}U^*_{bj}(e^{-i\Delta m^2_{lj}L/2E} - 1)$$

and $\psi = \Delta m^2_{lj}L/2E$. For this consider the following:

$$\Re(\zeta) = \Re(U^*_{al}U_{bl}U_{aj}U^*_{bj}(e^{-i\psi} - 1)). \qquad (1.22)$$

With the help of the identity $e^{-i\psi} = \cos\psi - i\sin\psi$ and $\cos\psi$ – 1= – $2\sin^2\psi/2$, the Eqn. 1.22 can be written as,

$$\Re(\zeta) = \Re\left(U^*_{al}U_{bl}U_{aj}U^*_{bj}(-2\sin^2\psi/2 - i\sin\psi)\right). \qquad (1.23)$$

Now separating the real and imaginary parts of the Eqn. 1.23 we can get

$$\Re(\zeta) = -2\Re\left(U^*_{al}U_{bl}U_{aj}U^*_{bj}\right)\sin^2\psi/2 + \mathrm{Im}\left(U^*_{al}U_{bl}U_{aj}U^*_{bj}\right)\sin\psi \qquad (1.24)$$

where $\mathrm{Im}(z)$ denotes the imaginary part of a complex number, z. Now substituting Eqn. 1.24 to Eqn. 1.21, we finally get

$$P\left(\nu_a \to \nu_b\right) = \delta_{ab} - 4\sum_{l>j} \Re(U^*_{al}U_{bl}U_{aj}U^*_{bj})\sin^2\Delta_{lj} + 2\sum_{l>j} \mathrm{Im}(U^*_{al}U_{bl}U_{aj}U^*_{bj})\sin 2\Delta_{lj}. \qquad (1.25)$$

with $\Delta_{lj} = \Delta m^2_{lj}L/\left(4E\right)$.

From Eqn. 1.25, we can see that neutrino oscillation probabilities depend on the energy of neutrinos and the distance L from the neutrino production point. The equation 1.25 is a general transition probability equation from which we can try to understand different oscillation scenario. In addition to the matrix parameters U_{al}, neutrino oscillation probability depends on Δm^2_{lj}, L and E, where E is neutrino energy and L is the baseline. Baseline is the distance between the neutrino production point and the detection point in the Far Detector. In an oscillation experiment, the baseline is fixed in such a way that the detector sees maximum possible oscillation for the peak neutrino energy. In the case of NOvA experiment neutrino energy peaks at 2 GeV. So, in constructing a neutrino oscillation experiment, the value of L/E plays an important role.

Two Flavor Approximation

We can try to understand the neutrino oscillation phenomenon with the help of a two-flavor approximation. Here we consider only two neutrino flavors: electron (ν_e) and muon (ν_μ), along with the corresponding two mass eigenstates ν_1 and ν_2 [33]. Their relation can be written as,

$$\begin{pmatrix} \nu_e \\ \nu_\mu \end{pmatrix} = U \begin{pmatrix} \nu_1 \\ \nu_2 \end{pmatrix}. \tag{1.26}$$

Where U is the 2×2 unitary matrix, using which we can describe the neutrino flavor basis in terms of the neutrino mass basis and vice-versa. Now the 2×2 unitary real matrix would take the form

$$U = \begin{pmatrix} \cos\theta & -\sin\theta \\ \sin\theta & \cos\theta \end{pmatrix}. \tag{1.27}$$

Here neutrino mixing angle θ is the only free parameter in the unitary matrix. With this, we can try to understand two-flavor oscillation scenario with ν_μ as the initial neutrino flavor:

1. The ν_μ survival probability, $\mathrm{P}(\nu_\mu \to \nu_\mu)$:
   This can be seen as the $a = b = \mu$ in the Eqn. 1.25. Since there are only two mass eigenstates and $\Delta_{12} = \Delta m^2_{12} L/4E$. We can substitute Eqn. 1.26 to 1.25. Since the unitary matrix in this case is real and using $\Delta m^2_{12} = \Delta m^2$, we have

$$P\left(\nu_\mu \to \nu_\mu\right) = 1 - \sin^2 2\theta \sin\left(\frac{\Delta m^2 L}{4E}\right). \tag{1.28}$$

2. The ν_e appearance probability, P($\nu_\mu \rightarrow \nu_e$):
   Under the two-flavor hypothesis, this can be written as,
   1-$P\left(\nu_\mu \rightarrow \nu_\mu\right)$

$$P\left(\nu_\mu \rightarrow \nu_e\right) = \sin^2 2\theta \, \sin\left(\frac{\Delta m^2 L}{4E}\right) \tag{1.29}$$

   From Eqns. 1.28 and 1.29, we can see that the oscillation probability amplitude is determined by angle θ, which is the only neutrino mixing matrix parameter present in this case.

Three-flavor Oscillation

The three-flavor neutrino oscillation formalism takes into account of three neutrino flavors predicted by the standard model. These include electron neutrino (ν_e), muon neutrino (ν_μ) and tau neutrino (ν_τ). Each of these flavor states can be expressed as a linear combination of three mass eigenstates (ν_1, ν_2 and ν_3). The PNMS matrix [34] is of dimension 3×3 and as a result, there will be four independent parameters that determine the neutrino oscillation. We can express it as,

$$\begin{pmatrix} \nu_e \\ \nu_\mu \\ \nu_\tau \end{pmatrix} = \begin{pmatrix} U_{e1} & U_{e2} & U_{e3} \\ U_{\mu 1} & U_{\mu 2} & U_{\mu 3} \\ U_{\tau 1} & U_{\tau 2} & U_{\tau 3} \end{pmatrix} \begin{pmatrix} \nu_1 \\ \nu_2 \\ \nu_3 \end{pmatrix}. \tag{1.30}$$

The four independent parameters in this equation are neutrino mixing angles, θ_{12}, θ_{13} and θ_{23} and a complex phase term δ known as CP violating phase [35]. Following the PDG notation [36], the matrix can be written as,

$$U = \begin{pmatrix} c_{12}c_{13} & s_{12}c_{13} & s_{13}e^{-i\delta} \\ -s_{12}c_{23} - c_{12}s_{23}s_{13}e^{i\delta} & c_{12}c_{23} - s_{12}s_{23}s_{13}e^{i\delta} & s_{23}c_{13} \\ s_{12}s_{23} - c_{12}c_{23}s_{13}e^{i\delta} & -c_{12}s_{23} - s_{12}c_{23}s_{13}e^{i\delta} & c_{23}c_{13} \end{pmatrix}. \tag{1.31}$$

Here $s_{ij} = \sin\theta_{ij}$ and $c_{ij} = \cos\theta_{ij}$. The matrix in Eqn. 1.31 can be conveniently written as the product of three different matrices as given below:

$$U = \begin{pmatrix} 1 & 0 & 0 \\ 0 & c_{23} & s_{23} \\ 0 & -s_{23} & c_{23} \end{pmatrix} \begin{pmatrix} c_{13} & 0 & s_{13}e^{-i\delta} \\ 0 & 1 & 0 \\ -s_{13}e^{i\delta} & 0 & c_{13} \end{pmatrix} \begin{pmatrix} c_{12} & s_{12} & 0 \\ -s_{12} & c_{12} & 0 \\ 0 & 0 & 1 \end{pmatrix}. \tag{1.32}$$

Here the mixing matrix is broken in terms of three rotation matrices R_{ij}, along the Euler axes:

$$U = R_{23}(\theta_{23})R_{13}(\theta_{13}, \delta)R_{12}(\theta_{12}), \tag{1.33}$$

where ij refers to the plane in which the rotation takes place. Due to historical reasons θ_{12} is known as solar mixing angle, θ_{13} is known as reactor mixing angle since θ_{13} is first measured by reactor experiments. And θ_{23} sector is first measured by atmospheric neutrino oscillation experiments.

What if neutrino passes through matter - MSW effect

In deriving Eqn. 1.25, we assumed a free particle Hamiltonian for the neutrino mass eigen states. In other words, we considered the oscillation of neutrino while it propagates through the vacuum. But in experiments like NOvA the neutrinos travel through the "rock". This causes the neutrinos to interact with matter and alter its oscillation probability [37]. This is known as the MSW effect (Mikheyev-Smirnov-Wolfenstein effect). The matter consists of particles such as neutrons, protons, and electrons. The ν_e can interact with electron in the matter through exchange of $W^{\pm}$ (charged-current interaction) while ν_μ and ν_τ cannot. But in the neutral-current interaction which is mediated by the Z^0 boson, a neutrino, irrespective of its flavor can interact with neutron, proton or electron. But the effect of the interaction on electrons and protons exactly cancels and the remaining contribution is only by neutrons. So the ultimate effect is a modification [38] of the Hamiltonian with factors:

$$V_{\mathrm{NC}} = -G_F N_n/\sqrt{2}, \tag{1.34}$$

$$V_{\mathrm{CC}} = G_F N_e \sqrt{2}. \tag{1.35}$$

Here N_n and N_e are densities of neutrons and electrons respectively and G_F is the Fermi constant.

The effect of the addition of these potentials can be seen as a correction to the neutrino mass. The effect of V_{CC} is changing effective mass of ν_e only while keeping that of ν_μ unaltered. When neutrinos pass through sufficiently high electron densities, this effect of V_{CC} causes an amplification of neutrino oscillation. At the same time V_{NC} modifies the effective mass of all of the neutrino flavors. Thus the effect is not a considerable factor in the case of neutral-current interactions. Since this thesis is based on the neutral-current analysis, we do not expect this to be a large effect.

1.4.1 Current Landscape of Neutrino Oscillation Measurements

Neutrino experiments are generally designed to study different oscillation parameters and PNMS matrix elements. With reference to the sources of neutrino, neutrino oscillation experiments can be broadly classified as:

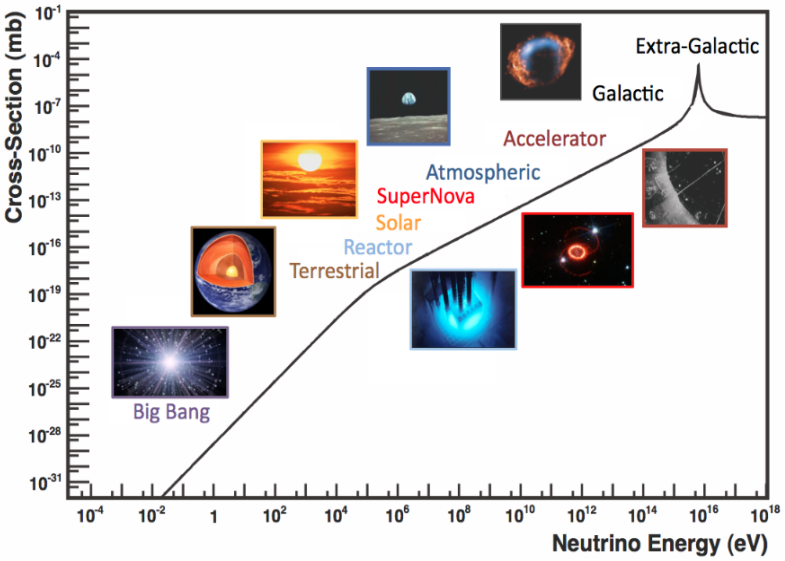

Figure 1.2: Different neutrino sources and the energy scale of neutrinos from each source. Adapted from Ref.[39].

1. Solar neutrino experiments – Here neutrinos of solar origin is used with an $L/E \approx 1500$ km/GeV, and the energy falls in the MeV range. They are most sensitive to θ_{12} and Δm^2_{12}. Due to the high density at the sun's core, the MSW effect is predominant. Examples are GALLEX [40], SAGE [41], Super-K [42], and SNO [43].

2. Reactor neutrino experiments – Electron antineutrino ($\bar{\nu}_e$) produced in the neutrino reactor is used to study neutrino oscillation in the experiments such as Chooz [44], Double Chooz [45], RENO [46], and Daya Bay [47]. It is the reactor experiments first measured θ_{13}.

3. Atmospheric neutrino experiments – Neutrinos produced in the atmosphere as a result of cosmic ray interaction with atmospheric par-

ticles are used in these experiments. Examples are Super-K [48, 49] and IceCube [50]. These experiments are highly sensitive to θ_{23} due to its characteristic L/E which falls in 500 km/GeV range.

4. Accelerator based neutrino experiments – These experiments study neutrinos produced by the particle accelerator generally with an energy of order GeV. Some experiments have a baseline in the range of a couple of kilometers such as Minerva [51], LSND [52], MicroBooNE [53] and are known as short-baseline experiments. The two detector experiments such as MINOS [54] and NOvA [55] have a short-baseline near detector and a long-baseline far detector. These have a baseline which falls in a range of hundreds of kilometers. These experiments are sensitive to the neutrino mixing parameters such as θ_{13}, θ_{23}, Δm^2_{32} and δ.

Current known values of the neutrino mixing matrix elements and the three-flavor oscillation parameters are shown in Figs. 1.3 and 1.4.

$$\text{NuFIT 4.1 (2019)}$$

$$|U|^{\text{w/o SK-atm}}_{3\sigma} = \begin{pmatrix} 0.797 \to 0.842 & 0.518 \to 0.585 & 0.143 \to 0.156 \\ 0.244 \to 0.496 & 0.467 \to 0.678 & 0.646 \to 0.772 \\ 0.287 \to 0.525 & 0.488 \to 0.693 & 0.618 \to 0.749 \end{pmatrix}$$

$$|U|^{\text{with SK-atm}}_{3\sigma} = \begin{pmatrix} 0.797 \to 0.842 & 0.518 \to 0.585 & 0.143 \to 0.156 \\ 0.243 \to 0.490 & 0.473 \to 0.674 & 0.651 \to 0.772 \\ 0.295 \to 0.525 & 0.493 \to 0.688 & 0.618 \to 0.744 \end{pmatrix}$$

Figure 1.3: Precision value of matrix elements using standard three-flavor neutrino oscillation measurements. The top matrix is without SuperK atmospheric data in the global fit and the bottom is with SuperK atmospheric data. Table adapted from Ref. [56].

NuFIT 4.1 (2019)

		Normal Ordering (best fit)		Inverted Ordering ($\Delta\chi^2 = 6.2$)	
		bfp $\pm 1\sigma$	3σ range	bfp $\pm 1\sigma$	3σ range
without SK atmospheric data	$\sin^2\theta_{12}$	$0.310^{+0.013}_{-0.012}$	$0.275 \to 0.350$	$0.310^{+0.013}_{-0.012}$	$0.275 \to 0.350$
	$\theta_{12}/^\circ$	$33.82^{+0.78}_{-0.76}$	$31.61 \to 36.27$	$33.82^{+0.78}_{-0.76}$	$31.61 \to 36.27$
	$\sin^2\theta_{23}$	$0.558^{+0.020}_{-0.033}$	$0.427 \to 0.609$	$0.563^{+0.019}_{-0.026}$	$0.430 \to 0.612$
	$\theta_{23}/^\circ$	$48.3^{+1.1}_{-1.9}$	$40.8 \to 51.3$	$48.6^{+1.1}_{-1.5}$	$41.0 \to 51.5$
	$\sin^2\theta_{13}$	$0.02241^{+0.00066}_{-0.00065}$	$0.02046 \to 0.02440$	$0.02261^{+0.00067}_{-0.00064}$	$0.02066 \to 0.02461$
	$\theta_{13}/^\circ$	$8.61^{+0.13}_{-0.13}$	$8.22 \to 8.99$	$8.65^{+0.13}_{-0.12}$	$8.26 \to 9.02$
	$\delta_{\rm CP}/^\circ$	222^{+38}_{-28}	$141 \to 370$	285^{+24}_{-26}	$205 \to 354$
	$\frac{\Delta m^2_{21}}{10^{-5}\ \text{eV}^2}$	$7.39^{+0.21}_{-0.20}$	$6.79 \to 8.01$	$7.39^{+0.21}_{-0.20}$	$6.79 \to 8.01$
	$\frac{\Delta m^2_{3\ell}}{10^{-3}\ \text{eV}^2}$	$+2.523^{+0.032}_{-0.030}$	$+2.432 \to +2.618$	$-2.509^{+0.032}_{-0.030}$	$-2.603 \to -2.416$
		Normal Ordering (best fit)		Inverted Ordering ($\Delta\chi^2 = 10.4$)	
		bfp $\pm 1\sigma$	3σ range	bfp $\pm 1\sigma$	3σ range
with SK atmospheric data	$\sin^2\theta_{12}$	$0.310^{+0.013}_{-0.012}$	$0.275 \to 0.350$	$0.310^{+0.013}_{-0.012}$	$0.275 \to 0.350$
	$\theta_{12}/^\circ$	$33.82^{+0.78}_{-0.76}$	$31.61 \to 36.27$	$33.82^{+0.78}_{-0.75}$	$31.61 \to 36.27$
	$\sin^2\theta_{23}$	$0.563^{+0.018}_{-0.024}$	$0.433 \to 0.609$	$0.565^{+0.017}_{-0.022}$	$0.436 \to 0.610$
	$\theta_{23}/^\circ$	$48.6^{+1.0}_{-1.4}$	$41.1 \to 51.3$	$48.8^{+1.0}_{-1.2}$	$41.4 \to 51.3$
	$\sin^2\theta_{13}$	$0.02237^{+0.00066}_{-0.00065}$	$0.02044 \to 0.02435$	$0.02259^{+0.00065}_{-0.00065}$	$0.02064 \to 0.02457$
	$\theta_{13}/^\circ$	$8.60^{+0.13}_{-0.13}$	$8.22 \to 8.98$	$8.64^{+0.12}_{-0.13}$	$8.26 \to 9.02$
	$\delta_{\rm CP}/^\circ$	221^{+39}_{-28}	$144 \to 357$	282^{+23}_{-25}	$205 \to 348$
	$\frac{\Delta m^2_{21}}{10^{-5}\ \text{eV}^2}$	$7.39^{+0.21}_{-0.20}$	$6.79 \to 8.01$	$7.39^{+0.21}_{-0.20}$	$6.79 \to 8.01$
	$\frac{\Delta m^2_{3\ell}}{10^{-3}\ \text{eV}^2}$	$+2.528^{+0.029}_{-0.031}$	$+2.436 \to +2.618$	$-2.510^{+0.030}_{-0.031}$	$-2.601 \to -2.419$

Figure 1.4: Precision value of neutrino mixing angles and mass square splitting as of 2019 using updated global analysis of standard three-flavor neutrino oscillation measurements. Table adapted from Ref. [56].

1.5 Sterile Neutrinos

The standard three-flavor oscillation is widely accepted among physicists. The three-flavor mixing angles and the other parameters have been precisely measured. Also the CERN LEP (Large Electron-Positron) collider experiment data [9] fit well with the prediction that there exist only three active neutrino flavors as shown in Fig. 1.5. But some of the experimental results point to the existence of additional neutrino states which have masses at the eV^2 scale. This indicates that if there are additional

neutrinos, it could not have any coupling with the Z^0 boson. Hence it does not participate in any standard model interaction. These neutrinos are called "sterile neutrinos". A sterile neutrino is considered as a lepton that is neutral in charge and does not participate in the ordinary weak interaction. Many standard model extensions can accommodate sterile neutrinos [57]. The theory of sterile neutrinos reveals that it can mix with the active neutrinos. As a consequence, the oscillation experiments like NOvA can be used to search for sterile neutrinos. The theory of the early universe and leptogenesis can also accommodate sterile neutrinos.

The three-flavor oscillation formalism can be generalized to deal with the additional sterile neutrino states. We have seen how the three-flavor active neutrino mixing is formulated with the help of a 3×3 unitary matrix parameterized by three neutrino mixing angles and one physical phase. This can be generalized for N neutrino mass eigenstates and the N-flavor neutrino mixing can be formulated with the help of a unitary matrix having a dimension of $N \times N$. It will have $N(N-1)/2$ mixing angles and $(N-1)(N-2)/2$ physical phases[2] (see Ref. [58]). An estimate of the flavor content in a particular mass eigenstate is given by the neutrino mixing angles. The discussion in this thesis is limited to the 3+1 model of neutrinos [59] with the assumption that there exist three active neutrinos and one light sterile neutrino.

[2]Dirac CP-violating phases which may be observed in oscillations

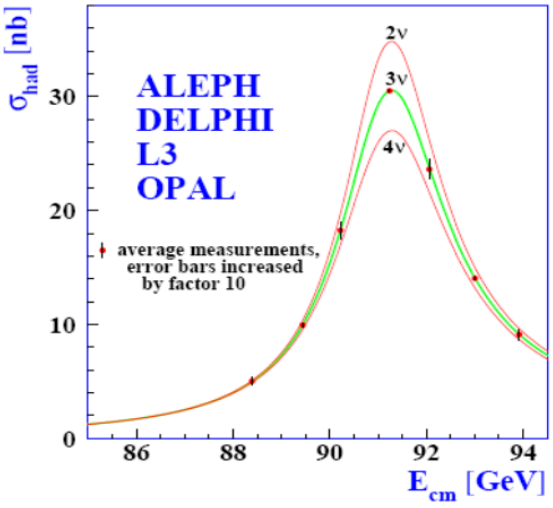

Figure 1.5: The LEP experimental data fitted with different neutrino models. The three-flavor model fitted well with the data. Plot adapted from Ref. [9].

1.6 Experimental Anomalies

Implementation of an additional neutrino state is sufficient to explain the anomalies observed in the short-baseline neutrino oscillation experiments. The neutrino oscillation experiments are termed as short-baseline experiments, if their $L/E \sim 1$ m/MeV, where L is the distance between the neutrino production point and the neutrino interaction point, in meters and E is the energy of the neutrino in MeV unit. This L/E gives them a sensitivity to the oscillations characterized by a mass splitting of 1 eV. The short-baseline experiment, LSND (Liquid Scintillator Neutrino Detector) at Los Alamos Laboratory reported an anomaly in its experimental data [60]. The Fermilab short-baseline neutrino experiment MiniBooNE (Mini Booster Neutrino Experiment) studied the $\bar{\nu}_\mu\,(\nu_\mu)$ oscillating to $\bar{\nu_e}\,(\nu_e)$ also observed an anomaly [53, 61]. Some other anomalies reported in the neutrino experiments include the reactor experiment anomaly [62], radioactive anomalies in GALLEX (Gallium Experiment) [63] and the observed anomaly in the solar neutrino experiment SAGE (Soviet-American Gallium Experiment) [64].

1.6.1 The LSND Anomaly

The LSND experiment has used the neutrino beam produced from Los Alamos Meson Physics Facility. This experiment was designed to study the oscillation of muon antineutrinos into electron antineutrinos ($\bar{\nu}_\mu \rightarrow \bar{\nu}_e$). This experiment reported an excess of antineutrino events above the expected background events at 3.8σ significance. There were 87.9 $\pm$ 22.4$\pm$ 6.0 $\bar{\nu}_e$ events above an expected background of 30.0$\pm$6.0 events [60]. This corresponds to an oscillation probability of 0.264$\pm$0.067(stat.)$\pm$ 0.045(syst.)%. Fig. 1.6 shows the LSND excess.

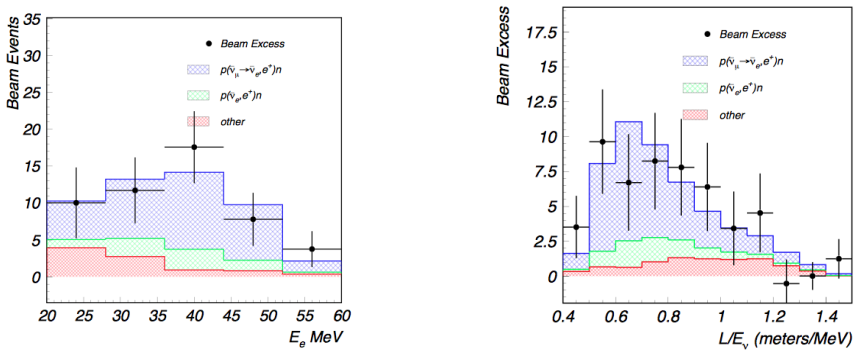

Figure 1.6: The LSND excess in the ν_e events. The observed LSND data excess is plotted as a function of energy (left) and as a function of the ratio, L/E (right). Plot is taken from Ref. [60].

The LSND excess may be interpreted as a two flavor neutrino oscillation with a $\Delta m^2 \sim 1$ eV^2 and $\sin^2 2\theta_{\mu e} \sim 0.003$ (see Fig.1.7). The Δm^2 reported by the LSND is $\sim 10^5$ order of magnitude larger than that of the Δm^2_{21} value and $\sim 10^3$ order of magnitude larger than the Δm^2_{32}. The existence of three mass-square splittings can only be explained with the help of at least four neutrino mass eigenstates. This experimental result supports the existence of more than three neutrinos.

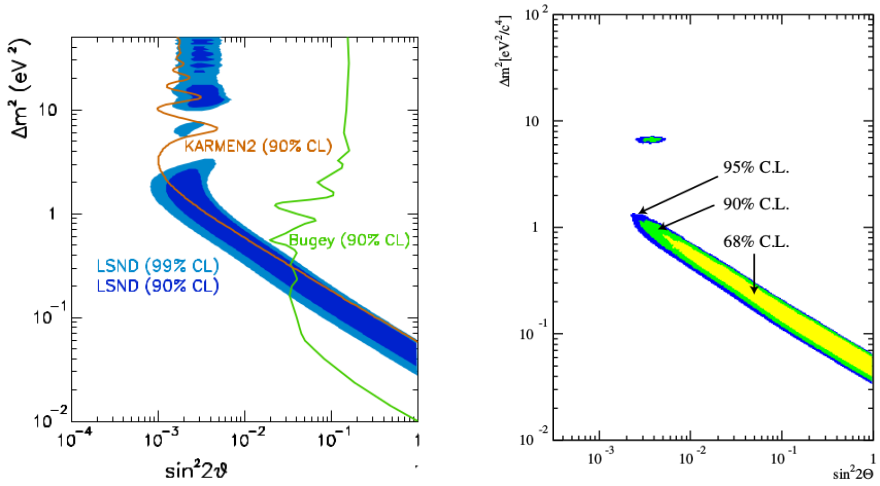

Figure 1.7: The fitting is done in Δm^2 vs $\sin^2 2\theta$ parameter space. Results from the reactor Bugey experiment (green) and KARMEN2 (brown) are shown with 90% confidence limit (90%C.L.). The allowed region is given by the KARMEN and LSND combined analysis (right). Fig. is adapted from Ref. [65].

1.6.2 The MiniBooNE Experiment

The Fermilab experiment MiniBooNE was designed to investigate on the LSND anomaly [53]. This experiment was designed with an L/E (ratio of the average distance traveled by the neutrino to the average neutrino energy) of same in magnitude as that of the LSND experiment. The Fermilab Booster Neutrino Facility (FBNF) supplied neutrinos to the MiniBooNE detector, which was a spherical tank of diameter ~ 12.2 m filled with eight hundred tons of mineral oil. This experiment investigated both $\bar{\nu}_\mu \rightarrow \bar{\nu}_\mathrm{e}$ oscillations and $\nu_\mu \rightarrow \nu_\mathrm{e}$ oscillations. Selecting the charged current quasi-elastic (CCQE) event ($\nu_\mathrm{e} + \mathrm{C} \rightarrow \mathrm{e}^- + \mathrm{X}$) was the primary objective of the event selection. The predicted neutrino flux at the MiniBooNE detector is shown in Fig. 1.8.

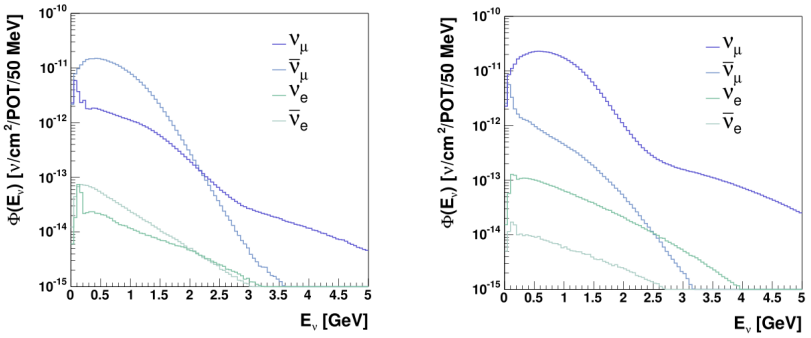

Figure 1.8: The distribution of the predicted neutrino flux in the MiniBooNE experiment. The component-wise neutrino flux distribution both for neutrinos (right) and antineutrinos (left). Fig. is adapted from Ref. [65].

Fig. 1.9 shows the reconstructed neutrino energy spectra that split into different components. In this figure, we can see that the data and Monte Carlo simulation (MC) are in good agreement in the region $E_{QE} >$ 475 MeV along the X-axis. At the same time, there is an excess in the data events in the region below 475 MeV.

The MiniBooNE experiment studied both neutrino ($\nu_\mu \rightarrow \nu_e$) and antineutrino ($\bar{\nu}_\mu \rightarrow \bar{\nu}_e$) oscillation data and reported a combined result. This experiment studied 6.46×10^{20} protons on target (POT) ν_μ data and 11.27×10^{20} protons on target (POT) $\bar{\nu}_\mu$ data with the same oscillation model to combine these results. Both the neutrino and antineutrino mode of run reported an excess in the data events. A 3.8σ event excess was observed in the combined neutrino and antineutrino data in the neutrino oscillation energy range from 200 MeV to 1250 MeV. The combined neutrino-antineutrino analysis results are summarized in Table 1.1. The MiniBooNE result agrees with the LSND anomalous result. The LSND-MiniBooNE joint-fit result is shown in Fig. 1.10.

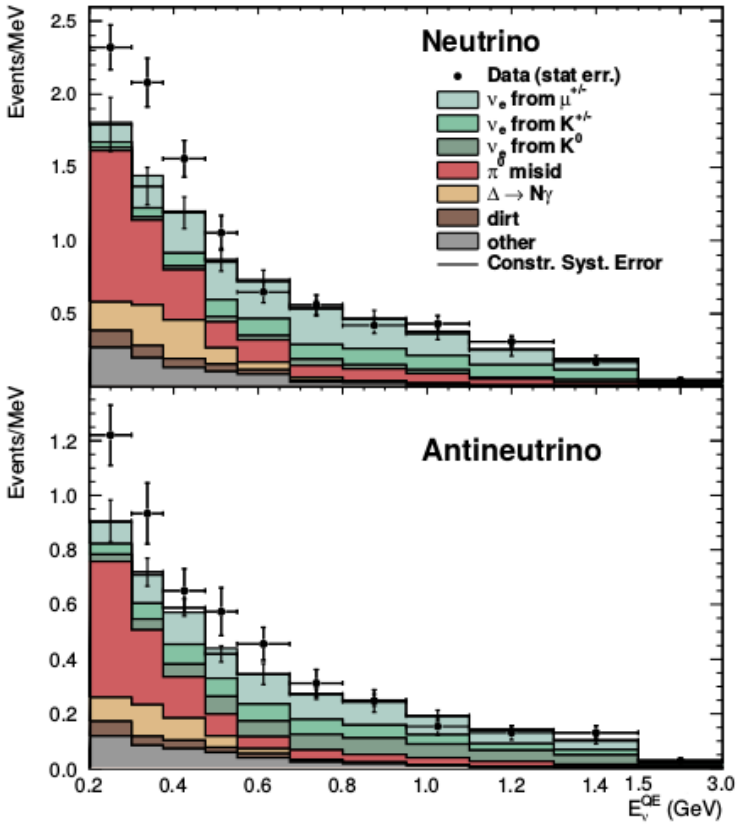

Figure 1.9: The stacked plot with reconstructed neutrino energy spectra (a) and antineutrino spectra (b) in the MiniBooNE detector. Fig. is adapted from Ref. [66].

Mode of run	Data	Background	Excess
Neutrino	952	790.0 ± 28.1 ± 38.7	162.0 ± 47.8
Antineutrino	478	399.6 ± 20.0 ± 20.3	78.4 ± 28.5
Combined	1430	1189.7 ± 34.5 ± 52.6	240.3 ± 62.9

Table 1.1: MiniBooNE data excess reported in the neutrino and antineutrino mode of run within the neutrino oscillation energy range from 200 MeV to 1250 MeV. The uncertainties included are both statistical and systematic. Table is from Ref. [66].

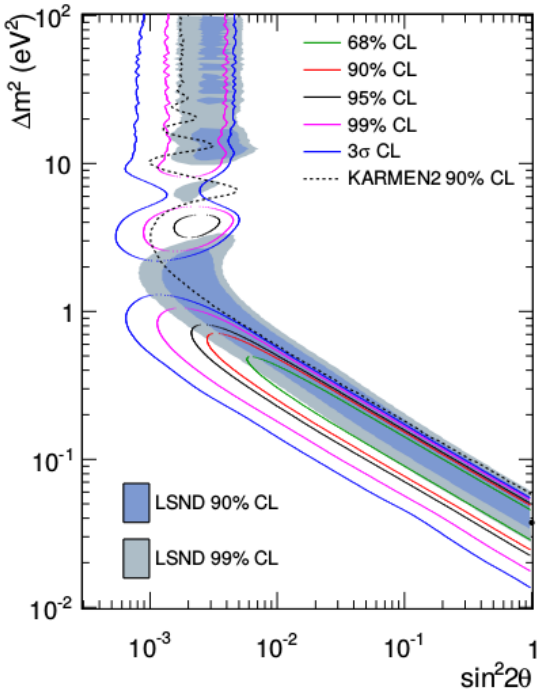

Figure 1.10: The allowed region of parameter space obtained from the MiniBooNE antineutrino fit result, this result is consistent with the anomalous result reported by the LSND. Fig. is adapted from Ref. [66].

1.6.3 The Reactor Anomalies

The antineutrinos are produced in the decay chains of ^{235}U,^{238}U,^{239}Pu, and ^{242}Pu in the nuclear reactor. The β-decay of nuclear fission product yields an electron accompanied by an antineutrino [67]. The reanalysis of the old neutrino data from the reactor experiments unboxed the reactor anomaly. This reanalysis is done with the newly evaluated $\bar{\nu}_e$ flux with improved modeling of electron to $\bar{\nu}_e$ data conversion. This updated evaluation estimated a $\bar{\nu}_e$ flux $\approx$3.5% larger than that previously used. For neutrinos that travel 10-100 m from the core of the nuclear reactor to the neutrino detector, this leads to a change in the ratio of observed to expected events from 0.976 $\pm$ 0.024 to 0.943 $\pm$ 0.023 which was calculated as a deviation from unity at 98.6% confidence limit (C.L) [68]. This deficit can be seen as an energy dependent suppression of $\bar{\nu}_e$ flux at >15 m.

This can be explained as an oscillation with a $\Delta m^2 \sim 1$ eV^2. The right plot in Fig.1.11 shows the ratio of observed to the expected number of events in various experiments, with varying Δm^2 and $\sin^2 2\theta_{14}$.

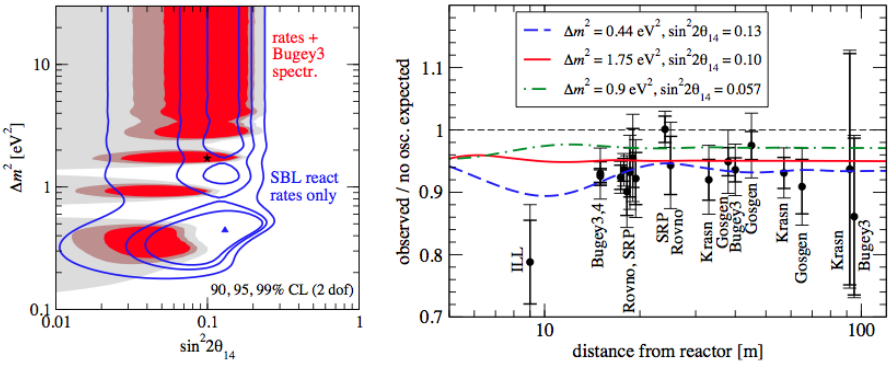

Figure 1.11: The allowed regions of oscillation parameters from the short-baseline data with 3+1 model (left). Ratio of measured to expected number of events, together with prediction for different Δm^2 and $\sin^2 2\theta_{14}$ values (right). Fig. is taken from [69].

1.6.4 The Gallium Anomaly

The Gallium anomaly is the deficit of the observed ν_e events in GALLEX and SAGE (Soviet-American Gallium Experiment) solar neutrino detectors. The data events observed to be less than the predicted number, as shown in Fig. 1.12. The ν_e events are produced by the radioactive source of Cr and Ar that was placed in the middle of the cylindrical detector through the interaction

$$e^- + {}^{37}\mathrm{Ar} \rightarrow {}^{37}\mathrm{Cl} + \nu_e \tag{1.36}$$

$$e^- + {}^{51}\mathrm{Cr} \rightarrow {}^{51}\mathrm{V} + \nu_e \tag{1.37}$$

The neutrino was detected in the detector through the interaction

$$\nu_e + {}^{71}\mathrm{Ga} \rightarrow {}^{71}\mathrm{Cu} + e^- \tag{1.38}$$

This interaction was also used to detect the solar neutrinos. The average distance traveled by the neutrinos before they interact is 1.6 m for

GALLEX and 0.6 for SAGE, with an average neutrino energy of $\sim$ 0.8 MeV. The Gallium anomaly can be explained as a short-baseline neutrino oscillation with a $\Delta m^2 \sim 1$ eV^2.

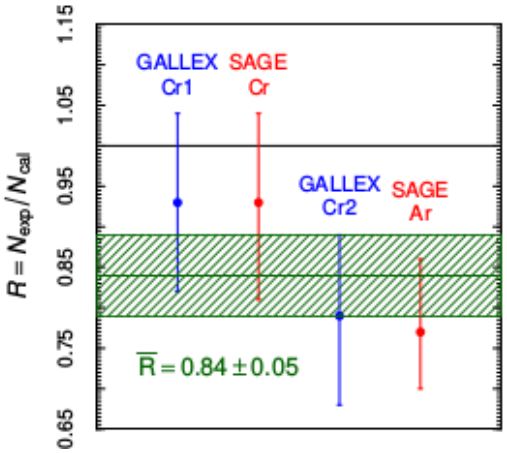

Figure 1.12: Results of GALLEX and SAGE experiments. $\overline{\text{R}}$ in the figure is calculated by taking the ratio of the measured data to the calculated number. The total systematic uncertainty is shown as green band. Fig. is adapted from Ref. [70].

1.6.5 Adding a 4th Neutrino Flavor into the Recipe

The evidence from some experiments (as discussed in Sec. 1.6) demands the existence of more than three neutrinos. If there exist such neutrinos, they may be light sterile. This thesis is based on the searches for a light sterile neutrino at the NOvA Far Detector through the neutral-current disappearance.

Putting a sterile neutrino into the standard three-flavor would add a column and row to the standard PMNS matrix. The new matrix has a dimension of 4×4. As a consequence of this, there will be a total of six mixing angles and three physical phases. Analogous to a standard three-flavor PNMS matrix shown in Eqn. 1.33, we can look in to the four-flavor PMNS matrix as a product rotation matrices with respect to Euler's axes:

$$U = R_{34}(\theta_{34})R_{24}(\theta_{24},\delta_2)R_{14}(\theta_{14})R_{23}(\theta_{23})R_{13}(\theta_{13},\delta_1)R_{12}(\theta_{12},\delta_3). \quad (1.39)$$

The mixing matrix can be written as,

$$U = \begin{pmatrix} U_{e1} & U_{e2} & c_{14}s_{13}e^{-i\delta_1} & s_{14} \\ U_{\mu 1} & U_{\mu 2} & -s_{14}s_{13}e^{-i\delta 1}s_{24}e^{-i\delta 2} + c_{13}s_{23}c_{24} & c_{14}s_{24}e^{-i\delta 2} \\ U_{\tau 1} & U_{\tau 2} & -s_{14}c_{24}s_{34}s_{13}e^{-i\delta 1} - c_{13}s_{23}s_{34}s_{24}e^{i\delta 2} + c_{13}c_{23}c_{34} & c_{14}c_{24}s_{34} \\ U_{s1} & U_{s2} & -s_{14}c_{24}c_{34}s_{13}e^{-i\delta 1} - c_{13}s_{23}c_{34}s_{24}e^{i\delta 2} - c_{13}c_{23}s_{34} & c_{14}c_{24}c_{34} \end{pmatrix}. \tag{1.40}$$

The probability of a neutrino flavor oscillating to another is given by Eqn. 1.25,

$$P\left(\nu_a \to \nu_b\right) = \delta_{ab} - 4\sum_{l>j} \Re\left(U^*_{al}U_{bl}U_{aj}U^*_{bj}\right)\sin^2\Delta_{lj} + 2\sum_{l>j}\mathrm{Im}\left(U^*_{al}U_{bl}U_{aj}U^*_{bj}\right)\sin 2\Delta_{lj}, \tag{1.41}$$

where $\Delta_{lj} = \Delta m^2_{lj}L/4E$. In the case of sterile oscillation analysis with a ν_μ beam, we can formulate a sterile neutrino appearance channel. We are going to look into the $\nu_\mu \to \nu_\mu$ and $\nu_\mu \to \nu_a$ oscillation probabilities, where a can be e, τ or sterile (s). Because of the fact that $\Delta_{21} << \Delta_{31}$ and so first and second mass states are treated as degenerate. As a result $\sin\Delta_{21}$ can be set to zero that implies $\Delta_{42} = \Delta_{41}$ and $\Delta_{32} = \Delta_{31}$. The oscillation probability equation 1.41, after applying the orthogonality relation $\sum_i U_{ai}U^*_{bi}$ can be divided as:

$$\begin{aligned} P\left(\nu_\mu \to \nu_\mu\right) = 1 - 4\Big[&|U_{\mu 3}|^2\left(1 - |U_{\mu 3}|^2 - |U_{\mu 4}|^2\right)\sin^2\Delta_{31} \\ &+ |U_{\mu 4}|^2|U_{\mu 3}|^2\sin^2\Delta_{43} \\ &+ |U_{\mu 4}|^2\left(1 - |U_{\mu 3}|^2 - |U_{\mu 4}|^2\right)\sin^2\Delta_{41}\Big], \end{aligned} \tag{1.42}$$

$$\begin{aligned} P\left(\nu_\mu \to \nu_a\right) = 4\Re\Big[&|U_{\mu 3}|^2|U_{a3}|^2\sin^2\Delta_{31} \\ &+ |U_{\mu 4}|^2|U_{a4}|^2\sin^2\Delta_{41} \\ &+ U^*_{\mu 4}U_{a4}U_{\mu 3}U^*_{a3}\left(\sin^2\Delta_{31} - \sin^2\Delta_{43} + \sin^2\Delta_{41}\right)\Big] \\ &+ 2\,\mathrm{Im}\Big[U^*_{\mu 4}U_{a4}U_{\mu 3}U^*_{a3}\left(\sin 2\Delta_{31} - \sin 2\Delta_{41} + \sin 2\Delta_{43}\right)\Big]. \end{aligned} \tag{1.43}$$

Eqn. 1.42 gives the ν_μ charged-current disappearance probability, and Eqn. 1.43 is the probability of muon neutrino oscillating to any of the

other three neutrino flavors. Eqn. 1.43 has a general form of the four-flavor appearance probability. Sterile appearance probability can be obtained by substituting $a = s$ in 1.43. Substituting the matrix elements from Eqn. 1.40 and with approximations and added constraints from other experiments, these probabilities can be simplified further. Substituting the matrix elements from Eqn. 1.40 into Eqn. 1.43 and following the approximations as mentioned in Refs. [71] and [72], one can reach to the sterile appearance probability for a long-baseline experiment like NOvA,

$$\begin{aligned} P\left(\nu_\mu \to \nu_s\right) \approx\ & \cos^4\theta_{14}\cos^2\theta_{34}\sin^2 2\theta_{24}\sin^2\Delta_{41} \\ & + A\ \sin^2\Delta_{31} - B\ \sin 2\Delta_{31}, \end{aligned} \tag{1.44}$$

where $A = \sin^2\theta_{34}\sin^2 2\theta_{23}$ and $B = \frac{1}{2}\sin\delta_{24}\sin\theta_{24}\sin 2\theta_{34}\sin 2\theta_{23}$. The probability of NC disappearance can be represented as [73],

$$\begin{aligned} 1 - P\left(\nu_\mu \to \nu_s\right) \approx\ & 1 - \cos^4\theta_{14}\cos^2\theta_{34}\sin^2 2\theta_{24}\sin^2\Delta_{41} \\ & + A\ \sin^2\Delta_{31} - B\ \sin 2\Delta_{31}. \end{aligned} \tag{1.45}$$

From Eqn. 1.45, it is clear that the NC disappearance probability is sensitive to the sterile mixing angles θ_{34} and θ_{24}, and the phase δ_{24}.

1.6.6 Long-baseline Sterile Neutrino Searches in NOvA

This thesis summarizes the searches for the sterile neutrino at the NOvA far detector. The sterile neutrino search is conducted by looking at the neutral-current event depletion at the far detector. This thesis describes two different neutral-current disappearance analyses: one with 8.85×10^{20} POT of neutrino data and the other with 12.5×10^{20} POT of antineutrino data. We will discuss more of these in the following chapters.

2

NOvA Experimental Design

The NuMI Off-axis ν_e Appearance (NOvA) is a long-baseline neutrino oscillation experiment with functionally identical, segmented, tracking calorimeter near and far detectors. The detectors lie 14.6 mrad off-axis from the Fermilab NuMI (Neutrinos at the Main Injector) beam with a well defined peak in neutrino energy at 2 GeV. The Near Detector (ND) is at 1 km away from the target and is 100 m below from the ground level. At the same time, the Far Detector (FD) is at Ash River, MN which is 810 km away from the target. The FD is situated at the ground surface. The main physics goal of the NOvA experiment is to study ν_e ($\bar{\nu}_e$) appearance and ν_μ ($\bar{\nu}_\mu$) disappearance in a ν_μ ($\bar{\nu}_\mu$) in the NuMI beam [55].

A NOvA detector is composed of alternating vertical and horizontal planes of extruded Polyvinyl Chloride (PVC) cells [74] filled with mineral oil as a liquid scintillator. Each PVC cell contains a looped WLS fiber (wavelength-shifting fiber) [75] coupled to one pixel of an avalanche photodiode (APD). The output of the APD [76] is integrated, shaped, digitalized, and recorded in synchronization with the NuMI *spill time* window which is around 10 μs. The detector reads out all data in a 550 μs window around the spill time window. The data collected in the 550 μs time, in the vicinity of the spill time window is termed as cosmic data. The energy deposited in the detector during this time is due to the cosmogenic particles. A beam spill can contain more than one fundamental interactions. It is common to use the word event to refer to one of the individual fundamental interactions. But, multiple neutrino interactions may be seen in the NOvA ND within the unit of time that defines a single event ("unit of information"). Alternating horizontal and vertical plane structure of the detectors help to visualize the 3D image of an event. We will go through further details of the experimental design in this chapter.

The majority of the points discussed in this chapter is based on Ref. [77].

2.1 NuMI Beam

NOvA is an accelerator experiment and it does need a well maintained supply of neutrinos from a particle accelerator. The schematic diagram of the Fermilab accelerator complex is shown in Fig. 2.1. Negatively charged hydrogen atoms produced from the Ion source is getting accelerated in LINAC (Linear Accelerator) and then it enters the Booster Synchrotron. These protons are fed to the Recycler Ring as 12 bunches of protons, each with approximately 4.5×10^{20} protons. In a process called slip-stacking, 6 new higher intensity bunches are formed out of 12 bunches of protons. These are the output to the Main Injector and accelerated to 120 GeV. The 6 bunches of protons form a spill with a beamwidth of 10 μs. The time interval between the two spills (cycle time) is 1.333 s [78]. This beam pulse helps us to tag the detector response of beam neutrinos and differentiate them from the cosmogenic particle activities.

The NuMI [79] provides a beam of excellent power of 700 kW to NOvA, that makes NOvA the world's most powerful accelerator based neutrino experiment. The data collected in NOvA is expressed in terms of POT (Protons on the Target). Fig. 2.8 shows the beam power as a function of time. The process of neutrino production starts by accelerating 120 GeV protons to a graphite target that is 12.2 m long and has a water cooling system to prevent it from melting down due to the excess heat from the collision. Complex hadron production occurs at the target due to the high energy collision of protons; which produces mesons such as pions and kaons. These pions and kaons are then passed through two parabolic magnetic horns. The mesons passing through the magnetic horns will experience a magnetic field similar to a toroid; which is proportional to I/r, where I is the electric current through the magnetic horn and r is the radius. In the analysis of our interest, I is fixed as 200 kA. The function of this magnetic horn is to focus mesons which eventually decay into neutrinos.

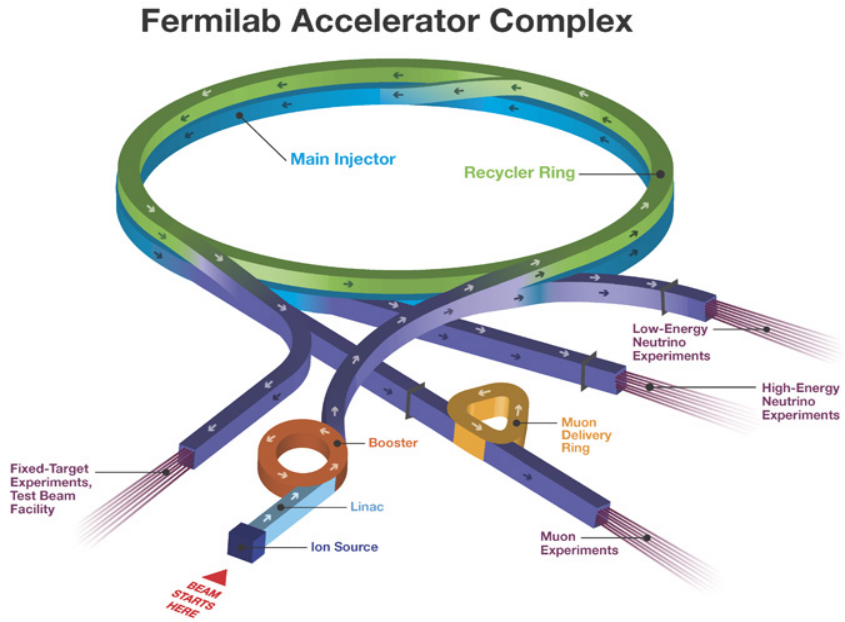

Figure 2.1: An overview of the Fermilab accelerator complex. This diagram is adapted from Ref. [80].

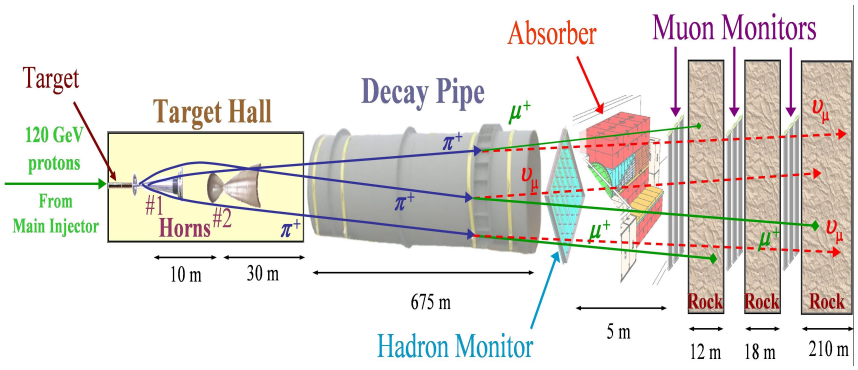

Figure 2.2: This diagram shows how neutrinos are produced with FHC configuration, and is taken from Ref. [81].

The direction of current through the magnetic horns is used to select neutrinos or antineutrinos in the beam. The current configuration of the horns to get a neutrino beam is termed as the Forward Horn Current (FHC) and to get an antineutrino beam is termed as the Reverse Horn Current (RHC). NOvA experiment uses a jargon "FHC analysis" to represent the neutrino beam analysis and "RHC analysis" to represent the antineutrino beam analysis. The following part of this thesis uses these jargons to differentiate between the neutrino analysis and the antineutrino analysis.

This neutrino beam then travels through 675 m long decay pipe with a radius of 1 m. Fig. 2.5 shows the arrangements to get the neutrino beam. This is the place where hadrons decay into leptons and neutrinos. In the FHC configuration, there will be a small number of negatively charged high energy hadrons passing close to beam center. This leads to the presence of few antineutrinos in the neutrino beam and is called wrong sign contamination. Similarly, a fraction of neutrinos contributes to the antineutrino beam.

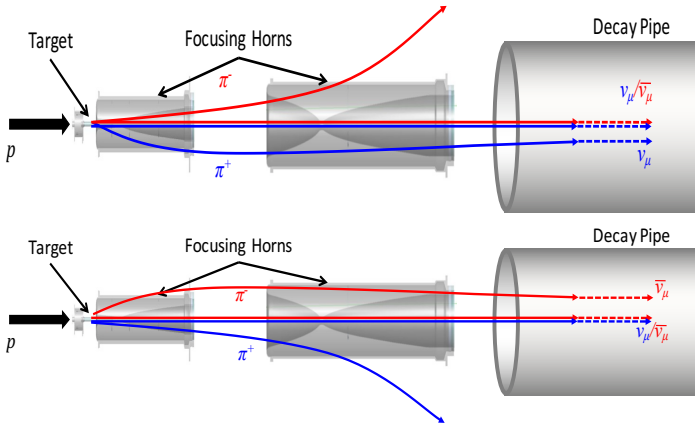

Figure 2.3: Top plot shows how the FHC (neutrino) beam is produced. The bottom plot shows the process of RHC (antineutrino) beam production. Wrong sign contamination happens due to the oppositely charged meson passing close the beam center with high energy.

The dominant hadronic decay modes can be summarized as:

$$\pi^{\pm} \rightarrow \mu^{\pm} + \nu_{\mu}(\bar{\nu_{\mu}}), \tag{2.1}$$

$$\pi^{\pm} \rightarrow e^{\pm} + \nu_e(\bar{\nu_e}), \tag{2.2}$$

$$K^{\pm} \rightarrow \mu^{\pm} + \nu_\mu(\bar{\nu_\mu}), \tag{2.3}$$

$$K^{\pm} \rightarrow e^{\pm} + \nu_e(\bar{\nu_e}), \tag{2.4}$$

$$K^{\pm} \rightarrow \pi^0 + \mu^{\pm} + \nu_\mu(\bar{\nu_\mu}), \tag{2.5}$$

$$K^{\pm} \rightarrow \pi^0 + e^{\pm} + \nu_e(\bar{\nu_e}), \tag{2.6}$$

Muons decay to neutrino via,

$$\mu^{\pm} \rightarrow e^{\pm} + \nu_e(\bar{\nu_e}) + \bar{\nu_\mu}(\nu_\mu). \tag{2.7}$$

Neutral kaon decay can also yield neutrinos. The parent contribution to the neutrino (antineutrino) beam is shown in Fig. 2.4.

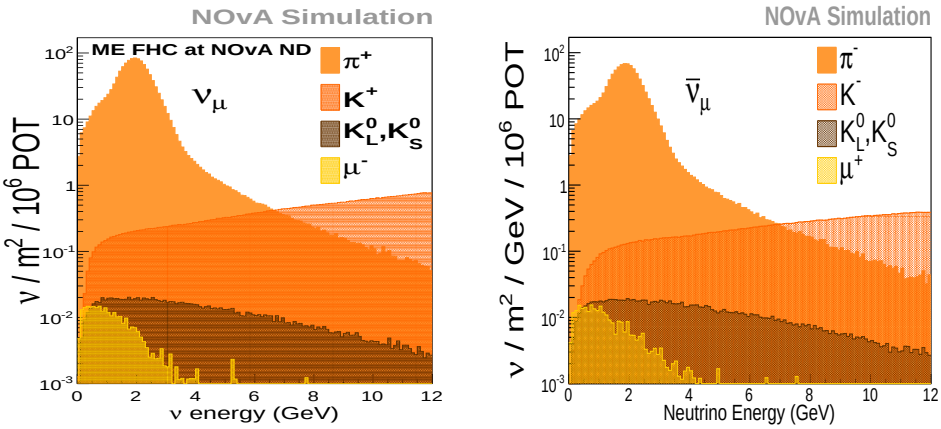

Figure 2.4: Parent information of neutrinos, for FHC (left) and the RHC beam(right).

The neutrinos (antineutrinos) produced in the decay pipe then pass through a hadron monitor to monitor beam direction. Then it passes through a hadron absorber. Next comes the muon monitor placed in between blocks of rock. Eventually, a well focused neutrino (antineutrino) beam directs towards the detectors. Fig. 2.5 represents production of a neutrino beam (FHC configuration).

2.1.1 Off-axis Detector

The NOvA detector is located at 14.6 mrad off from the beam axis. This position of NOvA detector is set to get a well-defined neutrino energy beam peaks at 2 GeV (see Fig. 2.6). The optimum neutrino energy needed to get the first oscillation maximum at the NOvA FD (with a baseline of 810 km) is 2 GeV. The narrow energy band is important so that we get more events where oscillations occur and fewer events where oscillations don't occur. The off-axis detector sees neutrinos with energies do not depend heavily on the broad spectrum of parent pion energies (see Fig. 2.7).

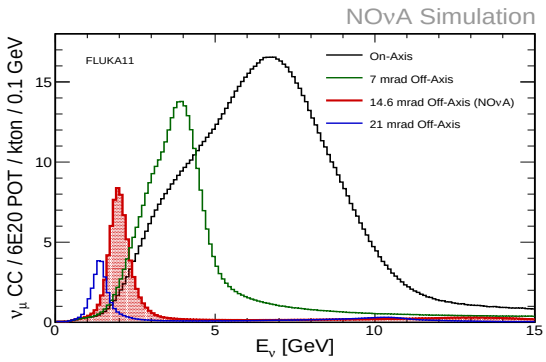

Figure 2.5: This plot shows the distribution of the charged-current events at the NOvA FD with different off-axis angles.

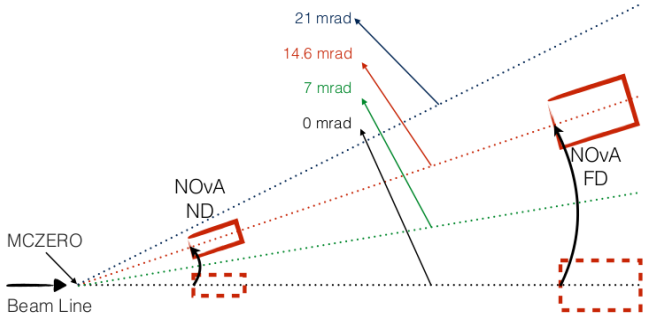

Figure 2.6: This diagram shows the position of NOvA ND and FD.

The neutrino flux produced by the pion decay, as measured from a

detector z distance away from the decay point is given as

$$\Phi = \left[\frac{2\gamma}{1+\gamma^2\theta^2}\right]^2 \frac{A}{4\pi z^2}. \tag{2.8}$$

Where A is the area of cross section, θ is the angular separation between pion direction and neutrino direction, and $\gamma = \frac{E_\pi}{m_\pi}$ Similarly, the neutrino energy is found to be

$$E_\nu = \frac{0.43E_\pi}{1+\gamma^2\theta^2}. \tag{2.9}$$

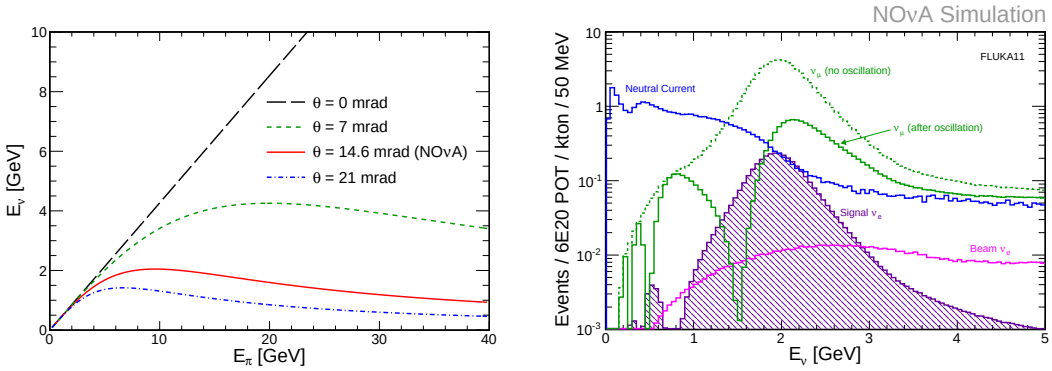

Figure 2.7: The left figure shows the variation of E_ν with E_π. The right figure shows the variation of E_ν for different neutrino types at NOvA FD.

From the left Fig. 2.7, we can see at $\theta = 14.6$ mrad, for a wide range of pion energies the neutrino energy does not change. Similarly from the right plot, the ν_μ after oscillation and ν_e signal at NOvA FD is maximum at E_ν equal to 2 GeV. We can also see that neutral-current events for the main oscillation studies is comparatively low in this region. Also, we can eliminate the majority of the neutral-current events if the beam is narrowly peaked at 2 GeV. This is attained mainly by eliminating the intrusion of high energy neutral-current events which back-feed into the low energy region, due to the energy carried away by the outgoing neutrino.

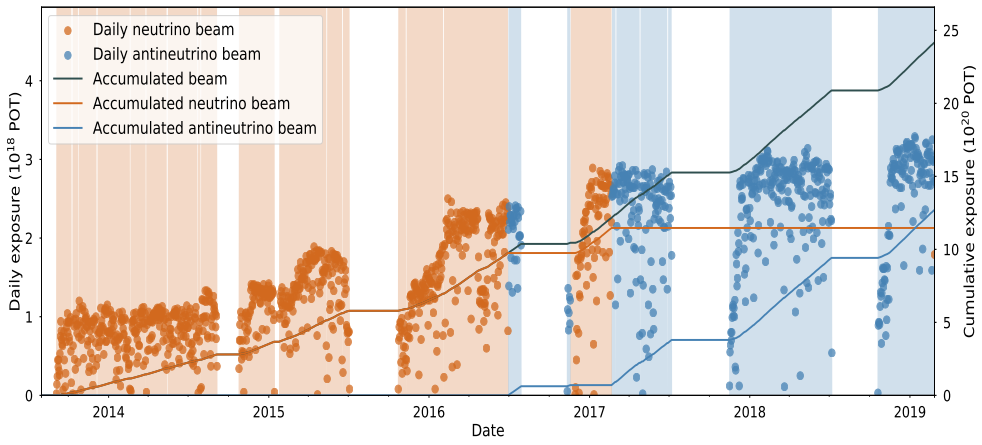

Figure 2.8: Time series showing the daily neutrino beam (orange) or antineutrino beam (blue) POT recorded by NOvA, from the start of commissioning to 2019-02-26. Also plotted are lines for the cumulative neutrino beam POT (dark orange), cumulative antineutrino beam POT (dark blue) and total accumulated POT (gray).

2.2 NOvA Detectors

As we discussed in the introductory section of this chapter, NOvA is a two detector experiment with two functionally identical detectors ND and FD. Each detector is a 65% active calorimeter by volume. The NOvA detector design is aimed to attain specific goals such as separating charged-current (CC) events from neutral-current (NC) events. The electron showers and muon track are the signature of CC events; which is the signal for two main oscillation analyses of NOvA. The NC events deposit energy in the detector volume as hadronic showers. In the following subsections, we will discuss more the detector design and its major components.

Figure 2.9: The figure shows two detectors and a baseline of 810 km between the detectors.

2.2.1 Detector Structure

The basic building block of the NOvA detector is a PVC cell with a looped WLS fiber in it and is filled with liquid scintillator [82]. The PVC cell has a rectangular cross section with corners smoothed and having a dimension 6×4 cm. One end of the PVC cell is sealed and the other end is opened. The WLS fiber is looped and it lies along the length of the cell. Two free ends of the WLS fiber is kept at the open end of the PVC cell.

The major components of the liquid scintillator are:

- Mineral oil that is used as a solvent and takes up the majority (95.5 %) of the total active detector volume.
- Pseudocumene (1,2,4-trimethylbenzene) is used as a scintillant and contributes 4.1% of the volume.
- Two wave-shifters: PPO (2,5-diphenyloxazole) that contributes 0.091% and bis-MSB [1,4-bis(2-methylstyryl)] with 0.0013% These wave-shifters shift the peak of scintillation light emitted from 375 nm to 425 nm (from UV region of the spectrum to violet-blue region of visible light).

- Anti-static agent (Stadis-425) contributes 0.0003%. It increases the conductivity of the liquid scintillator.
- Anti-oxidants (Vitamin-E) contributes 0.0010%

Sixteen PVC cells are extruded together as a group as shown in Fig. 2.14. Two extrusions of this kind glued together to form a module.

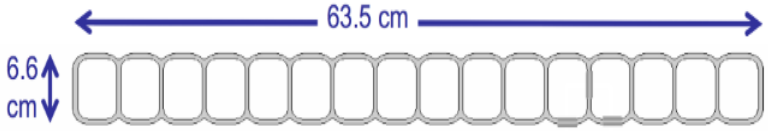

Figure 2.10: This diagram shows the extrusion of 16 PVC cells. Looped WLS fiber runs perpendicular to the page along the length of each PVC cell. Ref. [77].

The inner surface of the PVC cell has titanium dioxide (TiO_2) to maximize the reflection of the scintillated light inside the cells and thus maximize the absorption of WLS fiber. The WLS fibers are designed to maximize the absorption of the emitted scintillation light and to carry this signal to the electronics readout. The WLS fiber is of a diameter of less than 0.7 mm. The core of it is made up of polystyrene with a fluorescent dye (R27) to shift the light to the blue-green region (520 nm wave-length) of the electromagnetic spectrum. The core is surrounded by two acrylic layers designed to minimize the signal loss.

The modules of PVC cells as discussed above are glued side by side to form a plane of the detector. A normal vector from the detector plane aligns parallel to the beam direction. Two consecutive planes are arranged in such a way that a vector drawn through the length of the cells in the consecutive planes are perpendicular to each other and also perpendicular to the beam direction (taken as Z-axis). Usually, the down-up direction of the detector is taken as Y-axis and the perpendicular direction to Y-axis and Z-axis is labeled as X-axis. These alternate plane configuration in the NOvA detector helps to get a three-dimensional (3D) view of the detector (refer Fig. 2.11). This three-dimensional view can be interpreted

as a combined view from two 2D planes: one from the XZ plane and other from the YZ plane.

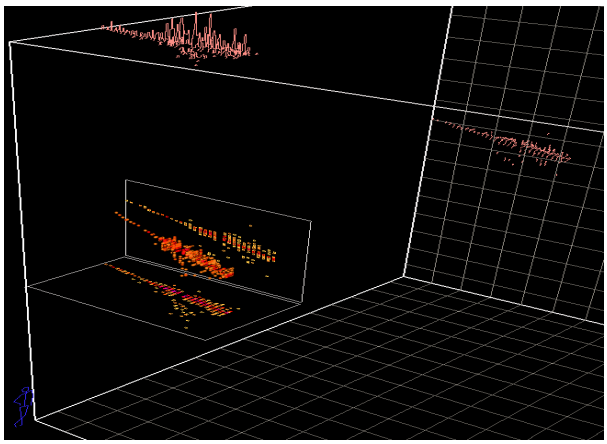

Figure 2.11: Event displays that went with NOvA's announcement of first 3D tracks recorded in the detector. The event is a cosmic ray muon with a large bremsstrahlung shower about 1/2 into its track.

2.2.2 Avalanche Photodiode

The avalanche photodiodes (APDs) are used as photon multipliers in the NOvA detector instead of PMTs[1]. The selection of APD over PMT is dependent on two factors: firstly, the high quantum efficiency of APD (85%) and secondly the APD response is optimum for the wavelength carried by the WLS fiber to electronics (520 nm-550 nm)

[1]The photon multiplier tubes, that commonly used in many other neutrino experiments

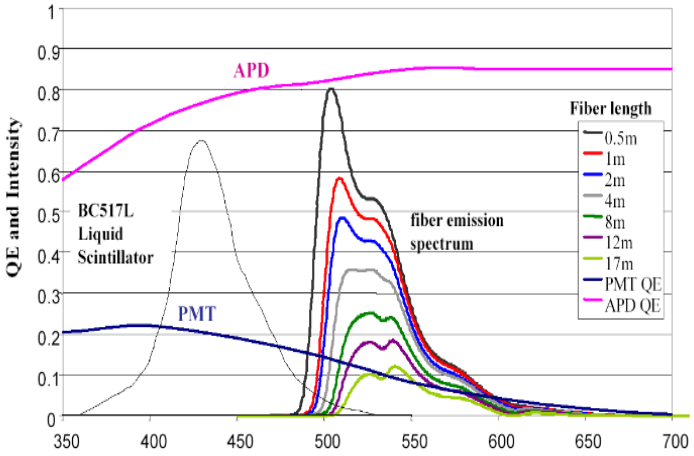

Figure 2.12: This plot shows the comparison of quantum efficiencies of APD and PMT. Also the attenuation length of different colors in WLS fiber as a function of wavelength. Light black line indicates the spectra emitted by the liquid scintillation before wave-shifting applied. Taken from Ref. [77].

NOvA uses the Hamamatsu APD. A reverse biased voltage is applied across the APD to get the photons multiplied. An APD can collect data from 32 cells. Data from each cell is fed to a specific pixel of the APD. The two open ends of the WLS fiber are fed to the one of the 32 pixels of the APD. So each cell corresponds to a particular pixel in the APD. There are some potential sources of noise in APD, such as dark current. Thermal excitation in the APD that creates electron-hole pairs is responsible for the dark current noise. To get away from this, a thermoelectric cooler (TEC) is implemented to keep the temperature of APD at -15^{0}C. A water cooling system that constitutes circulating chilled water is used to take away heat from the TEC. APD is coated with transparent plastic to keep it clean. Also, circulating dry air keeps the moisture away.

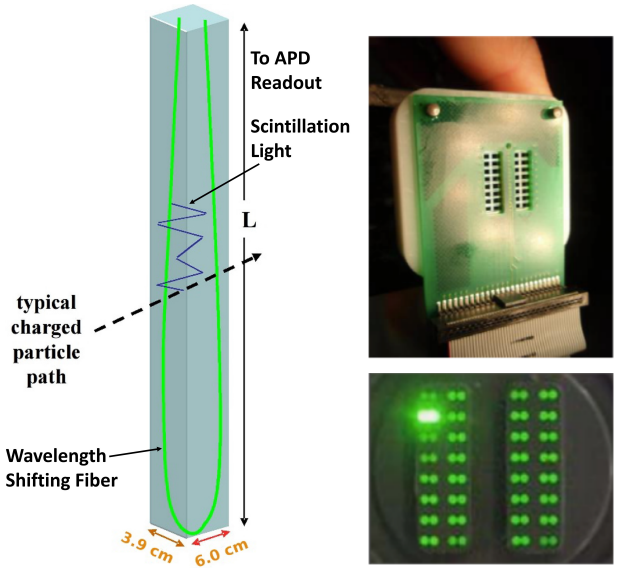

Figure 2.13: The left cartoon shows the two open ends of the WLS fiber which carries the signal from the scintillator to a pixel in APD. The right top plot shows 32 pixels of APD. The right bottom plot shows how the signal from a particular cell as seen by the APD (Ref. [77]).

The output signal from the ADC is processed through the electronics in the FEB (front end board). This processing include:

- Integrating and shaping the signals from each APD pixel – using Application Specific Integrated Circuit (ASIC).
- Converting analog signals to digital signal – using Analog to Digital converter (ADC).
- Determining whether the output of ADC is a signal or not, based on pulse height – using the Field Programmable Gate Array (FPGA).

The output of ADC is fed to FPGA to determine if it is a signal or not. A threshold for the pulse height is set to tag it as a signal. The setting of a threshold is a delicate balance in the sense that it should be high enough to capture the real physics and also should be reasonably low to harvest the signal from the far end of the 15.5 m long cells. The threshold is set 4σ at FD and 5σ at ND, above the root mean square of the noise spectrum.

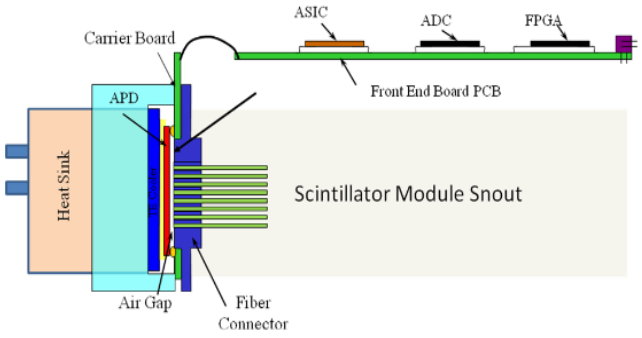

Figure 2.14: This diagram shows the APD and FEB.

The signals from 64 FEB's are collected at Data Concentrator Module (DCM). The data from DCM are stored in a 50 μs block and is called microslices. Which is then transfered to temporary data storage places called data buffer farms in blocks of 5 ms called millislices. The data in time with the beam spill or passed the trigger definitions passed to the permanent storage. In the storage area, data is well arranged into runs and "subruns" to collect data obtained with a specific detector configuration and condition for future analyses.

2.3 A Side by Side Comparison of ND and FD

As we have seen already, the ND placed at 100 m below the ground and is one km away from the target. As a result, it observes much less cosmic activity than the FD. Since FD is at the ground level, it faces 150 kHz of cosmic influx. But at the same time, the ND is close to the beam source and it sees multiple beam events in a single beam spill, so it has a large amount of data. For this reason, the ADC sampling time of ND is less than that of FD. Also for ND, each run consists of 24 subruns while for FD, it is 64 subruns per run [2]. The differences between ND and FD are summarized in Table 2.1 and shown diagrammatically in Fig. 2.15.

[2]NOvA groups events into a hierarchy called "run" that contains zero or more subruns and a subrun contains zero or more events.

Detector variable	FD	ND
Detector Weight	14 kt	0.3 kt
Number of Planes	896	214
Number of Cells	344064	20192
Detector Dimension	59.6×15.8×15.8	15.8×4.2×4.2
Cell Depth	5.6 m	5.6 m
Cell Width	3.6 m	3.6 m
Cell Length	15.2 m	3.8 m

Table 2.1: Comparison of the NOvA ND and FD.

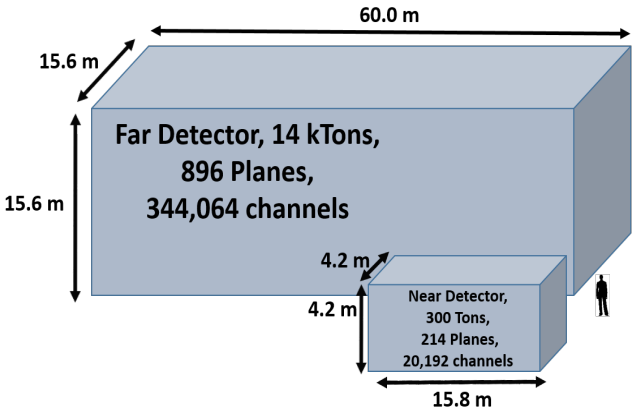

Figure 2.15: This cartoon shows a comparison of size of ND and FD. A human size is also shown for the purpose of understanding the scale.

3

Calibration and Reconstruction

The detector calibration and event reconstruction procedures translate the energy deposited in the detector to a meaningful neutrino interaction energy for doing the analysis. The response of the detector to the energy deposition depends on many factors such as the type of particle and its energy, the distance from the hits to the readout electronics, yield of the liquid scintillator, quantum efficiency of the APDs and the amount of dead materials through which the particle is traveling. We have to account for the effect of these factors in our simulation.

3.1 Calibration of the Detector

The information we are getting out of the detector is a collection of hits those are above a threshold value. The first task is to tag these "rawhits" with a meaningful unit of deposited energy. We have to have a uniform response across a single detector and also between the detectors. Signals reaching at the external electronics from different part of the PVC cell through WLS fiber cannot be treated in equal footing, as the photons collected from the far end of the electronic readout is subjected to more energy loss than that collected in the vicinity of the readout. As the NOvA ND is way smaller than the FD, the ND PVC cells are much shorter. The calibration process can be broadly classified into two parts. They are:

- Relative Calibration – This makes appropriate modification to the energy of photons to attain uniformity in the detector response throughout a detector.
- Absolute Calibration – This converts the relatively calibrated photon energies into meaningful units of energy (GeV).

3.1.1 Relative Calibration - A Closer Look

Relative calibration process accounts for the threshold effects, shielding effects and attenuation in the WLS fibers, and this makes a uniform response throughout a detector. It converts PE (photo-electrons) in ADC signal to PECorr (photo-electrons corrected). If the relative calibration comes across two equal signals collected from different regions a PVC cell, it produces two equal PECorr signals irrespective of their spatial distribution.

In the NOvA detector, cosmic muon is used as a calibration source. These cosmic muons are reconstructed using the tracking algorithm and they are selected using a series of quality cuts. Hits from cosmic muons that enter and exit the detector are used for the relative calibration. The muons are MIPs[1] (Minimum Ionizing Particles) in the NOvA detector. So they have a well characterized energy and have a well known dE/dx (average energy lost per distance). The energy deposited in a hit belonging to a reconstructed track is normalized by the path length in a cell. Since the path length on a cell by cell basis can be difficult to estimate as it depends on the angle with which the particle traversed. Most of the calibration uses tricells, ie. the cellhits where both the adjacent cells in the plane are also triggered by the same cosmic ray as shown in Fig. 3.1. This selection ensures that the particle entered through the top wall and exited through the bottom wall of that cell and it constrains the path length to be the cell height, corrected by the direction cosine in that view.

[1]The muon energy deposition in NOvA is near the minimum of the Bethe-Bloch curve and their dE/dx is well understood

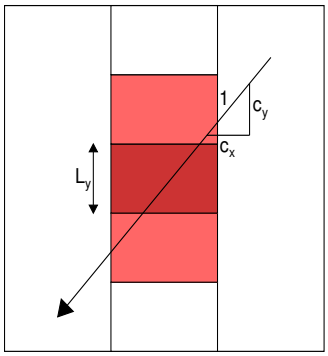

Figure 3.1: Figure shows a tricell(dark) and associated cells(light color) triggered by a particular cosmic track. The path length is calculated as L_y/c_y.

W is used to denote the distance between the location of energy deposition and the location of electronic readout in a cell. Now W is assigned to be zero at the center of a cell. Thus the W can have positive as well as negative values depending on whether the point is close to the readout (positive) or far end of the readout (negative).

Threshold Correction

The threshold and shielding effects should have corrected under the relative calibration procedure. The threshold effect accounts for the inability of a signal to register a hit in the electronic readout. At the same time, shielding effect is the self-shielding of the detector by its own mass, which can lead to a non-uniform muon energy deposition across the detector.

These effects alter the total true energy deposited in a cell. Hence we want to correct these effects using the Monte Carlo (MC) simulation. A correction factor T is defined as $\left(\frac{PE}{\lambda}\right)\left(\frac{E_{\text{True}}}{E_{\text{MIP}}}\right)$, is calculated for correcting these effects. Here the ideal scenario is put in the denominator (a case where there is no threshold and shielding effect) whereas the numerator is the real life case (threshold and shielding effects are present). Here PE is the number of photo-electrons observed while λ is the number of photo-electrons without any loss. Similarly E_{True} is the true energy deposited which includes the shielding effect, and E_{MIP} is the MIP energy without

any loss.

Attenuation Correction

Attenuation of the signal occurs during its propagation through the WLS fiber to the readout electronics. In this method, tricell hits for a particular cell is fit with an exponential function which deals with the attenuation of the signal that reaches both ends of the looped fiber.
The exponential is of the form,

$$y = A + B\left(\exp\left(\frac{W}{X}\right) + \exp\left(\frac{-L+W}{X}\right)\right). \tag{3.1}$$

where L is the length of a cell. A, B and X are free parameters and $W = 0$ is the point that makes a PVC cell into equal halves along its length. The hits near and the farthest end of the readout are treated differently. These end regions behave differently from the active region of the cell. The motivation for doing this is, the ends of the cells are black and some photons are getting absorbed by the walls in contrast to the active region (where photons are reflected well from the PVC cell walls). The fitting function used here is,

$$f(x) = \begin{cases} 1 - \alpha_R(W - W_R)^4, & \text{if } W > W_R \\ 1 - \alpha_L(W - W_L)^4, & \text{if } W < -W_L. \end{cases} \tag{3.2}$$

Here α_R and α_L are constants, and W_R takes a positive value and W_L negative. The product of these two equations gives the full fit function. In the case where considerable residuals are observed in the cell, the product which we have mentioned would not fit well with the data. In this case, a LOWSS (Locally Weighted Scatter plot Smoothing) [83] fit is done.

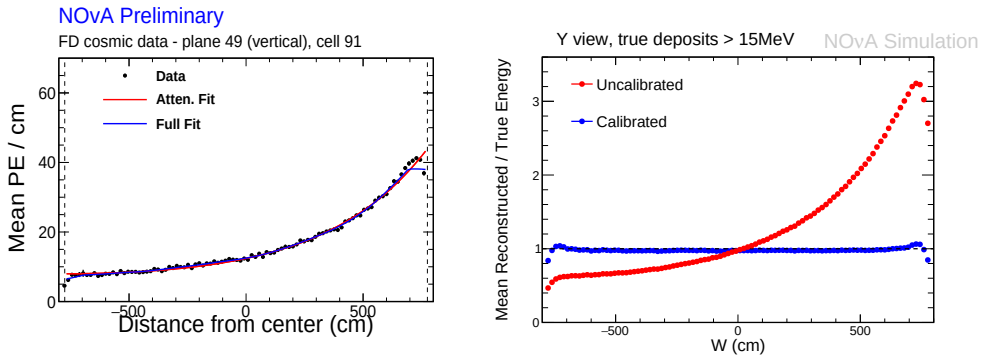

Figure 3.2: The method of attenuation correction. Left: The data is fitted with the simulated detector response per centimeter as a function of W in a cell. The blue curve is with Locally Weighted Scatter plot Smoothing (LOWSS) and red is without it. Right: The comparison of simulated reco/true as a function of W with and without calibration.

3.1.2 Absolute Energy Scale Calibration

Absolute energy correction is the final process in the calibration chain. It is done for both detectors. The goal of this correction is to convert signals that already passed through the relative calibration steps, to the meaningful units of energy. In short, the PECorr got after the relative calibration is converted to GeV or MeV. Cosmic muons that stop inside the detector are used as a calibration source for the absolute calibration. The stopping muon distribution is shown in Fig. 3.3. The dE/dx at the end of these muon tracks is used for the absolute energy calibration. The 100-200 cm region from the end of the track is used for the study as its dE/dx is well characterized by the Bethe-Bloch curve (Ref. [84]). The PEcorr is converted to the meaningful energy unit (GeV) by the help of an energy correction factor. Fig. 3.4 shows the absolute energy calibration process.

$$\text{Absolute energy correction factor} = \frac{\text{PECorr/cm from data}}{(dE/dx) \text{ from the MC simulation}} \tag{3.3}$$

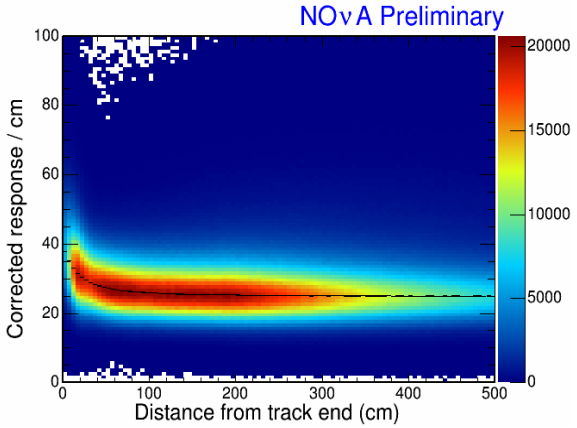

Figure 3.3: Each entry in the histogram is from a tricell hit on a stopping muon track. The Y-axis shows the path normalized attenuation corrected detector response. The X-axis shows the distance to the stopping point of the muon track. The black fit curve shows the mean of a fit to the peak of the attenuation corrected detector response at particular distance from the track end.

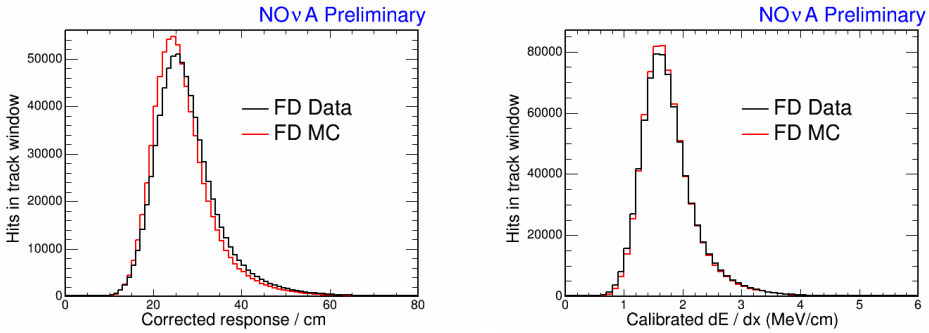

Figure 3.4: Left: Uncalibrated PEcorr/cm distribution of tricell hits within the track window. Right: Calibrated dE/dx in units of MeV/cm after the correction factor is applied.

3.2 Neutrino Event Reconstruction

The event reconstruction in NOvA is a chain of processes in which the calibrated "cellhit" level information is translated into a meaningful fundamental interaction. NOvA uses a jargon "cellhits" to represent recorded

energy deposition in the detector in a 550 μs time window [85]. The recorded energy deposition during this time window can be from a signal (meaningful fundamental interaction) or a noise. The reconstruction should be able to distinguish between these two kinds of cellhits. Sometime there may be multiple physics activity in a data event; multiple neutrino interactions in the ND and cosmic activity in the FD are two examples. The process of separating these interactions is named as "slicing" and each physics interaction is called as a "slice" in NOvA. Even though the slicing algorithm separates signal and background, multiple fundamental interactions can have clusters of hits that are overlapped spatially or temporally, and slicer has some limitations . The Slicer4D [86] algorithm is designed to separate these complicated interactions.

In the NOvA detector, cellhits are recorded into two spatial coordinates: XY and YZ. The event reconstruction helps to attain a three-dimensional manifestation of the fundamental interaction by combining information from both of these coordinates. The major steps in the NOvA event reconstruction are:

- Grouping cellhits based on the spatial and temporal information.
- Locating the event interaction vertex.
- Further grouping of cellhits to reconstruct the activity of the neutrino interaction products.

In the NC disappearance analysis, we make use of the strategy which is developed to reconstruct events in both the ν_μ analysis and the ν_e analysis. For the ν_μ analysis [87], the reconstruction strategy is muon-centric. As the distinct signature of a ν_μ interaction is a long muon track, the main focus of this reconstruction is on the track-like features. At the same time, the ν_e analysis [88] event reconstruction is designed to well reconstruct shower-like features. Fig. 3.5 shows how ν_μ, ν_e and ν_τ events look like in the NOvA detector.

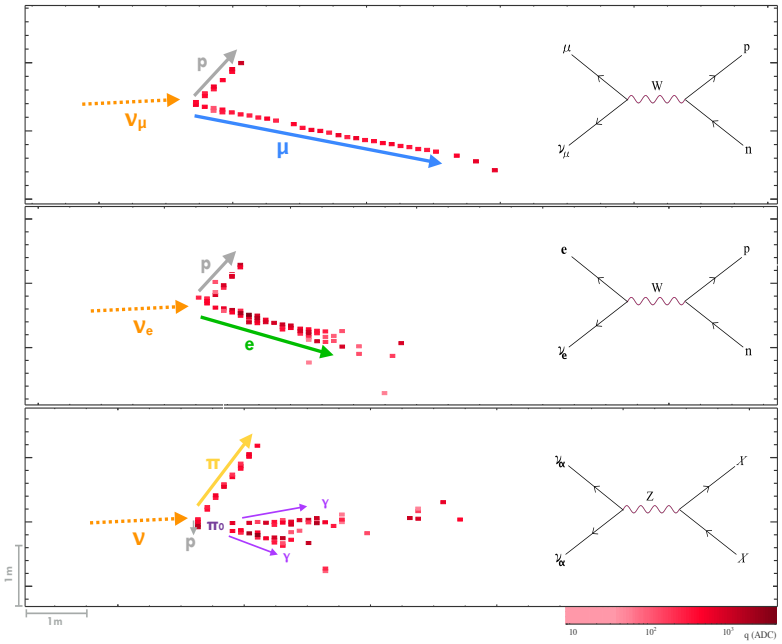

Figure 3.5: Example event topologies of ν_μ (top), ν_e (middle) and NC (bottom) events.

This section follows the process listed in Ref.[85].

3.2.1 Density Based Clustering

The calibrated cellhit is the only input to the event reconstruction algorithm. Grouping of these cellhits according to their spatial and temporal information is called clustering. The process of clustering starts with looping through each cellhit to find the so called core point. The core point is the cellhit with which at least a minimum number of neighbor hits within a threshold "distance" called critical distance. The distance function used can be written as,

$$D = \left(\frac{|\Delta T| - |\Delta \vec{\boldsymbol{r}}|/c}{T_{\text{res}}}\right)^2 + \left(\frac{\Delta Z}{D_{\text{pen}}}\right)^2 + \left(\frac{\Delta XY}{D_{\text{pen}}}\right)^2 \tag{3.4}$$

and this function defines the neighborhood of two cellhits. Here T_{res} is the timing resolution of hits summed in quadrature. The majority of particles passing through our detector should be treated using relativity

since their velocities are close to that of light. In the first term of Eqn. 3.4, ΔT is the difference in recorded time between two cellhits, $\Delta\vec{r}/c$ denotes the relativistic term; where $\Delta\vec{r}$ represents the 2D separation between two cellhits and c is the velocity of light. The distance penalty is represented as D_{pen} and is a tunable free parameter. The ΔZ and ΔXY are separations in each view. For hits in opposite view, ΔXY=0 and D_{pen} takes a smaller value. The ultimate goal of the slicer algorithm is to isolate a neutrino interaction completely into a cluster. The performance of the algorithm is represented as completeness and purity of the clustering,

$$\text{Completeness} = \frac{\text{Energy from interaction deposited in slice}}{\text{Total energy from interaction deposited in detector}} \tag{3.5}$$

and

$$\text{Purity} = \frac{\text{Energy from interaction deposited in slice}}{\text{Total energy in slice}}. \tag{3.6}$$

An example slice is shown in Fig. 3.6. The next step in the reconstruction chain is to sort out the features in a particular slice and it is done using Hough Transforms.

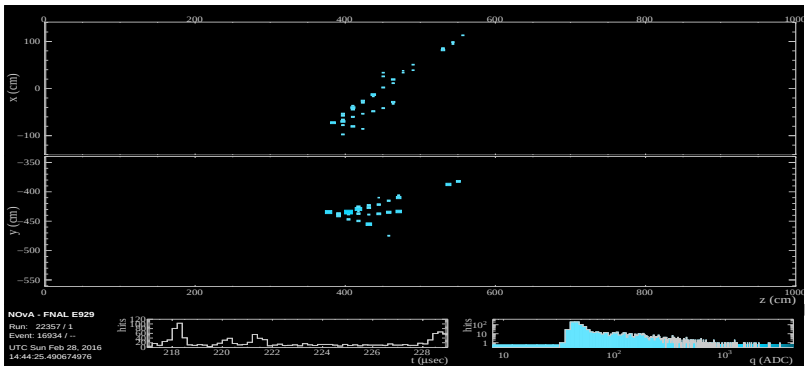

Figure 3.6: A filtered slice in FD. Here the hits from other slices are grayed.

3.2.2 Hough Transform in NOvA

Hough Transform is widely used in the image processing to find features out of an image. We make use of the basic principles of Hough Transform in NOvA reconstruction to find features out of clustered cellhits (Ref.

[89]). This algorithm gives a set of lines whose direction and point of intersection can be used to get a seed for the algorithm which finds the interaction vertex. Each line segment created between two cell hits is translated into polar coordinates in each detector view. The algorithm works in each detector view separately, filling a 2D Hough space in the coordinates ρ and θ with a Gaussian smeared vote for each hit pair. Peaks in the Hough space map are identified as coordinates of a line. A threshold for the peak identification is set for the noise separation.

3.2.3 Vertex Identification with Elastic Arms

The vertex identification is the process of reconstructing the interaction point of a neutrino event. All the particles produced as a result of the neutrino interaction are supposed to be outgoing from this particular point. This algorithm fit a set of lines through the cellhits in a slice to find a common point of origin. An example is shown in Fig. 3.7.

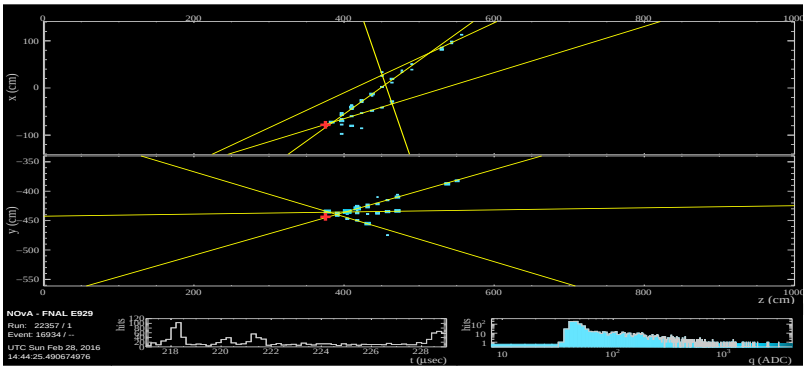

Figure 3.7: Example of filtered slice in the FD. The golden lines are the reconstructed Hough lines. The red cross is the reconstructed elasticarms vertex.

Ref. [90] explains more about the vertex identification with elastic arms in NOvA.

3.2.4 Fuzzy-k Prong Reconstruction

The Fuzzy-k prong reconstruction algorithm is employed to subcluster the cellhits in a cluster. Each subcluster is supposed to come from a particular product from the neutrino interaction. The word Fuzzy-k points to the

fact that the algorithm let multiple prongs to share a single cellhit and as a result, the boundary between the prongs is fuzzy. An example of Fuzzy-k prong is shown in Fig. 3.8.

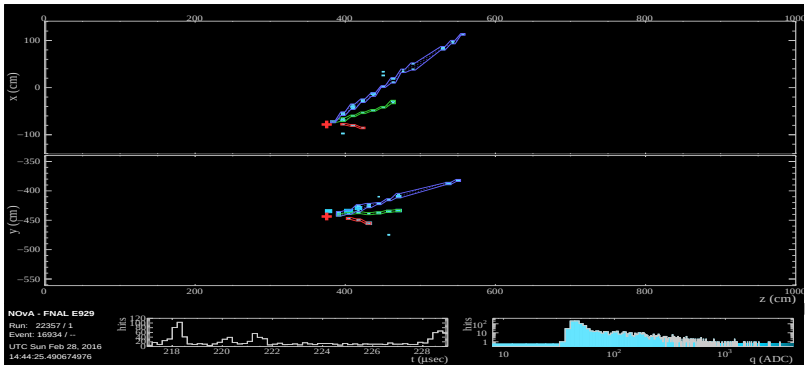

Figure 3.8: Example filtered slice in the FD. The blue, green and red regions are the reconstructed Fuzzy-k prongs. The red cross is the reconstructed elasticarms vertex.

3.3 NC Energy Estimation

The NOvA detectors are tracking calorimeters and are made up of PVC cells filled with liquid scintillator. The event topology of the CC events and the NC events are distinct in the sense that the NC events do not have an energy deposition in the detector by the lepton component (for NC events, the lepton component is the outgoing neutrino which carries a fraction of event energy). In contrast to NC events, CC events have leptons (muons, electrons or tau particles) which deposit energy in the detector, or they are "visible" in the detector. The response of the detector is also different for hadrons and leptons. In the 2017 FHC analysis, we have corrected the slice calorimetric energy (the reconstructed energy, with general calibration) against the "true visible energy"[2]. This does not take into account the energy lost in the detector material.

In the 2019 RHC analysis, we corrected the slice calorimetric energy against the true value of "energy deposited" in the detector that considers the true energy lost in the detector too. The Bjorken-y gives the fractional

[2]The difference between the true energies of the incoming neutrino and outgoing neutrino in a particular NC interaction.

energy loss of the neutrino. Multiplying the true neutrino energy with Bjorken-y gives the "true estimate" of energy deposited in the detector. This true energy deposited is the parameter which is used for correcting the slice calorimetric energy. We have used the jargon, "Energy Deposited in the Scintillator" or "Energy Deposited" to represent the corrected slice calorimetric energy.

Since the general strategy is the same for the neutrino and antineutrino analyses, here we will discuss only the procedure followed in the 2019 RHC analysis. The true energy, true visible energy, slice calorimetric energy and true energy deposited in the detector for FD FHC, FD RHC, ND FHC and ND RHC are shown in Fig.3.9.

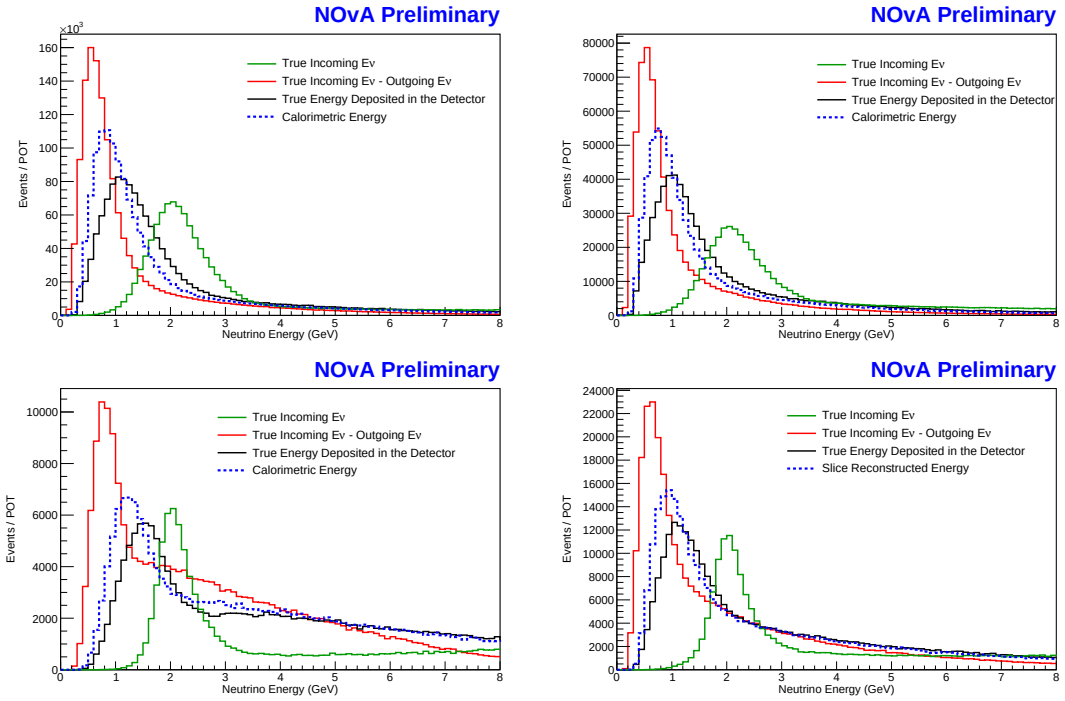

Figure 3.9: Comparison of different "energies"(with standard NC selection excluding the energy cut), ND FHC (left) and ND RHC (right) in top row and FD FHC (left) and FD RHC (right)in bottom row.

3.3.1 The Methodology

The slice calorimetric energy is now compared with the true energy deposited in the detector for NC selected events.

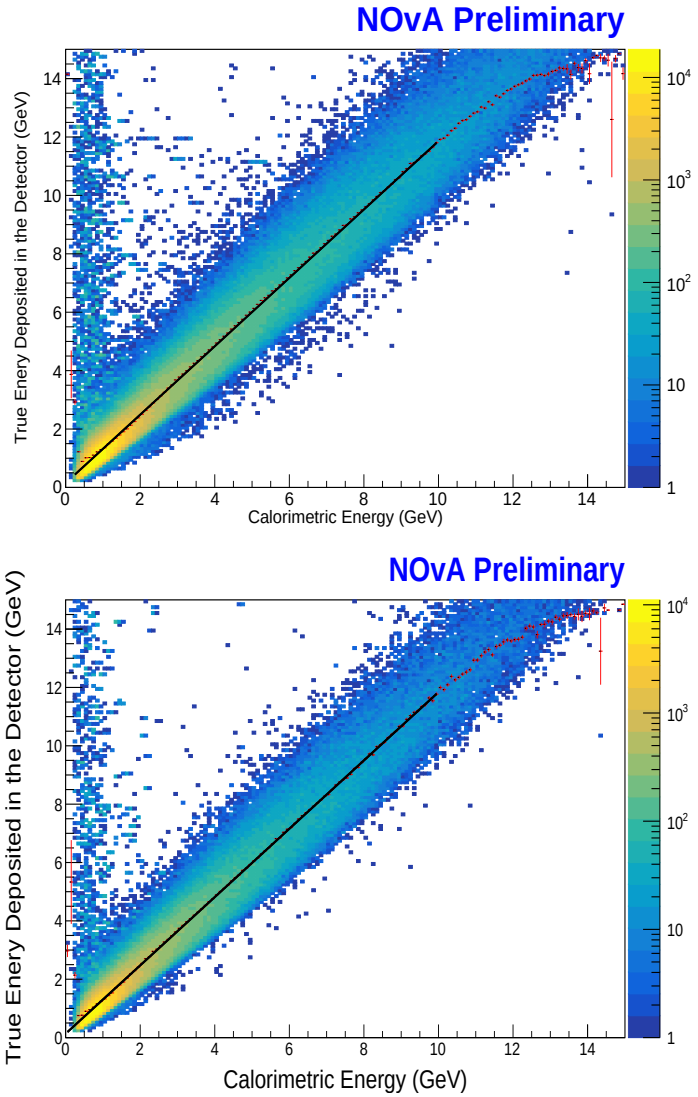

Figure 3.10: The slice calorimetric energy vs the true energy deposited in the detector plot for ND FHC (ND RHC) sample is shown on top (bottom). The profile along the Y-axis shown with red points. The color is shown on a log scale. It is fit with a line.

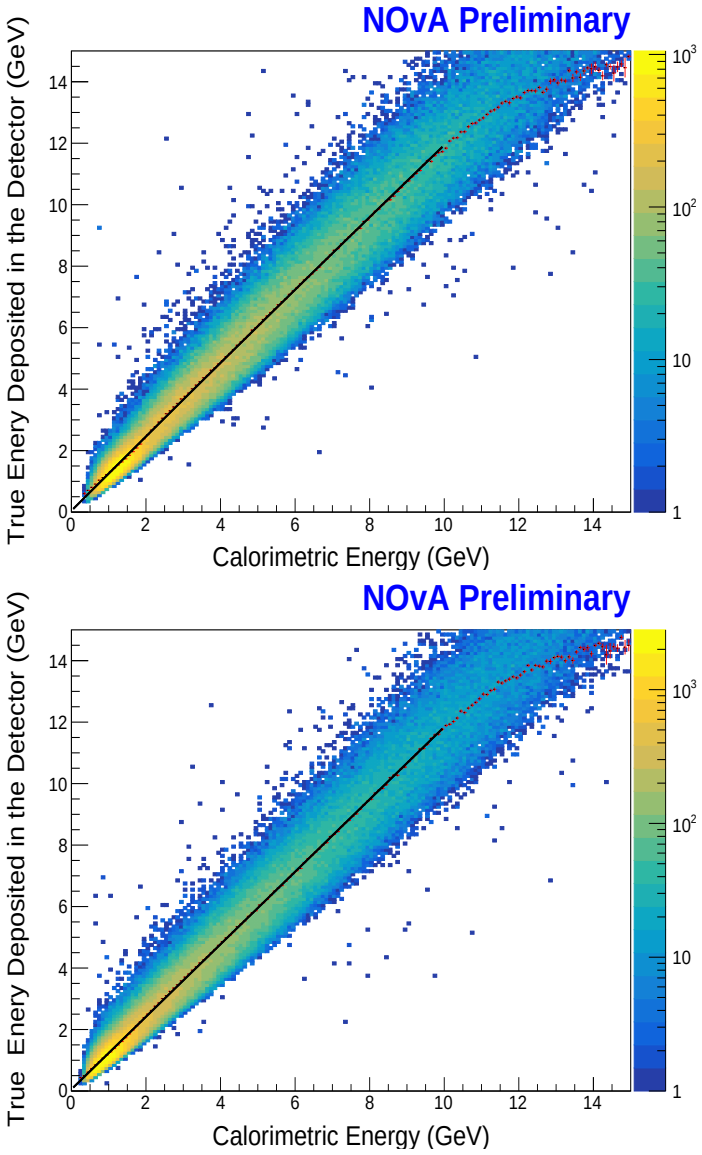

Figure 3.11: The slice calorimetric energy vs the true energy deposited in the detector plot for FD FHC (FD RHC) sample is shown on top (bottom). With standard FD NC selection, excluding the energy cut. The profile along the Y-axis is represented with red points. The color is shown on a log scale. It is fit with a line.

Figs. 3.10 and 3.11 are made with the slice calorimetric energy on the

X-axis and the true energy deposited in the detector on the Y-axis. The plot is profiled over the Y-axis and then the profile histogram is fit with a line. Fig. 3.10 is for the ND and Fig. 3.11 is for the FD. The value of the slope gives the constant correction factor to be applied to the slice calorimetric energy.

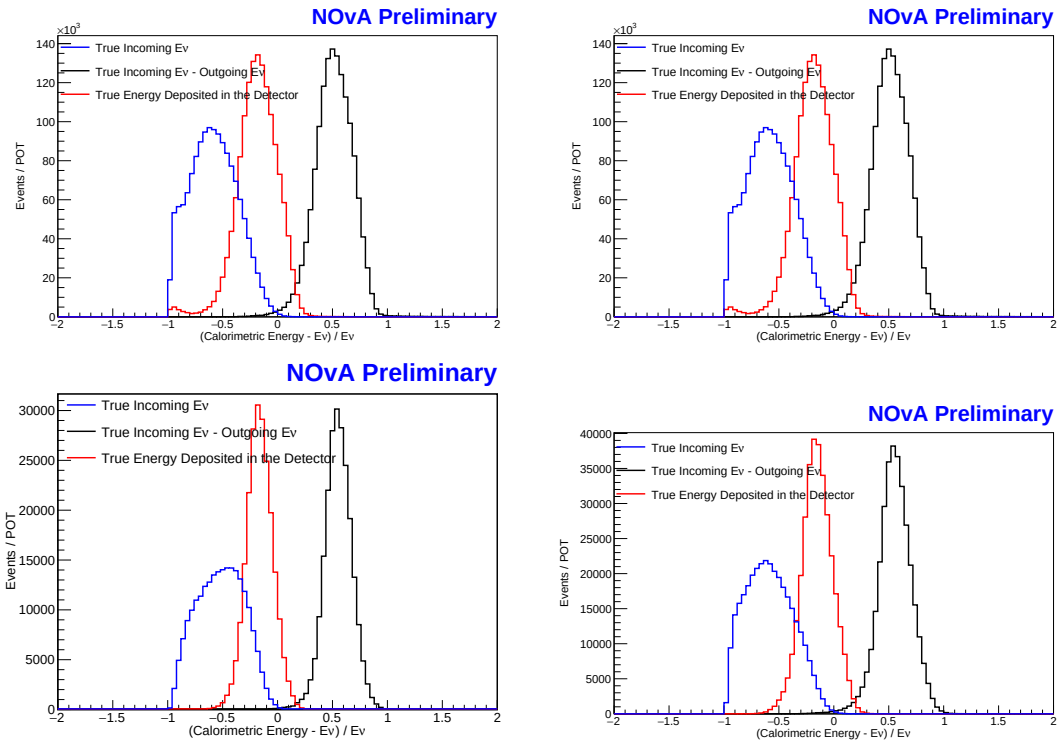

Figure 3.12: Comparison of different "energy resolution", ND FHC (left) and ND RHC (right) in the top row and FD FHC (left) and FD RHC (right) in the bottom row. In the X-label of each plot, "Energy" means: true energy for the blue line, true visible energy for the green line and for red is the true energy deposited in the detector. As we do not try to correct for the outgoing ν_μ, we expect the true E_ν to be biased.

$$\text{Slope of the line} = \frac{\text{True visible energy}}{\text{Slice calorimetric energy}} \tag{3.7}$$

The correction factor calculated are shown below:

- The ND FHC NC selected events = 1.15.
- The ND RHC NC selected events = 1.11.
- The FD FHC NC selected events = 1.18.
- The FD RHC NC selected events = 1.20.

3.3.2 Applying the Correction

The fractional energy resolution is used to compare the resolution before and after the energy correction, and the fractional energy resolution before correction =

$$\frac{\text{Slice calorimetric energy} - \text{True energy deposited in the detector}}{\text{True energy deposited in the detector}}. \quad (3.8)$$

When the uncorrected calorimetric energy is equal to the true energy deposited in the detector, we get an ideal case of zero fractional energy resolution. But from Figs. 3.10 and 3.11, it is clear that we have underestimated the slice calorimetric energy. So we have to scale its value up. For example, the slope is 1.11 for the ND RHC and so, the slice calorimetric energy when multiply with 1.11 yields the true energy deposited in the detector. The fractional energy resolution after correction can be seen as,

$$\frac{1.11\times \text{ Slice calorimetric energy} - \text{True energy deposited in the detector}}{\text{True energy deposited in the detector}}. \quad (3.9)$$

3.4 Monte Carlo Simulation in NOvA

Irrespective of whether it is a precision measurement experiment or a parameter estimation experiment, simulation of the experimental data plays an important role. In the NOvA experiment, the simulation is a chain of processes which constitute the simulation of the interaction of the protons with the graphite target (p-C interaction), the secondary and tertiary interaction of the hadronic products, propagation of neutrinos produced through the NuMI beamline, interaction at the detector, simulation of the transport of photons through the WLS fiber and the simulation of the

signal coming out of the electronics part of the detector. The simulation of interaction in the detector is carried out with the use of GENIE (Generates Events for Neutrino Experiments) package and the Geant4 package is used for simulating of the propagation of the interaction products through the medium. This simulation package uses an extensive list of physics interaction along with the environmental parameters like the cross section, geometry, etc. The high statistics of simulated data reduce the statistical uncertainty.

3.4.1 Flux Simulation

The simulation of NOvA flux starts from simulating the collision of high energy protons at the graphite target. The next stage is the simulation of the propagation of the mesons produced, through the NuMI beamline. The simulation package used for this purpose is known as G4NuMI, which is an adaptation of Geant4. This makes use of physics models such as FRITIOF Pre-compound model and Bertini Cascade model for the primary hadrons having energy below 20 GeV. In reality, the interaction of protons on the target produces a shower of hadronic particles. A data-driven technique based package called PPFX (Package to Predict Flux) [91] was developed for the Fermilab cross section experiment MINERvA. The hadronic data in p-C interaction was used in developing the PPFX package [92]. As MINERvA uses the NuMI beamline, the PPFX package can be used to constrain the systematic uncertainties in the beam simulation in other experiments which makes use of the NuMI beam like NOvA. The NOvA flux is shown in Fig. 3.13.

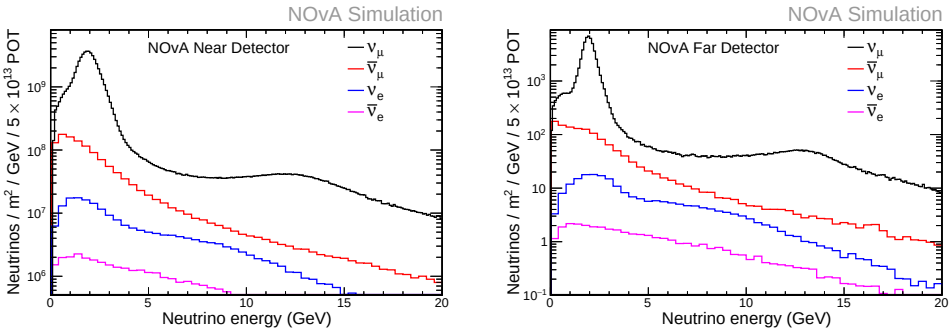

Figure 3.13: Predicted ND MC composition based on PPFX, in the ND (left) and in the FD(right).

The next part of the flux simulation is the propagation of the particles created. The Geant4 [93] is widely used in the HEP experiments to simulate the propagation of the particles through a given geometrical model. The NOvA specific geometrical model consists of modeling of NuMI beamline with magnetic horns, decay pipe, hadron monitor, absorber and muon monitor. By inputting the geometrical model information, we would get G4NuMI flux files. Which is essentially a ROOT file with saved parent and grandparent information of each neutrino event entry. Neutrino parent distribution at the ND for neutrino beam (FHC) and antineutrino beam (RHC) are shown in Fig. 3.14.

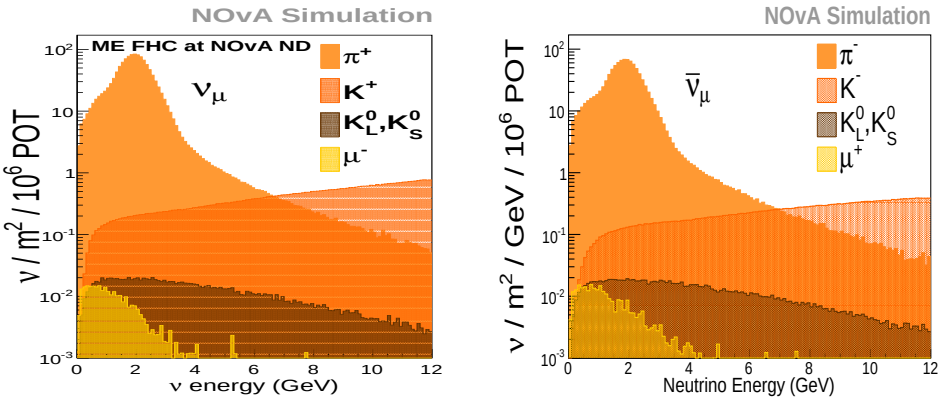

Figure 3.14: Parent information stored for neutrinos in the flux files, for FHC beam (left) and RHC beam (right).

3.4.2 Interaction Simulation

Neutrino interaction simulation is carried out by the GENIE [94, 95] simulation package. GENIE takes G4NuMI neutrino flux along with the neutrino cross sections to deliver different types of neutrino interactions. A specific kind of neutrino interaction is generated depending on the total cross section of that interaction (see Fig. 3.15). The differential cross section is used to determine the particle kinematics in an interaction. The GENIE package takes an extensive list of phenomenological models of particle interaction and constraints from other particle physics experiments. A neutrino interaction inside the detector can be viewed as an interaction of a neutrino with a nucleus, and then the hadrons produced as a result of this interaction further interacts with the nucleons within the nuclear

environment. This is known as the final-state interaction (FSI) and Relativistic Fermi Gas Model is used in the GENIE as the phenomenological model. The INTRANUKE package is used to simulate the FSI. The Cosmic RaY (CRY) package [96] is used for the simulation of cosmic ray particle interaction. For simulating the propagation of neutrinos through the detector, three major physics lists are used in the Geant4 package. They are:

- QGSP (Quark-Gluon String Precompound) to model the de-excitation of the nucleus.
- The Bertini cascade to model the propagation of the primary hadrons below 10 GeV.
- The High Precision neutron package that deals with neutrons traveling with energy below 20 MeV.

The neutrino physics interactions that modeled are categorized as quasi-elastic scattering (QE), resonant baryon production (RES), deep inelastic scattering (DIS), coherent nuclear scattering (COH), and meson exchange current scattering (MEC) [97].

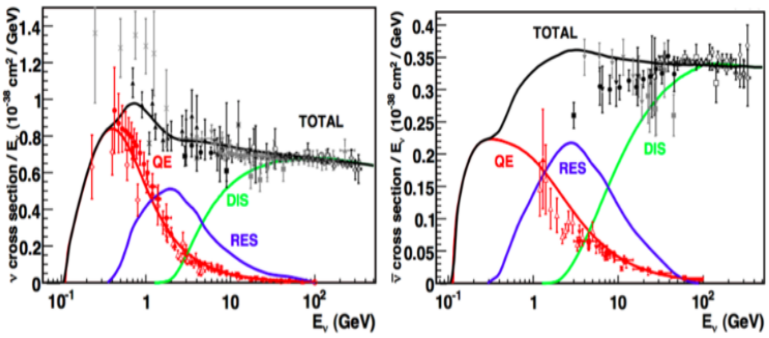

Figure 3.15: Interaction cross section for the neutrinos (left) and antineutrinos (right), with varying energy. This Fig. is taken from Ref. [98].

3.4.3 Detector Simulation

This part of the simulation takes care of how the detector components respond to the GENIE simulated neutrino interaction. The Geant4 package is implemented to simulate the particle transport in the detector.

4

Particle Identifiers in the NC disappearance Analysis

In any experiment, augmenting the selection efficiency and purity of the selected sample is of great importance. In this chapter, we are going to have a brief summary of the primary event selector in NOvA NC disappearance analysis. As we have seen in the previous chapters, the ND is at 100 m below the ground level. So the cosmic ray background is greatly reduced at this detector. At the same time, ND is just 1 km away from the beam source and it witness a huge amount of CC events. As the dominant background to the NC events in the ND is CC events, the primary event selector in the ND should be capable of well separating NC events from CC. We are using a computer vision-based particle identifier (PID) for this purpose and it is termed as the Convolutional Visual Network (CVN). We will discuss more this in the next section.

The NOvA FD is at 810 km away from the beam source and is on the ground level. So it witnesses a shower of particles with a cosmic origin and which can mimic the NC event topology in the detector. At the same time, the rate of CC events at the FD is order of magnitudes lower than the cosmic events. The cosmic events constitute the dominant background in the FD. We employed a Multivariate Analysis Technique [99] based on the ROOT framework [100], ie. the Boosted Decision Tree (BDT), in developing a particle identifier that well distinguishes cosmic events from the beam NC events. A comparison of the breakdown of events between the ND and FD is shown in Fig. 4.1. We will discuss more of the training and implementation of this PID in section 4.2.

The section 4.3 of this chapter is dedicated to demonstrate a FD cali-

bration cross-check using cosmic π^0 as the standard candle. This analysis is one of the example of the application of CVN to select a pure sample of π^0 from a large set of backgrounds.

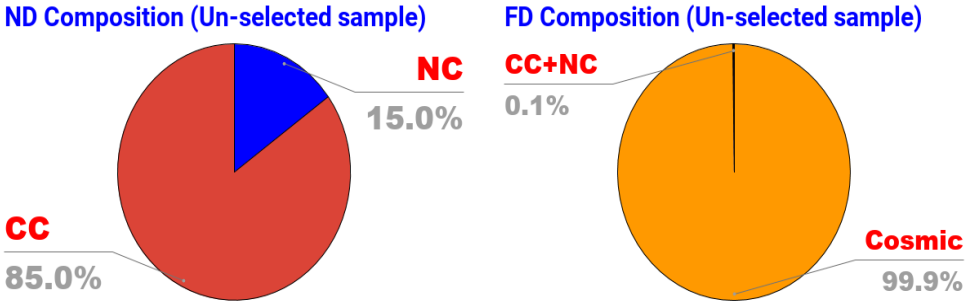

Figure 4.1: Unselected event composition in the ND (left) and FD (right).

4.1 Convolutional Visual Network

4.1.1 An Overview of the Network Architecture

The machine learning algorithms such as k-Nearest Neighbors, Boosted decision trees and Multilayer Perceptrons have been widely used in HEP experiments for a long time. But these are subject to a couple of practical difficulties when applying to experiments like NOvA. Since they use reconstructed events as input, any reconstruction failures lead to the propagation of error through the training process which eventually results in the misidentification of an event. Also, the reconstructed features that used to train the algorithm constrain the ability of the network to separate signals from the background. Because this trained network can only identify an event with the help of the reconstructed features of the event used in the training process.

The traditional neural networks like Multilayer Perceptrons (MLP) generally employ multilayer architecture: an input layer, an output layer and a number of hidden layers in between input and output layers. The MLP approximates the linear transformation function $f : R^n \rightarrow R^m$, which is essentially a mapping from an input column matrix $\overrightarrow{x}$ with dimensionality n to an output $\overrightarrow{f}$ with dimensionality m. Each node output

can be seen as the weighted sum of outputs from all nodes in the previous layer with a nonlinear function as a bias term. The supervised learning method is used to determine the weights and bias term. The variable "loss" is determined by finding the deviation of the output from the "true" output. The back-propagation algorithm is used to find the loss as a function of bias and weight terms. We can tune the loss function with bias and weight as knobs. Stochastic gradient descent method is used for such a tunning.

Some of the practical issues of the traditional neural network can be eliminated by introducing a Deep Learning (DL) architecture. This possesses many layers (multiple hidden layers are sandwiched between the input and output layers) and has been successfully used in the image processing technology. A CNN (Convolutional Neural Network) is capable of extracting features from the low level variables such as clusters or groups of cellhits with definite spatial and temporal correlation. The CNN uses the extracted features to train the network rather than using the high-level reconstructed variables as input. The deep learning architecture is making use of non-saturating rectifying linear units (ReLU) functions (functions that takes the form, $f(x) = max(0, x)$). This replaces the conventional saturating nonlinear functions like sigmoid functions used in the traditional neural networks. In some cases, even if the network works well with the training sample, it can show a different efficiency between the data and MC . This is known as overtraining and when the number of training variables increases, the probability of network to get overtrained increases. The risk of overtraining a CNN is reduced with the help of a process known as dropout, which uses a random subsample of the available network connections in each training iterations.

The NOvA experiment employs a computer vision-based CNN architecture known as Convolutional Visual Network (CVN). Here the input to the network is two 2D views (as shown in Fig. 4.2) of a particular neutrino event. The convolution layer performs a discrete convolution to extract features from an input image. A pooling layer is used to reduce the dimensionality of the feature extracted. It makes use of an architecture commonly known as network in network (NIN), in which the main network contains repeated subnetworks commonly known as an inception module. This NIN approach is adopted from the GoogLeNet [101] architecture, which possess high efficient learning capabilities and dimensional

reduction. In NOvA, we use two parallel architecture one for event X-view and other for the Y-view (see Fig. 4.2). In a later stage, features from each of these parallel architectures add together to get features of both views together.

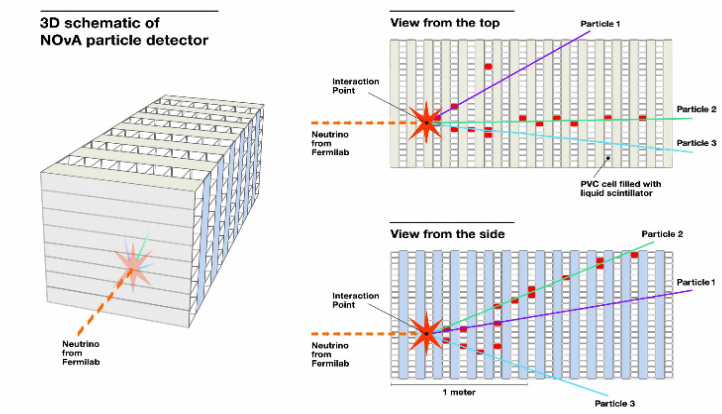

Figure 4.2: The alternating planes of the NOvA detector are perpendicular to each other. This helps to resolve the 3D image of an event into two different views known as X-view and Y-view.

The sum of the classifier outputs is set to one, with the implementation of a function known as softmax function. The details and description of the technical terms used in this section can be found in Ref. [102].

4.1.2 Application of CVN into NOvA Analyses

The neutrino beam interaction in the detector can be broadly classified as the CC (mediated by $W^{\pm}$ bosons) and NC (mediated by Z^0 boson). The CC interactions can be further classified as ν_μ CC and ν_e CC, based on the flavor of the neutrino participating in the interaction. For the NC disappearance analysis, our primary objective in the event selection is to separate NC signal events from CC background events. In many cases, we can distinguish between these interactions just by looking at their topology. The ν_μ CC event is characterized by a long muon track and hadronic shower, ν_e CC characterized by an out going electron and a hadronic signature and NC events are characterized by a hadronic shower with neither e nor μ as primary particle. Examples of these events are

shown in Fig. 4.3. Based on the incoming neutrino energy, interaction may be of the type QE, RES, DIS or MEC. This adds complication to our method of just observing interaction topology and deciding the interaction category.

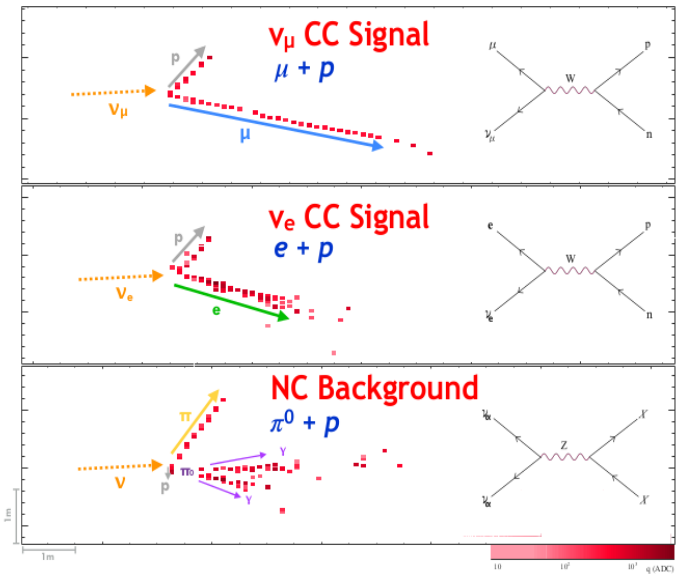

Figure 4.3: Representation of ν_e CC, ν_μ CC and NC events as seen in the NOvA detector.

For the 2017 FHC analysis, the CVN network was trained to distinguish between NC, ν_μ CC, ν_e CC, ν_τ CC and cosmic events. This analysis used 14 simulation-based labels, viz. neutrino flavor type, interaction type, a label for the cosmic event and NC event. $\{\nu_\mu \text{ CC}, \nu_e \text{ CC}, \nu_\tau \text{ CC}\} \times \{\text{QE}, \text{RES}, \text{DIS}, \text{Other}\} + \{\text{NC}, \text{Cosmic}\}$ were the set of labels used in this analysis. Here cosmic label was extracted from the simulated cosmic events.

The CVN used in 2019 RHC analysis is a bit different from the previous analyses. The main difference is in the architecture used and the final-state labels used for the training. Since CVN classification is based on event topology instead of the simulation based labels, it is possible to add cosmic labels by training the network with cosmic events. In order to reduce the dependency on GENIE interaction type labels, primary particles along with the neutrino flavor are adopted as the labels for this analysis. These

labels can be represented with a general form:
Neutrino flavour – Ne – Nν – Nπ^0 – N$\pi^\pm$ – Nn – Np. This line can be interpreted as: as a result of a particular neutrino flavor interaction, N number of different particles are produced. Here N can take values 0, 1, 2, 3, etc. Some examples are:

1. nE – 1e – 0ν – 0π^0 – 0$\pi^\pm$ – 0n – 1p (ν_e CC interaction that yields one electron and one proton).

2. nM – 0e – 1ν – 0π^0 – 0$\pi^\pm$ – 0n – 1p (ν_μ CC interaction that yields one neutrino and one proton).

3. nU – 0e – 0ν – 0π^0 – 1$\pi^\pm$ – 0n – 1p (NC interaction producing one $\pi^\pm$ and one proton).

4. nT – 0e – 0ν – 0π^0 – 0$\pi^\pm$ – 2n – 1p (ν_τ CC interaction that yields two neutron and one proton).

There are 5 more additional labels which accounts for the events that do not come under above list. The categories of neutrino flavors that does not come under above mentioned labels nM_Other, nE_Other, nT_Other. Label kCosmic_PT accounts the cosmic labels when network is trained with the cosmic data. kOther_PT account for NC events that whose primary particles does not come under a specific NC category. A total number of 392 labels are used. Also for this analysis, the network is trained with FHC and RHC data in contrast to the previous analyses which used only FHC data for training the network. The CVN used for this analysis uses improved architecture known as Short Simple, while previous analysis used CVN classic architecture [103]. Performance of the 2019 CVN is shown in Fig. 4.4.

For selecting events for training, preselection and containment selection are used. Details of these selection can be found in Ch. 5, 10% of cosmic data is used for the final training.

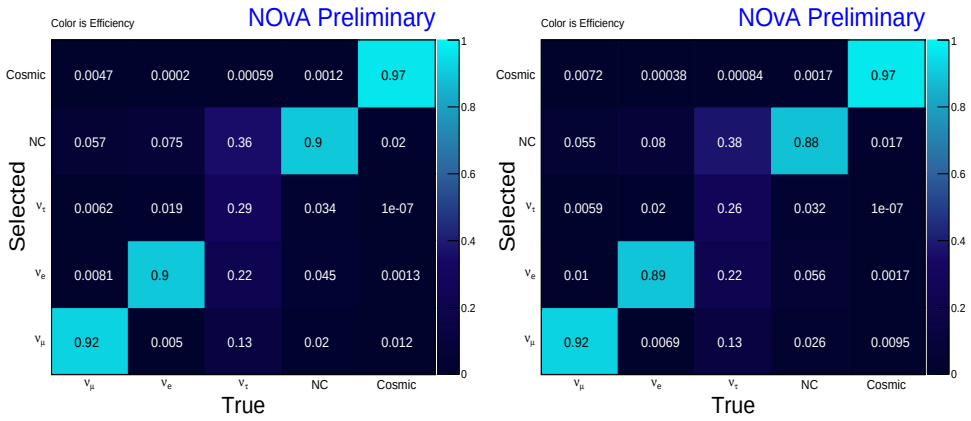

Figure 4.4: The right (left) plot shows the classification matrix for FHC(RHC) for the network trained with FHC(RHC).

We will discuss more about CVN NC classifier in Ch. 5.

4.2 Cosmic Rejection BDT for the NC Disappearance Analysis

The majority of astrophysical particles that enter into the earth's atmosphere are constituted by free protons, α -particle and heavy nuclei. These particles interact with the atoms in the atmosphere and a bunch of secondary particles are produced. They are mainly muons, electrons, positrons, γ -rays, protons and neutrons and a small amount of pions. Due to the huge size and the location of NOvA FD, it is subjected to a massive influx of the cosmogenic particles ("cosmics"). The FD shielded at the top with 6-feet concrete and four inches of Barite to reduce the particles of cosmic origin that penetrate into it [104]. But a fraction of cosmogenic particles, mainly the muons and the neutrons still enter the FD. The FD witnesses an influx of 150 kHz of cosmics.

The event topology of NC is completely different from that of CC in our detector. Since the outgoing neutrino is invisible, the NC event can be identified as a hadronic shower. The major backgrounds in the selected NC signal samples for the NC disappearance analysis is ν_μ CC events with short muon track, ν_e CC events with high slice calorimetric energy, and the energy deposited in the detector by cosmic muons and neutrons. The

cosmogenic neutrons that show up in the detector are mainly produced at the overburden[1] of the detector.

Cosmic Rejection- As an analysis requirement

Comparing the number of NC events and cosmic events, approximately one NC event for 50 million cosmic events is seen in the timing window before applying any selection. Hence removing the events with a cosmic origin is one of the primary objectives in the event selection process for the NOvA NC disappearance analysis. For the first NC disappearance analysis [105], the events in the top 5 m of the FD were removed to avoid the cosmogenic neutron background. The Cosmic Rejection BDT (or simply "BDT") used was designed for the ν_μ analysis [106] and largely aimed to remove the cosmogenic muon backgrounds, so that the input to the BDT was the Kalman track[2] based variables.

In the 2017 FHC analysis, the cosmogenic neutron backgrounds were removed using an improved BDT, so that we could reduce the cut off region at the top of the detector from 5 m to 100 cm. The 2017 FHC BDT training was based on the properties of the cluster of hits reconstructed as showers in an event slice. This helped us to increase the efficiency of the NC selection. For the case of 2019 RHC analysis, the BDT has been trained for each data taking period separately depending on the beam and the detector running conditions. The data taking is divided into four periods. Apart from this, the strategy for BDT training is the same for the analyses that are being discussed in this thesis, i.e the BDT training is based on the properties of event showers. BDT is trained for these four samples separately for this analysis. Here we limit our discussion to the training, testing and implementing BDT for the 2019 RHC analysis.

4.2.1 Cosmic Rejection Strategy

Apart from removing the obvious cosmic backgrounds using cosmic veto in the early stage of the data production, the event selection implements a two-layered strategy to remove dominant cosmic backgrounds.

[1] Concrete and barite on the top of the detector

[2] The muon track reconstruction algorithm used in NOvA.

Removing the Cosmic Backgrounds in Early Selection Stage

The cosmogenic backgrounds are removed by using some specific selection cuts. These include:

- A cut on the transverse momentum fraction. The transverse momentum fraction distribution for the cosmogenic background and the NC signal are different. This cut is correlated to the prong distance from the top of the detector. Events with distances larger than 540 cm are removed if they have a fractional transverse momentum greater than 0.4. This is motivated by the fact that cosmic backgrounds populate at the high end of the traverse momentum fraction distribution in contrast to NC signal events.

- Removing the events which fall in the close proximity of a cosmic event in time or space. The definition of close proximity here is, if they fall within -150 to 50 ns in time and within 500 cm of a slice located less than 100 cm from the top of the detector. This cut removes the neutron activity and the Bremsstrahlung shower (simply "brem") that can be located close to an event spatially and temporally [107].

- Removing events coming through the back of the detector. This removal is meant to separate the cosmic events from the signal events at the back of the detector, where there is less shielding.

BDT for the NC disappearance analysis

The majority of the background cosmic events that pass through the selection process discussed above are removed using BDT. The TMVA network is trained by inputting variables with distinct features for NC signal and cosmogenic background. For both FHC and RHC analysis, the input variables to the TMVA network are mainly ShowerLID[3] CAF variables (which describe many distinct properties of a cluster of cellhits reconstructed as a shower in a sliced event), slice variables and cosmic CVN[4]. The BDT is separately trained for the four different samples of the dataset[5], and the

[3]The event shower reconstruction algorithm used in NOvA

[4]Convolutional neural network-based probability score of an event to be a cosmic event

[5]Based on different data taking conditions, data set is divided into 4 samples. Details can be found in Ref. [108]

weight files are saved so that it can be used on the fly in the analysis. Figs. 4.5– 4.9 show the distribution of the 13 discriminating variables (plus two variables whose combinations is used as a discriminating variable) that are used to train the BDT to separate NC signal events from cosmogenic background events. In each row, of these area normalized plots, the left plot is for FHC and the right plot is for RHC. The FD variable plots are applied with complete NC selection cuts (see Ch. 5).

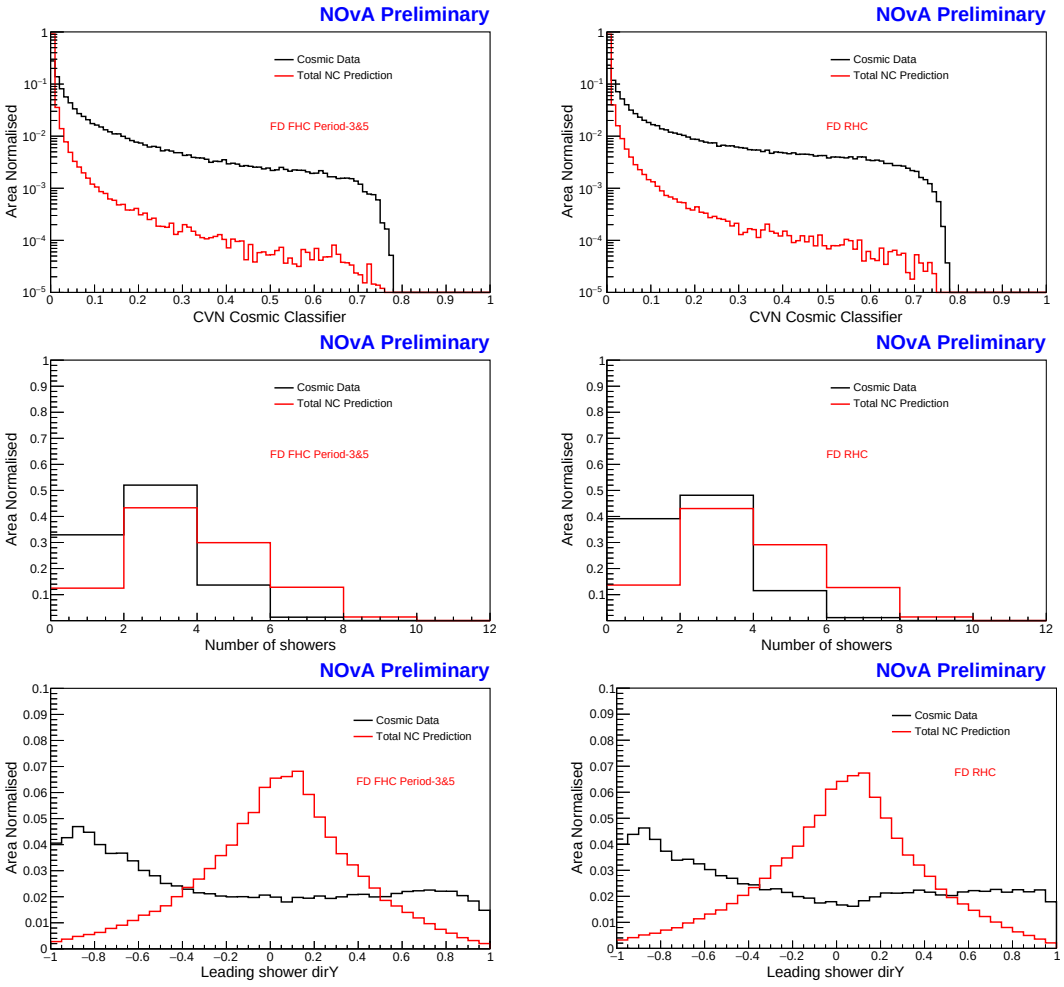

Figure 4.5: BDT input variables. With RHC (right) and FHC (left).

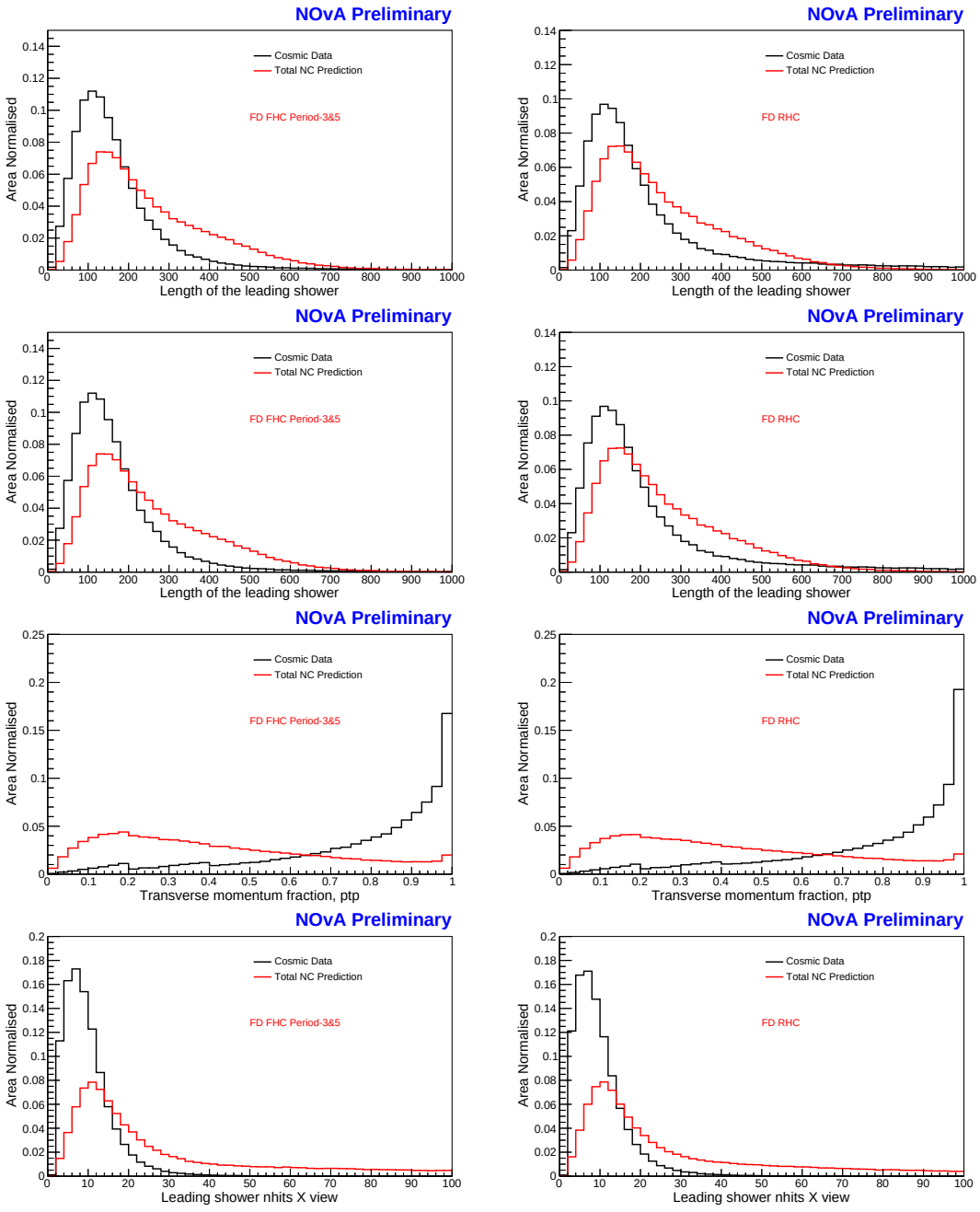

Figure 4.6: BDT input variables. With RHC (right) and FHC (left).

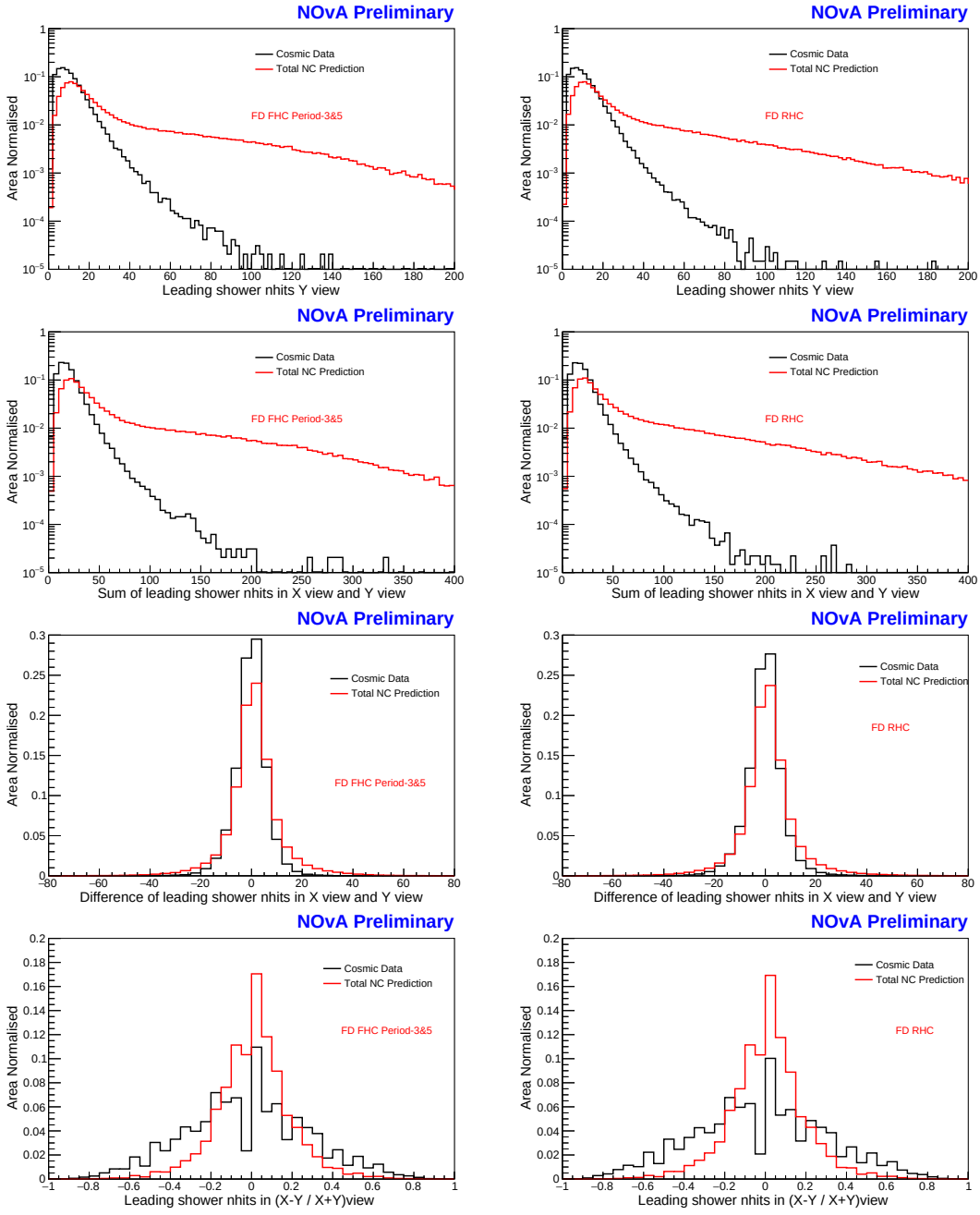

Figure 4.7: BDT input variables. With RHC (right) and FHC (left).

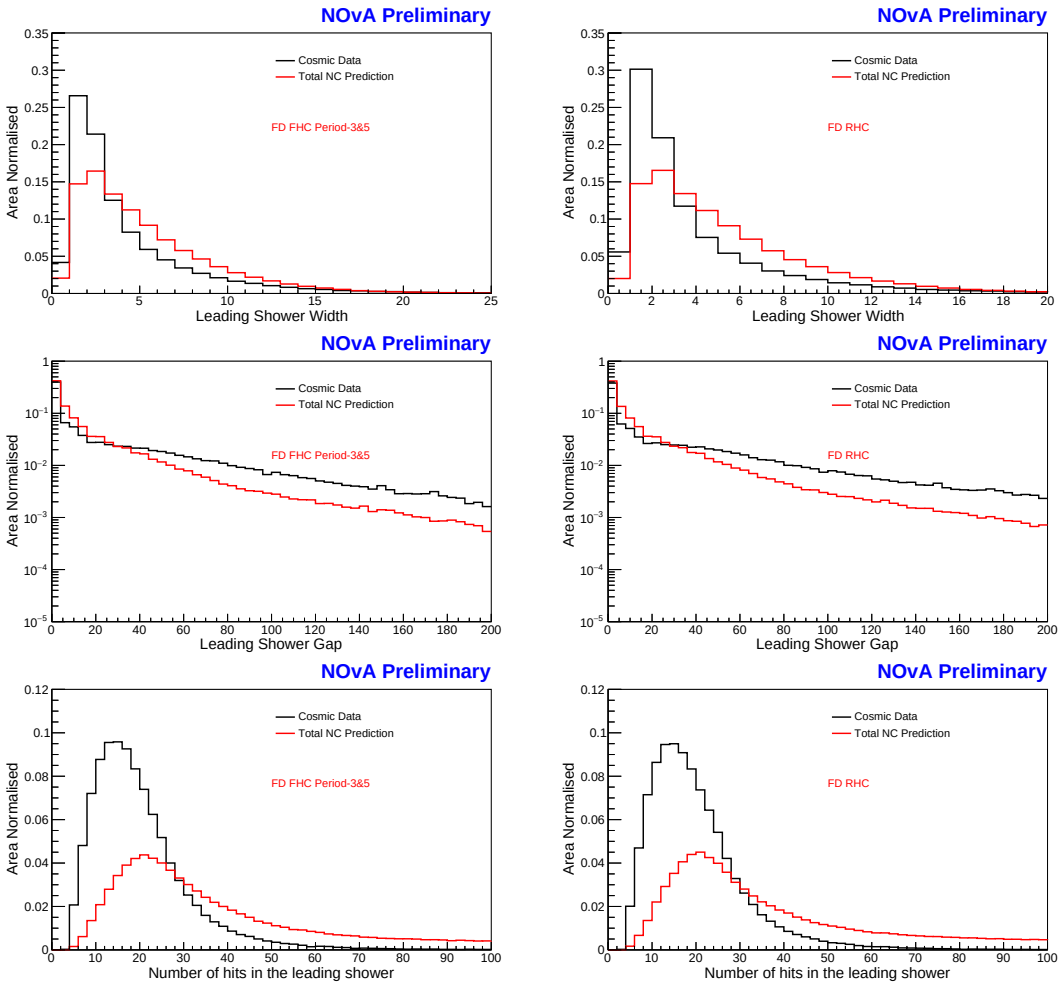

Figure 4.8: BDT input variables. With RHC (right) and FHC (left).

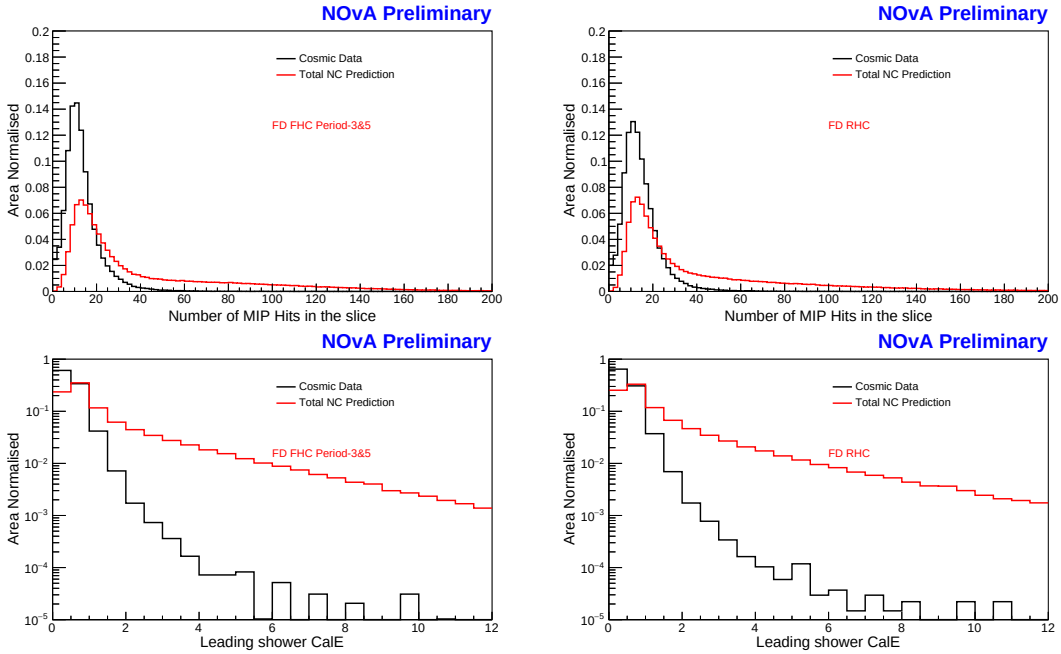

Figure 4.9: BDT input variables. With RHC (right) and FHC (left)

Training and Producing the Weight Files

The TMVA is trained using a subset of the dataset of both MC files and cosmic data files (using 1/3 of the total dataset). Using a CAFAna macro, a ROOT tree is produced with leaves that correspond to the variables used for the training. The tree should contain two branches, one corresponding to the NC signal events which extracted from the MC dataset (used truth condition to get the true NC events), the other branch is made from the cosmic data file and corresponding to the cosmic events. For getting the most NC like cosmic events that pass all NC selection criteria, the tree is filled with events that pass through the following conditions:

- Cosmic veto to remove obvious cosmics.
- Event quality cut which removes fuzzy events and the issues due to FEB flashes.
- Containment cut, which makes sure that the event is fully contained in the detector.

- Fiducial cut helps to select only well-reconstructed events.
- Selects events with a number of hits > 25 and classic CVN NC score > 0.2.
- Cosmic rejection cuts are explained in Sec. 4.2.1.

Details of the NC selection procedure is summarized in Ch. 5. The training event energy is not restricted in any particular region of the spectrum. As a second step, the TMVA network is trained using a training macro with a ROOT tree which has separated NC and cosmic background events. The output of this training is weight files. Different aspects of the training and properties of the separating variables (covariance, overtraining check, etc.) are done using a testing macro.

4.2.2 Evaluating the BDT Performance

The ND data/MC comparison for the trained BDT variables is the best way to investigate for the mismodeling. The following two pages comprise of the distribution of the BDT variables at the FD, with cosmic data and MC (refer Figs. 4.10 and 4.11). The ND data/MC comparison for the BDT variables are shown in Fig.4.13.

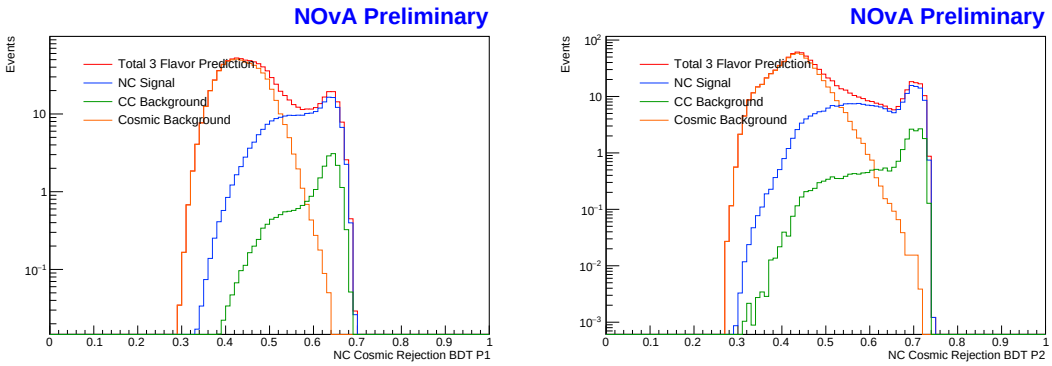

Figure 4.10: The BDT input variable at the FD for the period-1 (left) and period-2 (right). These plots are N-1 plots: applied all NC FD selection cuts except cosmic rejection BDT.

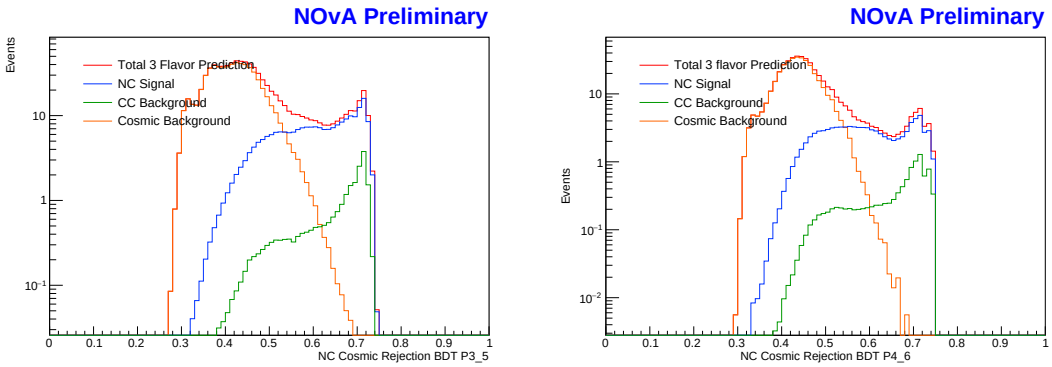

Figure 4.11: The BDT input variable at the FD for the period-3&5 (left) and period 4&6 (right). These plots are N-1 plots: applied all NC FD selection cuts except cosmic rejection BDT.

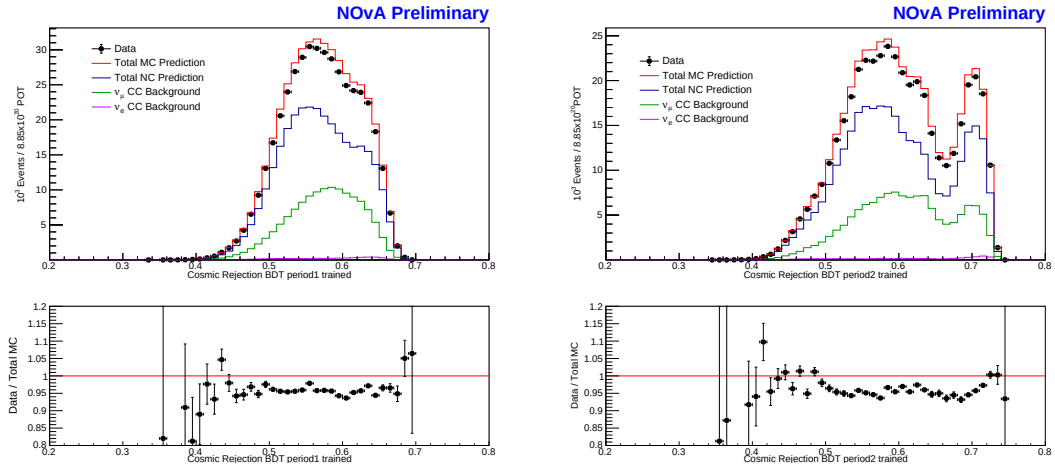

Figure 4.12: Comparison of data/MC for the BDT input variable at the ND for period-1 sample (left) and period-2 sample (right).

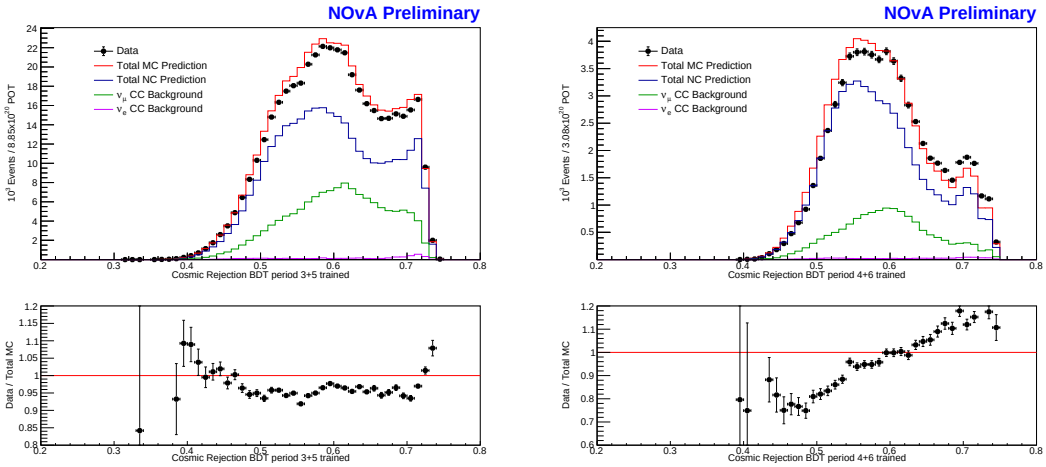

Figure 4.13: ND data/MC comparison for the BDT input variables for the period-3&5 (left) and period 4&6 (right). These events are passed through all ND NC analysis selection cuts. The data/MC discrepancy in the RHC BDT distribution (right plot) can be explained as poor modeling of its training variables.

After this cross-check, four different sets of BDT weights each correspond to one training dataset are saved. When a particular dataset is subject to the analysis, the BDT corresponds to that dataset is called based on its run number.

4.3 Cosmic π^0 Mass Reconstruction in the NOvA Far Detector

4.3.1 Absolute Calibration

The absolute calibration is the final step of the calibration chain. Absolute calibration provides a conversion factor between the detector response and the true energy deposited in the scintillator. The aim of the absolute calibration is to express energy deposits in physically meaningful units (GeV). There exist a few standard candles which can be used as a tool for absolute calibration. The primary tool used in NOvA detectors is the stopping muons in both detectors (discussed in Sec. 3.1.2). Some other standard candles include:

- Michel electron spectrum.
- π^0 invariant mass.

Fig. 4.14 shows the reconstructed mass peak at the ND using the beam π^0.

4.3.2 Introducing the Cosmic π^0 Mass Reconstruction in NOvA

A completely different methodology is adopted to reconstruct the π^0 mass in the FD. The main challenge is the scarcity of beam π^0's in the FD. So we have to look for some other source. The feasible candidate is the π^0 events from the cosmic rays. But as far as NOvA FD is concerned, we have to tackle many problems to realize this. Some of them are:

- The π^0 events in the NOvA FD are rare.
- Most of the cosmic π^0 events in the detector are low energy events with an average of 5-8 hits in each prong.
- Since the NOvA FD is situated at the ground surface, it is subject to a huge influx of cosmic rays with a frequency of 150 kHz.
- Since the cosmic influx to the detector is more or less isotropic, the events do not have any directional dependence.

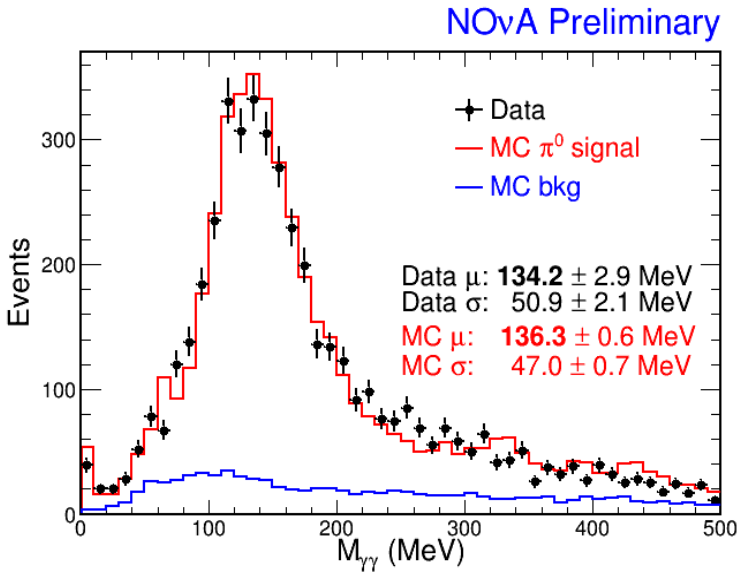

Figure 4.14: The π^0 mass peak used to cross-check the absolute calibration in the ND, using beam π^0s.

- The selection is against a large set of backgrounds.

The predominant decay mode of the π^0 is the two photon decay (branching ratio 0.989). We are going to look for such an event. The theoretical value of the invariant π^0 mass is 134.98 MeV [36].

In the NOvA detector, the π^0 events are identified with two-photon shower like clusters ("Prongs" in the NOvA terminology) with a small gap between the event vertex and the first hit of a prong. The reconstructed π^0 mass is calculated using the formula:

$$M_{\pi^0} = \sqrt{E_{\gamma_1} E_{\gamma_2} (1 - \cos 2\theta)}. \tag{4.1}$$

The E_{γ_1} is the reconstructed energy of the first prong (The most energetic prong). E_{γ_2} is the reconstructed energy of the second prong and 2θ is the opening angle between the two prongs. An example event is shown in Fig. 4.15

4.3.3 Event Selection

The event selection process is a two-layer process. As a primary selection strategy, a series of cuts are developed on the basic event variables such as:

- The number of hits in each prong.
- The opening angle between the two prongs.
- The gap between the event vertex and the first hit of each prong.

The details of the cut are tabulated in Table. 4.1. On top of this, a different variant of CVN is used to identify the extent of photon contribution in each of the prong.

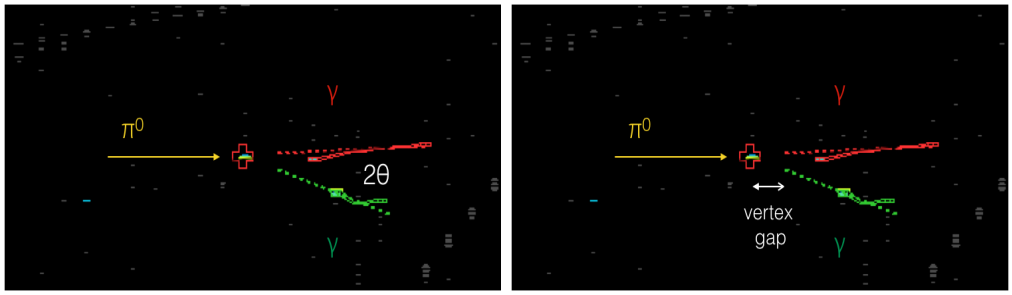

Figure 4.15: The left plot is a display of π^0 event showing the opening angle between two prongs(2θ). The right plot shows the gap between the event vertex and the first hit of each prong. There are two gaps per event: the gap between vertex and first hit of most energetic prong(known as "Gap1"), and the gap between event vertex and second prong ("Gap2").

The Event Selection Using Convolutional Visual Network

The CVN [102] takes the calibrated hits as input. Each event in the NOvA detector can be interpreted as two 2D images, one in each view (X-view and Y-view). A multi-layered representation of each image is constructed using the features extracted from the image using a convolutional neural network deep learning technique. Bypassing these features through a single hidden layer traditional neural network to get likely flavor of neutrino and the interaction type as output. This kind of CNN is known as event CVN, which we have discussed earlier in Sec. 4.1.

For this analysis, an adaptation of the CVN known as prong CVN is implemented. The prong CVN is trained with the individual component of an event. Generally speaking, the output of this adaptation of CVN would be the likelihood score of different particles for a particular component of an event, such as prong, shower, etc. This version of the prong CVN makes use of the slice information along with the prong information. The photon contribution (γ-CVN in Table. 4.1) in both of the prongs are used along with the muon score (μ-CVN in Table. 4.1).

Cosmic π^0 Signal

The π^0 events that decay to two-photon shower is our signal in this analysis. A condition is implemented to confine the event vertex inside the fiducial volume of the detector. Most of the events are coming from cosmic neutrons and protons. Some rare cases of charge exchange interaction of π^- are also seen. The event display of a typical signal event is shown in Fig. 4.16

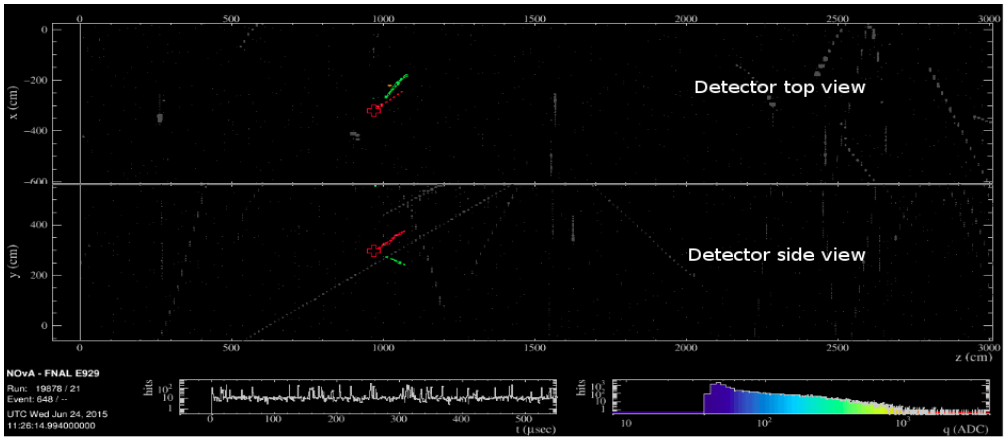

Figure 4.16: An event display of the signal event.

Backgrounds

Due to the high influx of cosmic rays to the NOvA FD, there are a lot of background events having topology identical to that of π^0 signal. The major part of the backgrounds are photons with parents other than π^0. They fall mostly into 2 categories:

- Nuclear de-excitation caused by protons and neutrons of the cosmic origin.
- Some cases of Bremsstrahlung shower are also identified.

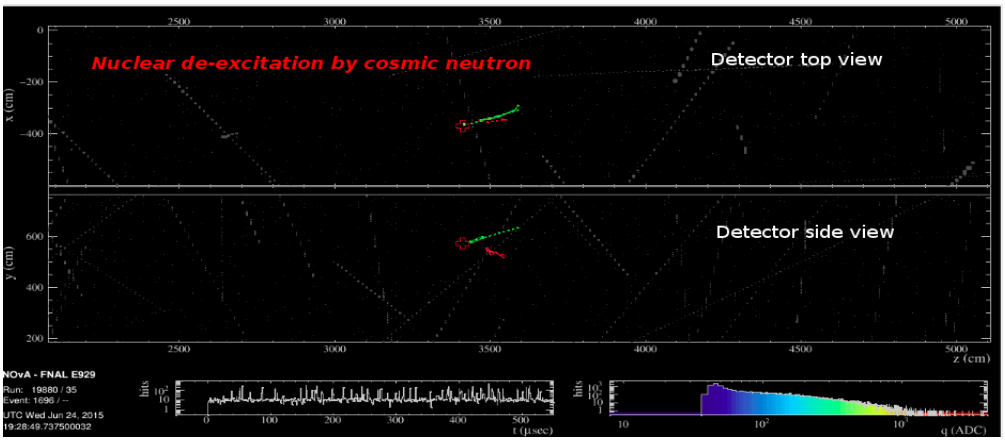

Figure 4.17: An event display of the background event. The nuclear de-excitation caused by the cosmic neutron is responsible for the event.

Signal - Background Distribution.

The selection cuts are tuned by hand using signal and background distributions. The variables are correlated very tightly, which makes the separation of signal from background cumbersome. Figs. 4.18 and 4.19 are the signal and background distributions. The cuts developed by this procedure are summarized in Table. 4.1. The BDT multivariate technique was also implemented [99] in the sample to improve the selection of signals from the background. But the MC statistics at the region of our interest limits the power of the TMVA technique. Fig. 4.20 explains these points.

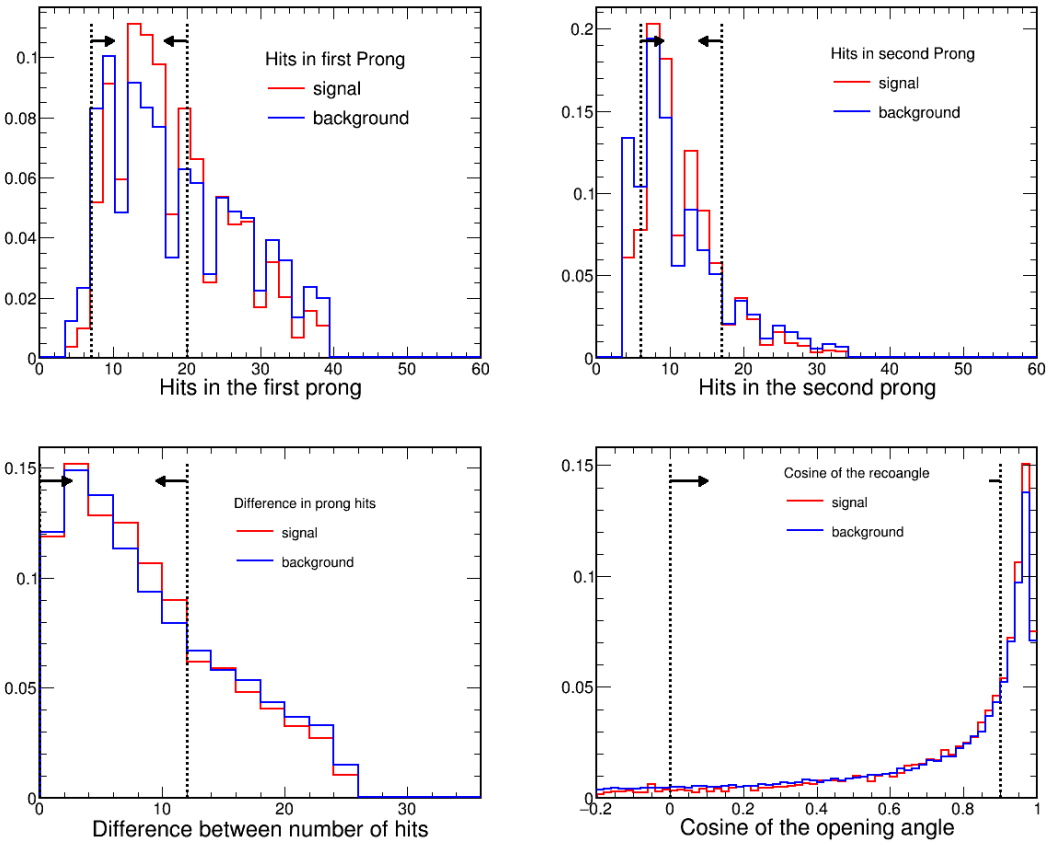

Figure 4.18: The signal vs background plots for the different selection variables used for this analysis.

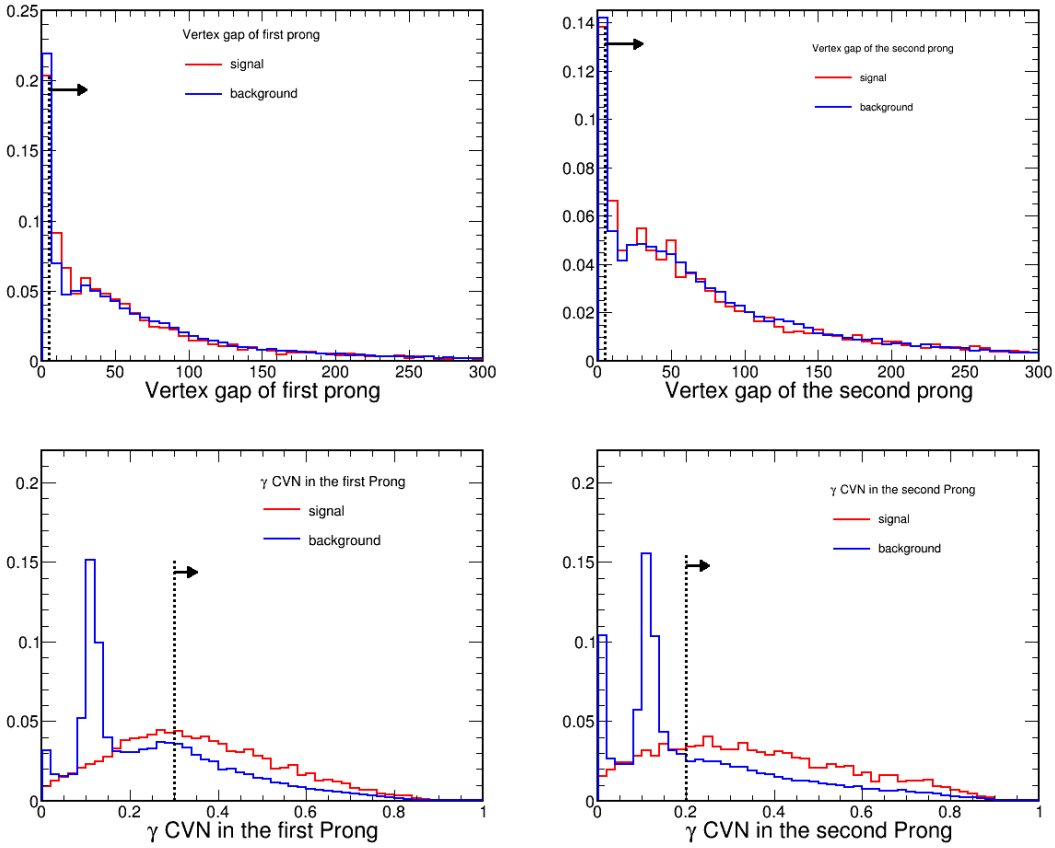

Figure 4.19: The signal vs background plots for the different selection variables used for this analysis. The first prong means the most energetic one among the two. These plots are area normalized.

Prong variable	Lower value	Upper value
Opening angle	26^0	90^0
Prong1 hits	7	20
Prong2 hits	6	17
Prong1 hits − Prong2 hits	0	12
γ_1-cvn	0.5	1
γ_2-cvn	0.2	1
μ_1-cvn	0	0.025
μ_2-cvn	0	0.015
Gap1	5 cm	-
Gap2	5 cm	-
Number of missing planes	> 0	-
Number of most contiguous	> 0	-

Table 4.1: Summary of the selection cuts used for the π^0 mass reconstruction analysis.

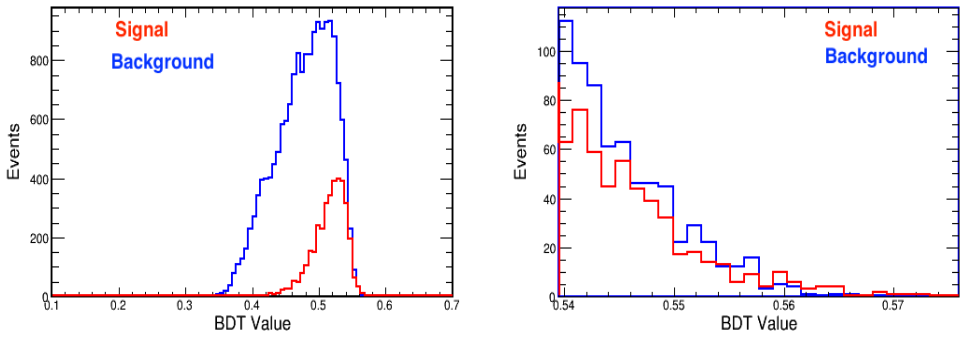

Figure 4.20: The left plot is the BDT distribution and the right plot is the zoomed version of the left plot which shows the region where signal dominates over background. Red line is the signal and blue line is the background.

The Data/MC Comparison

The cosmic MC and data are compared after applying the selection cuts developed. Fig. 4.21 shows the data/MC comparison of the basic variables after applying the preselection cuts, ie. the primary level selection cuts that does not include a CVN cut.

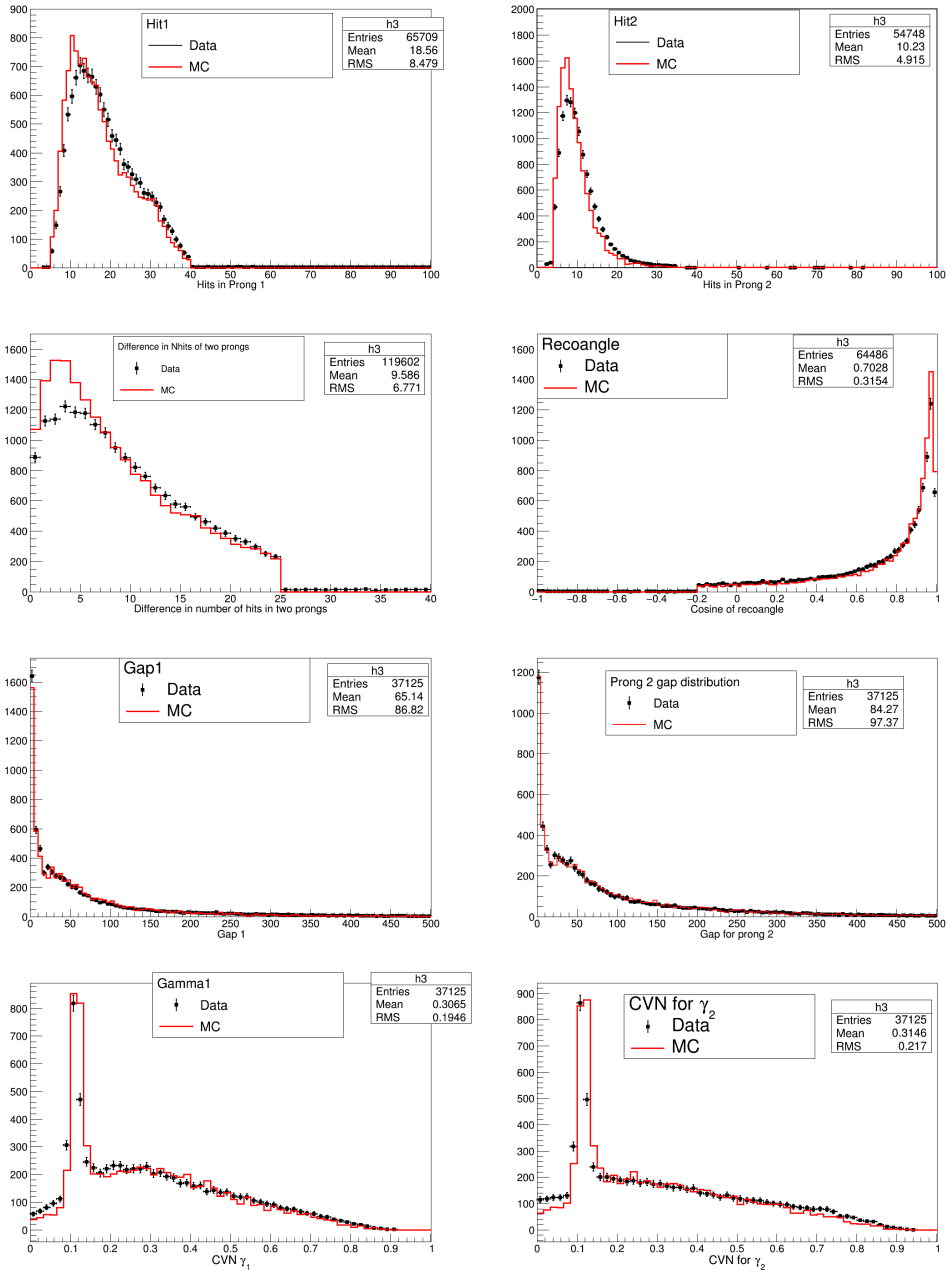

Figure 4.21: The data vs MC plots for the different variables used for the event selection. The plots are with applied preselection cuts

4.3.4 Reconstructed Mass Peak

After applying all selection criteria that have been summarized in Table 4.1, the reconstructed π^0 mass peak is plotted with data and MC. Total 2030 π^0 candidates are selected in the data. The selection has an efficiency of 15 % and a purity of 55%.

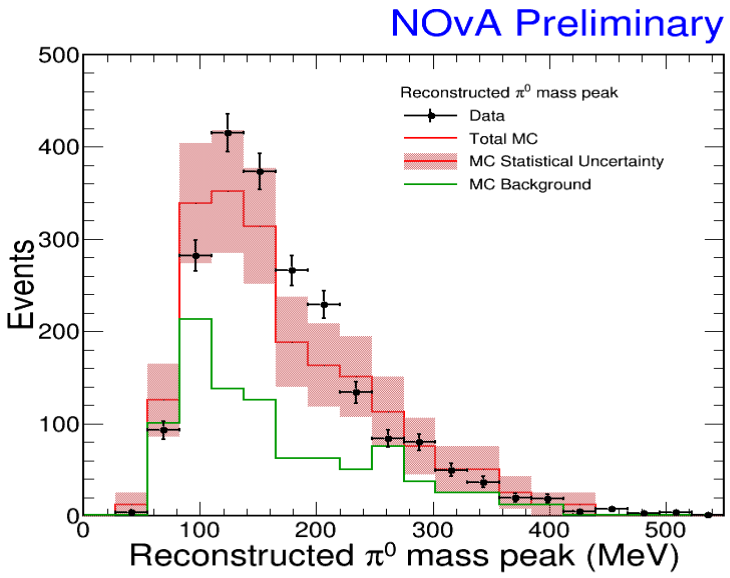

Figure 4.22: The reconstructed cosmic π^0 mass peak.

In Fig. 4.22, the MC simulation is normalized to the detector lifetime of data. The simulation sample is 1/12th the size of the data sample. The uncertainty is dominated by simulation statistics. This is one of the rare cases, in which the production of simulation statistics is too expensive to match up with the measured data statistics. The variables of Gaussian fit to the mass peak is tabulated in the table below.

Sample	Mean	σ
MC	118.3 ± 17.1	53.3± 20.8
data	135.1 ± 2	45.6 ± 3.4

Table 4.2: The table shows the Gaussian fit values for the data and MC. The data peak at 135 MeV. But due to low MC statistics, the statistical uncertainty is very large.

The Gaussian fit to the mass peak gives the information that the data and MC agree within 0.9σ.

4.3.5 Summary

A new method is introduced to identify cosmic π^0 in the NOvA FD to cross-check the absolute calibration. It complements an existing strategy to identify π^0 from the neutrino beam using more traditional methods in the ND.

5

Event Selection for the NC Disappearance Analysis

5.1 2017 FHC Analysis

5.1.1 Introduction

In this analysis, the observed FD spectrum of NC selected events are compared with the FD predicted spectrum after extrapolation. Selecting a pure sample of NC signal events are essential for it. The ν_μ CC interactions, ν_e CC interactions, and cosmic ray events that mimic NC event topology are the major backgrounds for this analysis. There is a negligible amount of ν_τ CC background. This chapter describes the step by step process for selecting a pure sample of NC events and reducing its backgrounds, discussing data quality selection, event quality selection, fiducial cut, containment cut, and NC selection. The particle identifying algorithms such as CVN and BDT (discussed in Secs. 4.1 and 4.2) are implemented to select a desirably pure sample of signal NC events. The MC beam spectra are scaled to 8.85×10^{20} POT and the cosmic data is scaled to the equivalent lifetime of 440 s. Cuts were set assuming the three-flavor oscillation parameters listed in Table 5.1.

Oscillation Parameter	Value
ρ	2.8 g/cm^3
Δm^2_{21}	7.53 $\times 10^{-5}$eV^2
$\sin^2 2\theta_{12}$	0.846
Δm^2_{32}	2.44 $\times 10^{-3}$eV^2
θ_{23}	$\pi/4$
$\sin^2 2\theta_{13}$	0.085
δ_{CP}	0

Table 5.1: The three-flavor oscillation parameters used for the NC selection in 2017 FHC analysis. Same as that used in Ref. [105].

The cuts discussed in this chapter were trained on cosmic data from the cosmic trigger.

5.1.2 Data Quality

Data quality (DQ) cuts helps us to ensure proper data taking conditions. This selection is treated as standard and all NOvA analyses use them. These cuts are applied per spill, and spills that fail these cuts are not included in POT accounting. The cuts can be categorized into three main groups: beam quality, data quality, and timing. The beam quality cuts are studied and set as described in Ref. [109]. A beam spill must pass the condition listed in Table 5.2 to qualify for the analysis. Two data quality cuts are applied to data and MC for each detector. These cuts are motivated and set as described in Refs. [110–112], and are summarized in Table 5.3. There is also a run filter applied to filter out runs identified as bad and kept in a list (kRunsFilter) as well as a cut to remove any spills that do not have any continuous segments larger than four diblocks (kRemoveSmallMasks). These cuts are all captured by kStandardSpillCuts. Finally, a timing cut is applied to cosmic data, kInCosmicTimingWindow, to ensure that the data is not too close to the edge of the data taking window. For cosmic events within a given 500 μs trigger window, only events between 25 μs $<$ t $<$ 475 μs are kept. Table 5.16 shows the number of events that pass these data quality cuts.

Beam Quality Parameter	Minimum	Maximum
Spill POT	2.00 $\times 10^{12}$	-
Horn Current	-202 kA	-198 kA
Beam X and Y position on target	0.02 mm	2.00 mm
Beam X and Y width	0.57 mm	1.58 mm
Time to nearest beam spill		0.5 μs

Table 5.2: Beam quality cuts applied to each spill to ensure proper data taking conditions.

Data Quality Parameter	Detector	Metric for Spill to Pass
Number of Missing DCMs	ND	=0
Hit Fraction	ND	$\leq$0.45
Missing DCMs from LiveGeometry	FD	=0
DCM Edge Match Fraction	FD	>0.2

Table 5.3: Data quality cuts applied to each spill to ensure proper data taking conditions.

Cut Level	NC	ν_μ CC	ν_e CC	ν_τ CC	cosmic
DQ at FD	405.74	824.486	103.731	8.33952	936.556
DQ at ND (X10^3)	6469	36843	596.1	0	0

Table 5.4: The number of events that pass the data quality cuts, at both detectors.

5.1.3 Event Quality

Event quality (EQ) cuts are applied after reconstructing neutrino events. They ensure that the events are well reconstructed without any probable failure and they have enough information to be properly analyzed. As with the data quality cuts above, these cuts evolved from the summer 2016 NC disappearance analysis [105]. Two of the cuts within this suite require the presence of at least a reconstructed vertex and a reconstructed prong object in an event. These reconstructed objects are used more extensively at later stages, so that the event quality cuts make sure that they are available. Other quantities considered are the number of hits per plane and the number of contiguous planes. Events with a high number of hits

per plane are cut to remove so called "FEB Flashers", ie. an electronics failure most often triggered by high energy cosmic rays. Likewise, events with a low number of contiguous planes are most often associated with very vertical cosmic rays. These cuts are summarized, with the exact cut values used, in Table 5.5. The number of events before and after the kNus17EventQuality cuts are listed in Table 5.8 and Fig. 5.1 shows the energy spectra of the events that pass these cuts.

Event Quality Parameter	Condition an for event to pass
Number of reconstructed vertex objects	>0
Number of reconstructed prong objects	>0
Number of hits per plane	<8
Number of contiguous planes	>2
Number of hits (FD)	> 20
Number of hits (FD)	< 250
Number of hits (ND)	> 10
Length of longest prong (ND & FD)	<500 cm

Table 5.5: EQ cuts applied to individual events.

Cut Level	NC	ν_μ CC	ν_e CC	ν_τ CC	cosmic
DQ at FD	405.74	824.486	103.731	8.33952	936.556
+ EQ at FD	373.376	809.057	102.379	8.16352	919.6
DQ at ND ($\times 10^3$)	6469	36843	596.1	0	0
+EQ at ND ($\times 10^3$)	6420	36801	595.3	0	0

Table 5.6: The number of events before and after application of event quality cuts, at both detectors.

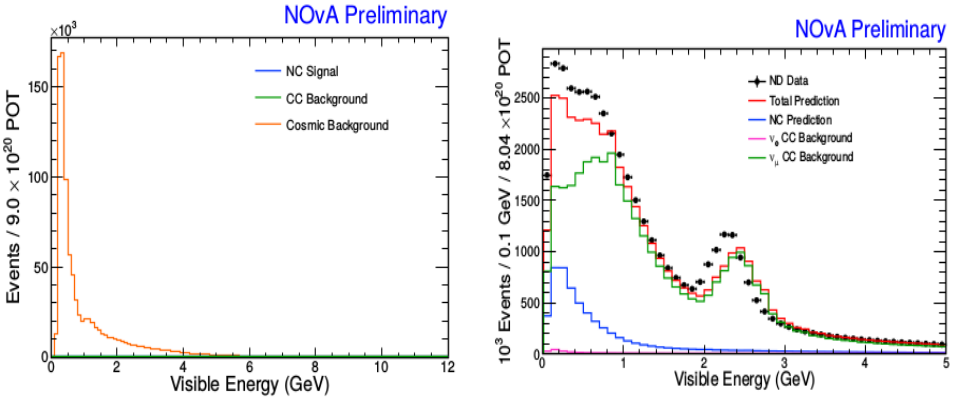

Figure 5.1: Event distribution in the FD (left) and ND (right) after applying EQ cut.

5.1.4 Fiducial Volume and Containment

Fiducial volume (ND-only) and containment cuts are designed to eliminate the events originating outside of the detector. At the same time it ensure that event interactions originating inside the detector have its complete activity inside the active region of the detector. The fiducial volume cut is on the location of the reconstructed neutrino vertex. The containment cut considers the distance of all prongs in a slice from the Top, Bottom, Front, Back, East and West edges of the detector. For each detector face, cuts are applied on the minimum distance of the start or stop point from the edge in question, after considering all prongs. The specific cuts are set separately for each detector and are listed in Table 5.7 and Table 5.9.

Far Detector

Event reconstructed variables	Condition
Min. dist. from all prong start/stop dist. to detector Top	>100 cm
Min. dist. from all prong start/stop dist. to detector Bottom	>10 cm
Min. dist. from all prong start/stop dist. to detector East	>50 cm
Min. dist. from all prong start/stop dist. to detector West	>50 cm
Min. dist. from all prong start/stop dist. to detector Front	>50 cm
Min. dist. from all prong start/stop dist. to detector Back	>50 cm

Table 5.7: Conditions to be satisfied by an event, to pass the containment cut at the FD.

Cut Level	NC	ν_μ CC	ν_e CC	ν_τ CC	cosmic
DQ + EQ	373.376	809.06	102.38	8.16	919.6
DQ + EQ + Containment	256.53	249.03	69.46	4.80	5493.46

Table 5.8: The number of events before and after the application of the containment cut at the FD.

Near Detector

The ND is in a "safe depth" from the ground level; as a result of that, there will not be much cosmic background to eliminate. At the same time, there are many events that originate with the neutrino interaction in the rock outside of the detector that can leak into the detector. This happens because the ND is placed in a cavity surrounded by rock. Furthermore, due to the small size of the ND, many events have exit out the detector. The fiducial and containment cuts at the ND are engineered to reduce both of these problems. The fiducial cuts on the X and Y coordinates of the reconstructed vertex were applied symmetrically, with a modestly large cut to remove events that originate in the rock outside the detector. The vertex cut on Z filters a large portion of the detector to remove rock events that leak into the front of the detector. In the same fashion as for the FD, the containment cut on the ND considers the distance of all prongs in a slice from the Top, Bottom, Front, Back, East and West edges of the detector. For each detector face, cuts are applied to require the minimum distance of the start or stop point from the edge in question to be greater than 25 cm symmetrically for each edge, after considering all prongs. All of these cuts are summarized in Table 5.9.

Event reconstructed variables	Condition
X coordinate of the reco vertex	-100 cm $\leq$ vtxX $\leq$ 100 cm
Y coordinate of the reco vertex	-100 cm $\leq$ vtxY $\leq$ 100 cm
Z coordinate of the reco vertex	150 cm $\leq$ vtxZ $\leq$ 1000 cm
Min. dist. from all prong start/stop dist. to detector Top	$>$ 25 cm
Min. dist. from all prong start/stop dist. to detector Bottom	$>$ 25 cm
Min. dist. from all prong start/stop dist. to detector East	$>$ 25 cm
Min. dist. from all prong start/stop dist. to detector West	$>$ 25 cm
Min. dist. from all prong start/stop dist. to detector Front	$>$ 25 cm
Min. dist. from all prong start/stop dist. to detector Back	$>$ 25 cm

Table 5.9: Condition to be satisfied by an event, to pass the containment cut at the ND.

Cut Level	NC	ν_μ CC	ν_e CC
DQ + EQ	6420	36801	595.3
+ Fiducial	1090	4239	95.5
+ Containment	606.5	820.2	36.71

Table 5.10: The number of events before and after applying fiducial and containment cuts at the ND. Here, containment refers to cuts on the minimum distance prong start/stop points, when considering all prongs, to each detector face. All numbers in this table should be multiplied with 10^3.

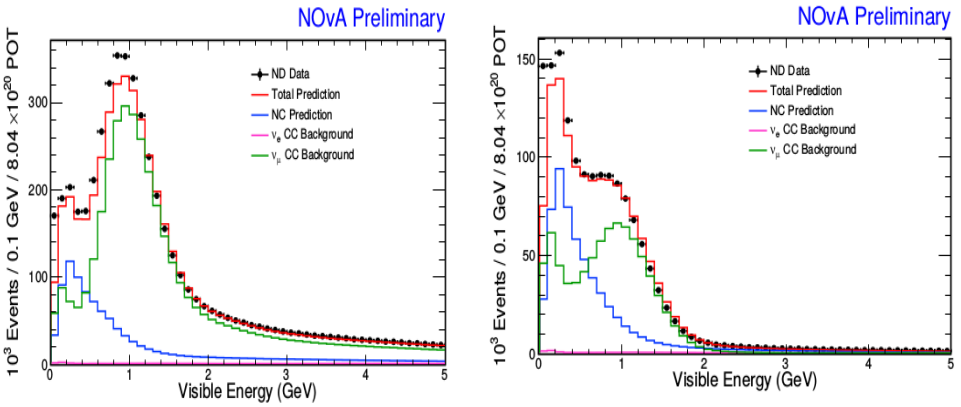

Figure 5.2: Energy spectra after fiducial and containment cuts for the ND. On the left, the cuts applied are data quality, event quality, and fiducial. The right plot have an additional containment cut.

5.1.5 Cosmic Rejection

Since the FD is located on the surface, it is exposed to 150 kHz of secondary cosmic rays. The cosmogenic neutrons produced in the FD overburden pass into the detector and have the potential to fake the neutrino event. On the average, before applying additional selections, we reconstructed 74,000 cosmogenic events for each reconstructed neutrino event in the 10 μs beam spill window.

The first step in cosmic rejection is to remove the cosmic photons entering the detector from the back, where the overburden is thin. We employ the Backward Photon Cut (kNus17BackwardCut) devised by the ν_e analysis group (Ref. [107]). Electromagnetic showers due to electrons begin with minimum ionizing hits, broaden in the middle and become sparse towards the end of the shower; a completely reversed profile is observed for the backward photon showers. A sparseness asymmetry[1] that used to separate ν_e CC events in the back of the detector from the backward photon is implemented in this analysis. Specifically for this analysis, a new NC dedicated cosmic rejection BDT algorithm has been implemented. The

[1]It is defined as the difference divided by sum of planes without any hits in the first 8 and the last 8 planes of showers

details can be found in Ch. 4. We try to separate the remaining cosmic background events with further two cuts: one based on nearest slice information and a second carving out a space in the transverse momentum versus shower maximum position in the detector Y coordinate. These cuts are adapted from the NOvA ν_e analysis selection. Since the ND is at 100 m underground, only a negligible amount of cosmic energy deposition at the ND. Almost all fail to pass the other NC selection criteria. So, no cosmic rejection BDT cut is implemented for the ND. At the FD, events with BDT score greater than 0.62 are selected for the analysis.

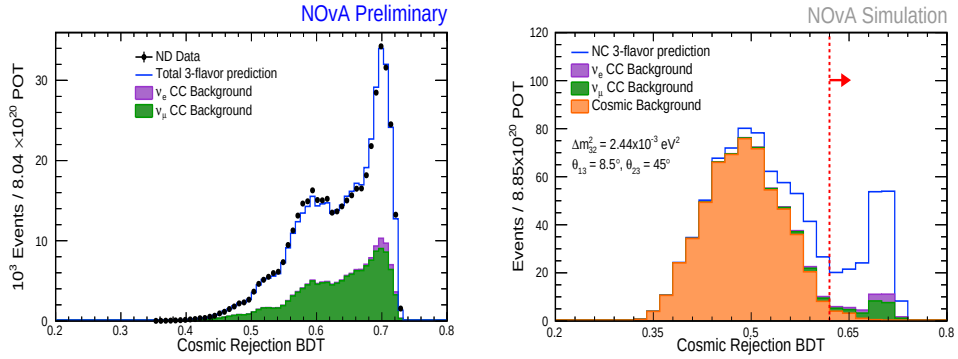

Figure 5.3: Stack plots of the cosmic rejection BDT variable distribution. The left plot is for the ND and the right plot is for the FD. The FD plot is normalized with the data POT of 8.85×10^{20}. ND plot is normalized with a data POT of 8.05×10^{20}.

Cut Level	NC	ν_μ CC	ν_e CC	ν_τ CC	Cosmic
.. + Containment	256.53	249.025	69.4641	4.79875	5493.46
+ Cosmic rejection	142.926	20.8015	9.45697	2.82166	23.5858

Table 5.11: The number of events before and after application of cosmic rejection cuts at the FD.

5.1.6 NC Selection

The primary purpose of the NC selection cut is to separate the NC signal from the CC backgrounds. For this purpose, we employ the CVN NC

identifier, CVNnc, which is discussed in more detail in Ch. 4. On top of the CVN NC selection cut, we put a condition on the number of hits in the selected event should be greater than (or equal to) 25 and set a 0.25 GeV lower threshold on the calorimetric energy for both detectors. The number of hits and calorimetric energy cuts is designed to cut off the very low-efficiency region where threshold effects are present. The cut on CVNnc remained the same as for that used in the summer 2016 analysis [105], i.e events with CVNnc score greater than 0.2 are selected. A cut on the transverse momentum fraction is applied in the ND to remove rock events. Before applying this cut the CVN distribution has a 10% data excess over MC. Table 5.12 summarizes the cuts used and Fig. 5.4 shows the energy distributions of events that pass these cuts.

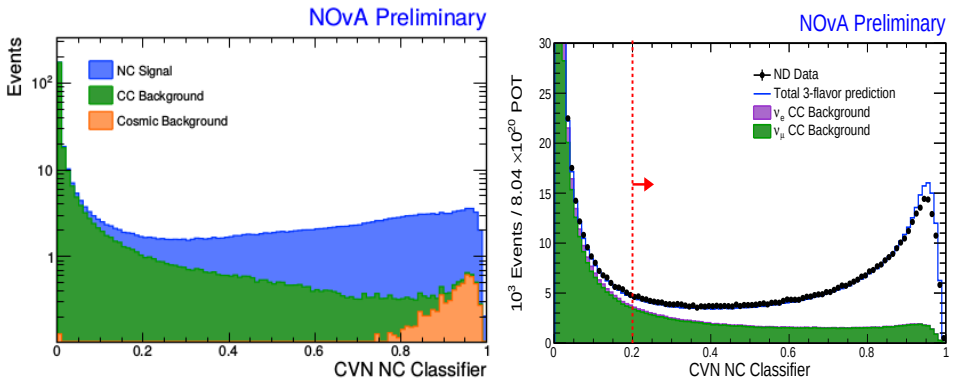

Figure 5.4: Stack plots of CVN NC Identifier distribution after applying all selection cuts except on CVN, for the ND(right) and FD(left).

Parameter used for selection	Cut
CVN NC Identifier value	≥ 0.2
Number of Hits	≥ 25
Energy Deposited	>0.25 GeV
p_T/p (ND-only)	≤ 0.8

Table 5.12: NC selection cuts to reject CC events, leaving a relatively pure sample of NC events. Since the BDT applied at the FD remove high p_T/p events, there is no need to apply a p_T/p cut at the FD.

Cut Level	NC	ν_μ CC	ν_e CC	Total MC	ND data
Data Quality	6469	36843	596.1	43909	46974
+ Event Quality	6420	36801	595.3	43816	46858
+ Fiducial	1090	4239	95.5	5425	5692
+ Containment	606.5	820.2	36.71	463	1567
+ NC selection	306.1	141.7	6.6	454.4	456.8

Table 5.13: The number of events after application of different levels of event selection cuts that we discussed so far, at the ND.

Cut Level	NC	ν_μ CC	ν_e CC	ν_τ CC	Cosmic
Data Quality					
+ Event Quality	373.376	809.057	102.379	8.16352	924220
+ Containment	256.53	249.025	69.4641	4.79875	5493.46
+ Cosmic rejection	142.926	20.8015	9.45697	2.82166	23.5858
+ NC selection	135.796	20.141	9.03707	2.7294	8.42142

Table 5.14: The number of events after application of different levels of event selection cuts that we discussed so far, at the FD.

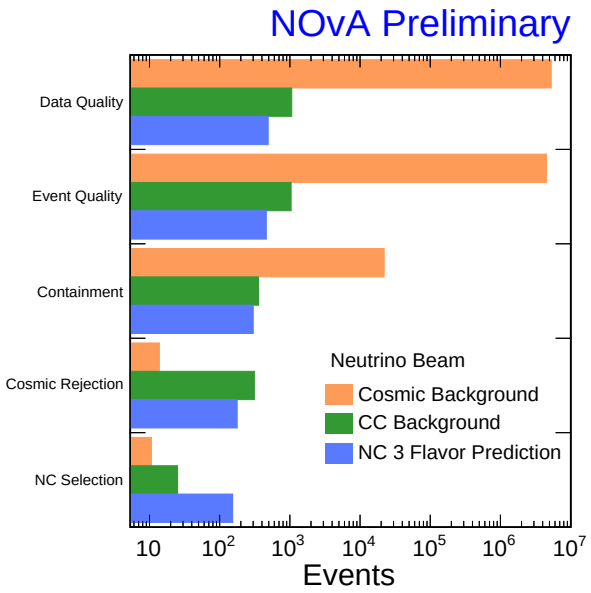

Figure 5.5: This FD plot shows the effect of each cut-level in the neutrino NC disappearance analysis.

After applying all the selection cuts that we have discussed so far, we get a prediction of 148.3 NC signal events and 42.8 background events. Among these backgrounds, 22.2 events are ν_μ CC, 9.9 events are ν_e CC, 2.8 ν_τ CC events and 7.9 cosmics. Here we can see that the dominant background is ν_μ CC.

5.2 RHC 2019 Analysis

5.2.1 Introduction

This analysis has used the same selection cuts as developed for the RHC 2018 analysis. The MC beam spectra are scaled to 7×10^{20} POT and the cosmic data is scaled to the equivalent lifetime of 176 s. Cuts are set assuming the three-flavor oscillation parameters as listed in Table 5.15. The cuts discussed in this chapter are trained on cosmic data and beam MC. These data have passed through a cosmic veto motivated by the ν_e appearance analysis. The actual cosmic prediction will come from the

Cut Level	NC	$\nu\,(\overline{\nu})$	$\nu_\mu\,(\overline{\nu}_\mu)$ CC	$\nu_e\,(\overline{\nu}_e)$ CC	$\nu_\tau\,(\overline{\nu}_\tau)$ CC	cosmic
DQ at FD	142	59.1(82.5)	30.8(14.1)	3.69(3.39)	2.79	321118
DQ at ND ($\times 10^6$)	2.76	1.27(1.49)	9.61(10.6)	0.21(0.14)	0	0

Table 5.16: The number of events that pass the data quality cuts, at both detectors.

NuMI out-of-time sideband. All these are same as the FHC analysis that we have discussed in Sec. 5.1.

Parameter	Value
ρ	2.8 g/cm^3
Δm^2_{21}	7.53x10^{-5}eV^2
Δm^2_{32}	2.44x10^{-3}eV^2
$\sin^2 2\theta_{12}$	0.846
$\sin^2 2\theta_{13}$	0.085
$\sin^2 \theta_{23}$	0.542
δ_{CP}	1.37π

Table 5.15: The three-flavor oscillation parameters used in RHC analysis. We set θ_{23}, δ_{CP} and Δm^2_{32} at PDG [36] normal hierarchy, upper octant values (most conservative).

5.2.2 Data Quality

Data quality cuts (DQ) assure that the proper data taking conditions is common to all other analyses. As we have discussed for the FHC analysis, these cuts are applied per spill, and spills that fail these cuts are not included in POT accounting. Similar to the FHC analysis, these cuts can be categorized into three main groups: beam quality, data quality, and timing.

5.2.3 Event Quality

Event quality (EQ) cuts are applied on the top of the event reconstruction. They ensure that the events are well reconstructed without any probable failure and they have enough information to be properly analyzed. We used the same 2017 FHC analysis strategy. The metric of the reconstructed event variables for passing the event quality cut are

Cut Level	NC	$\nu\,(\overline{\nu})$	$\nu_\mu\,(\overline{\nu}_\mu)$ CC	$\nu_e\,(\overline{\nu}_e)$ CC	$\nu_\tau\,(\overline{\nu}_\tau)$ CC	cosmic
DQ at FD	142	59.1(82.5)	30.8(14.1)	3.69(3.39)	2.79	321118
+EQ at FD	142	59.1(82.5)	30.8(14.1)	3.69(3.39)	2.79	263940
DQ at ND ($\times 10^6$)	2.76	1.27(1.49)	9.61(10.6)	0.21(0.14)	0	0
+EQ at ND ($\times 10^6$)	21.0	0.98(1.16)	8.73(9.88)	0.16(0.11)	0	0

Table 5.17: The number of events that pass the data quality and event quality cuts, at both detectors.

summarized in Table 5.5. The event quality cut variable is termed as kNus19EventQuality. The number of events selected after event quality and data quality cuts are summarized in Table 5.17.

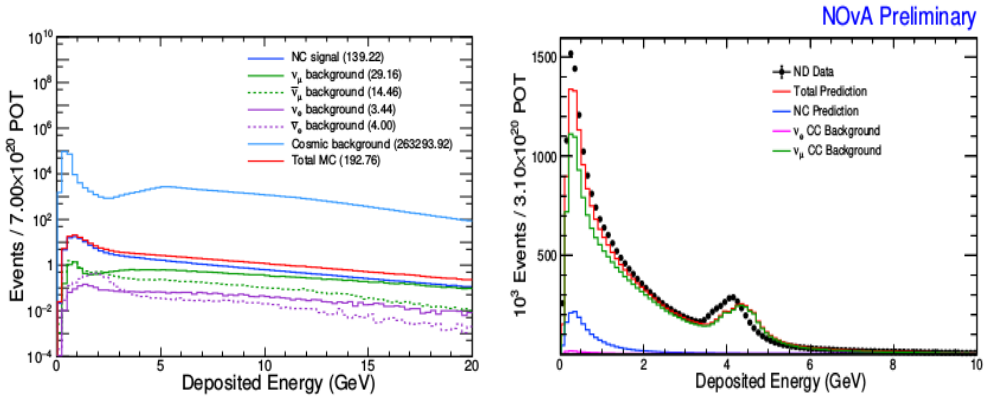

Figure 5.6: Event distribution in the FD (left) and ND (right) after applying EQ cut.

5.2.4 Fiducial Volume and Containment

For fiducial and containment selection, the condition is kept more or less same as that of 2017 FHC analysis. More details can be found in Sec. 5.1.4. The events selected after applying the fiducial and containment cuts at the ND is summarized in Table 5.18 and the number of selected events after applying containment cut at the FD are summarized in the Table 5.19

Cut Level	NC	$\nu\,(\overline{\nu})$	$\nu_\mu\,(\overline{\nu}_\mu)$ CC	$\nu_e\,(\overline{\nu}_e)$ CC
DQ at ND ($\times 10^6$)	2.76	1.27(1.49)	9.61(10.6)	0.21(0.14)
+EQ at ND ($\times 10^6$)	21.0	0.98(1.16)	8.73(9.88)	0.16(0.11)
+Fid+Cont at ND ($\times 10^6$)	0.116	0.0321(0.0835)	0.0343(0.090)	0.00358(0.00447)

Table 5.18: The number of events that pass the data quality, event quality, fiducial and containment cuts at the ND. Here the number of $\nu_\tau\,(\overline{\nu}_\tau)$ CC and cosmic events are turned out to be zero.

Cut Level	NC	$\nu\,(\overline{\nu})$	$\nu_\mu\,(\overline{\nu}_\mu)$ CC	$\nu_e\,(\overline{\nu}_e)$ CC	ν_τ CC	cosmic
DQ at FD	142	59.1(82.5)	30.8(14.1)	3.69(3.39)	2.79	321118
+EQ at FD	142	59.1(82.5)	30.8(14.1)	3.69(3.39)	2.79	263940
+Cont at FD	97.4	37.5(59.9)	9.3(4.1)	2.0(2.0)	1.68	2753

Table 5.19: The number of events that pass the data quality, event quality and containment cuts, at FD.

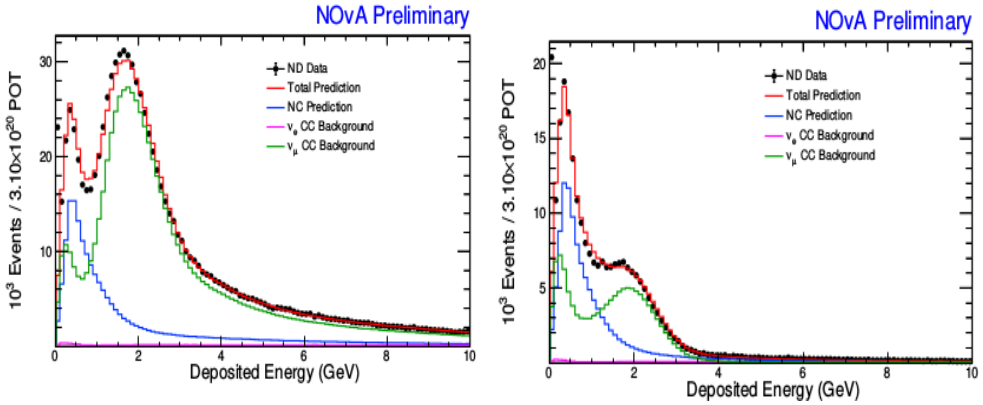

Figure 5.7: Energy spectra for the RHC ND data after the fiducial volume (left) and containment (right) cuts.

5.2.5 Cosmic Rejection

The method to remove cosmic background is similar to the 2017 FHC analysis. We employ the Backward Photon Cut (kNus19BackwardCut) which utilizes the difference in the topology of electromagnetic showers caused by

electrons and that of backward photon showers. A sparseness asymmetry is used to separate ν_e CC events in the back of the detector from the backward photon background and works equally well for removing them from the background to the NC signal. Two additional cuts are employed to carve out the cosmic dominant region of transverse momentum fraction parameter space (kNus19ShowerptpCut and kNus19SlicetimeCut). A cosmic rejection Boosted Decision Tree (BDT) algorithm has been implemented and that is trained using data with different data taking conditions. And trained with RHC data also. The details can be found in Sec. 4.2. The NC BDT response for RHC is taken in such away that the threshold is set at a value 0.55. Events with BDT score greater than 0.55 would pass the selection cut.

Cut Level	NC	$\nu\,(\overline{\nu})$	$\nu_\mu\left(\overline{\nu}_\mu\right)$ CC	$\nu_e\,(\overline{\nu}_e)$ CC	ν_τ CC	cosmic
DQ+EQ	142	59.1(82.5)	30.8(14.1)	3.69(3.39)	2.79	263940
+Cont	97.4	37.5(59.9)	9.3(4.1)	2.0(2.0)	1.68	2753
+Backward	96.1	37.1(59.0)	9.2(4.0)	2.0(2.0)	1.67	2633
+Slc Time	95.7	36.9(58.8)	9.2(4.0)	2.0(2.0)	1.66	2464
+Shw ptp	89.3	34.9(54.5)	8.8(3.8)	1.9(1.9)	1.60	1223
+BDT	51.3	26.1(25.2)	7.1(2.5)	1.7(1.6)	1.47	6.81

Table 5.20: The number of events that pass the cut levels at the FD.

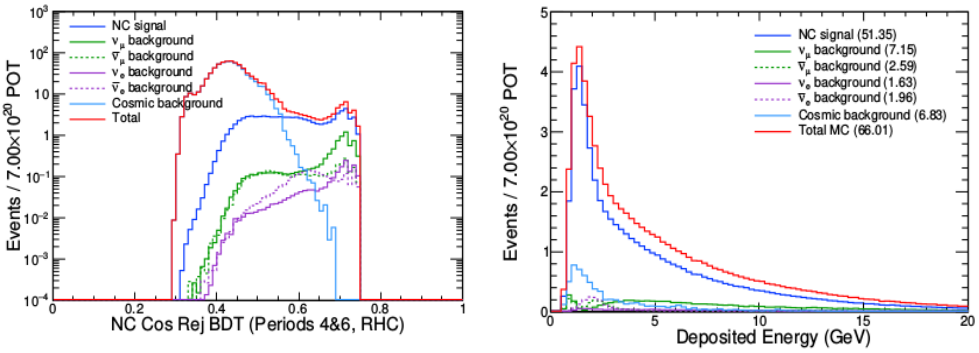

Figure 5.8: Left: the BDT response for the RHC MC data. Right: the distribution of deposited energy at the FD after applying cosmic rejection BDT cut.

5.2.6 NC Selection

The primary purpose of the NC selection is to separate NC events from the CC events, but may also remove further cosmic events from the sample. The CVN NC identifier is used for this purpose and is summarized in Sec. 4.1.2. This analysis uses an updated CVN from the previous analysis, known as CVN Short Simple (CVNss). The changes over the previous CVN (CVN2017) include modifications to the network architecture for improvements to classification performance and the inputs to the algorithm training. The new CVN was also trained separately for FHC and RHC MC. The distribution of CVN at the FD and ND, after applying all cuts except CVN are shown in Fig. 5.9. The tuned cuts are detailed in the Table 5.21. To remove the regions of low efficiency and significant threshold effects, a cut on the number of hits and the total deposited energy are implemented. The number of events selected after the CVN cut is tabulated in the Table 5.23 for ND and Table 5.22 for FD.

Parameter used for selection	Cut
CVN NC Identifier value for RHC analysis	≥ 0.23
CVN NC Identifier value for FHC 2017	≥ 0.20
Number of Hits	≥ 25
Deposited Energy	$0.5 < \text{Energy(GeV)} < 20$

Table 5.21: NC selection cuts to reject CC events, leaving a relatively pure sample of NC events.

Cut Level	NC	$\nu\,(\overline{\nu})$	$\nu_\mu\left(\overline{\nu}_\mu\right)$ CC	$\nu_e\,(\overline{\nu}_e)$ CC	ν_τ CC	cosmic
DQ+EQ	142	59.1(82.5)	30.8(14.1)	3.69(3.39)	2.79	263940
+Cont	97.4	37.5(59.9)	9.3(4.1)	2.0(2.0)	1.68	2753
+Backward	96.1	37.1(59.0)	9.2(4.0)	2.0(2.0)	1.67	2633
+Slc Time	95.7	36.9(58.8)	9.2(4.0)	2.0(2.0)	1.66	2464
+Shw ptp	89.3	34.9(54.5)	8.8(3.8)	1.9(1.9)	1.60	1223
+BDT	51.3	26.1(25.2)	7.1(2.5)	1.7(1.6)	1.47	6.81
+CVN	49.1	24.9(24.2)	4.6(1.5)	1.0(0.9)	1.3	5.34

Table 5.22: The number of events that pass the cut levels at FD.

Cut Level	NC	$\nu\,(\overline{\nu})$	$\nu_\mu\,(\overline{\nu}_\mu)$ CC	$\nu_e\,(\overline{\nu}_e)$ CC
DQ at ND ($\times 10^6$)	2.76	1.27(1.49)	9.61(10.6)	0.21(0.14)
+EQ at ND ($\times 10^6$)	21.0	0.98(1.16)	8.73(9.88)	0.16(0.11)
+Fid+Cont at ND ($\times 10^3$)	116	32.1(83.5)	34.3(90.7)	3.58(4.47)
+CVN at ND ($\times 10^3$)	52.6	17.6(34.9)	6.24(7.21)	0.43(0.34)

Table 5.23: The number of events that pass the cut levels at the ND. Here the number of $\nu_\tau\,(\overline{\nu}_\tau)$ CC and cosmic events are turned out to be zero.

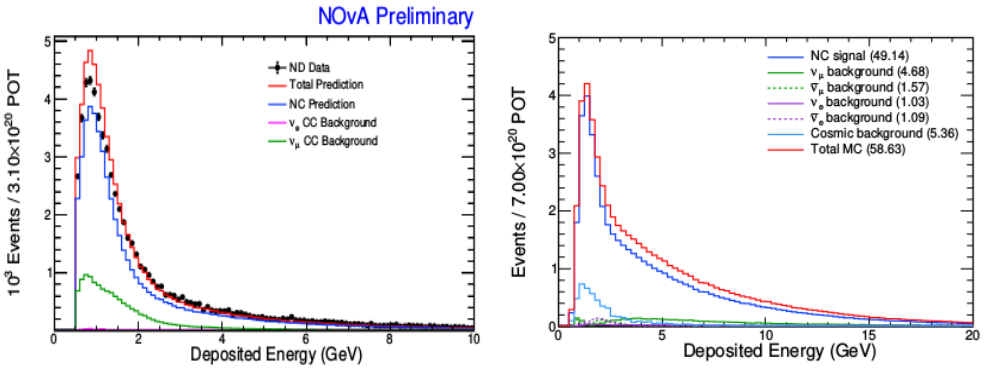

Figure 5.9: The distribution after CVN selection cut is applied. In the ND (left) and the FD (right).

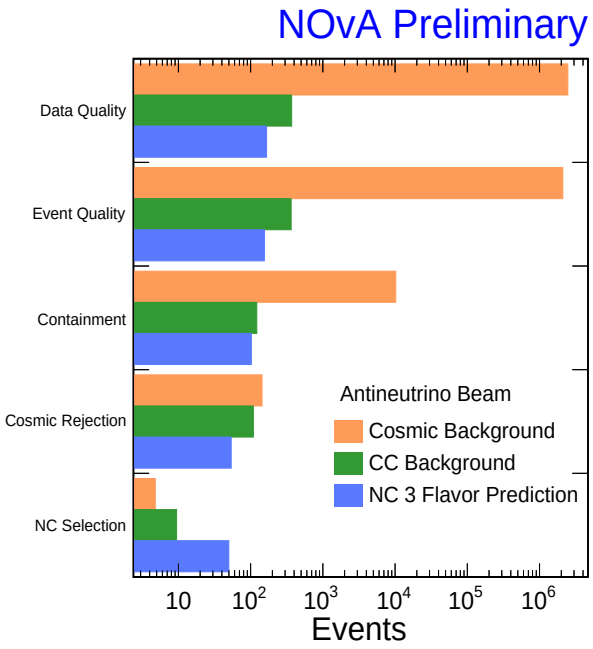

Figure 5.10: The effect of the each cut-level in the antineutrino NC disappearance analysis.

5.3 Efficiency and Purity

The efficiency and purity are important parameters used in optimizing the event selection. The efficiency can be defined as,

$$\text{Efficiency}(E) = \frac{\text{Number of selected signal events}}{\text{Total number of signal events}}. \tag{5.1}$$

It gives the metric for the percentage of signal events selected. The purity can be defined as,

$$\text{Purity}(P) = \frac{\text{Number of selected signal events}}{\text{Total number of selected events}}. \tag{5.2}$$

This give a metric for how pure the selected sample is. Table 5.24 compares the 2017 FHC analysis and 2019 RHC analysis in terms of their efficiency and purity. We can see that our purity is higher in 2019 RHC, with only a slight decrease in efficiency in the ND.

Analysis	Efficiency (ND)	Purity (ND)	Efficiency (FD)	Purity (FD)
2017 FHC	50%	67%	52%	77%
2019 RHC	45%	78%	50%	77%

Table 5.24: Comparison of efficiency and purity for 2017 FHC and 2019 RHC analyses.

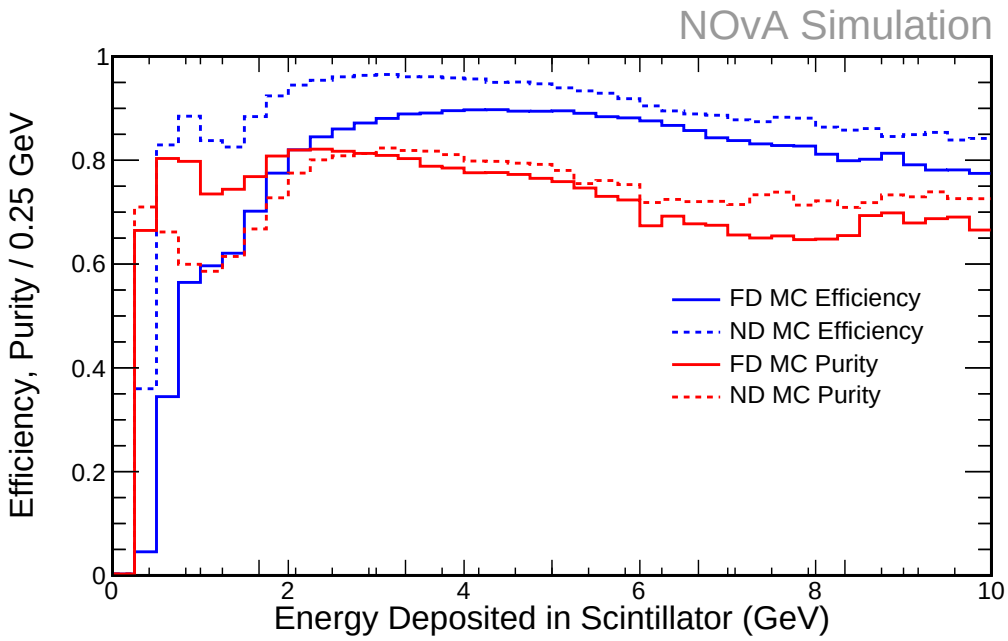

Figure 5.11: Efficiency-purity plot for the neutrino analysis. The X-axis of the plot ranges from 0 to 10 GeV.

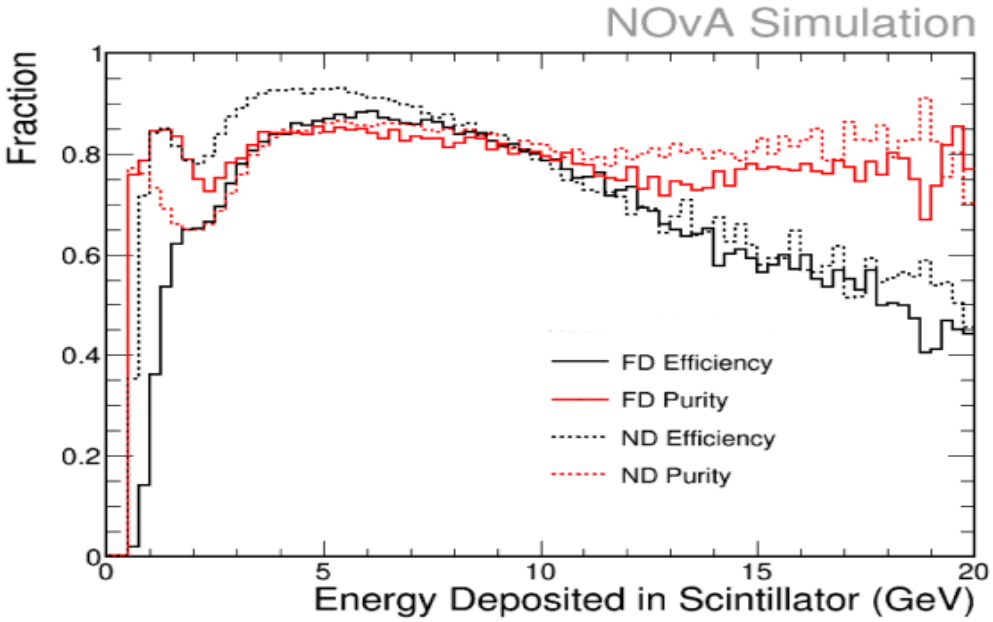

Figure 5.12: Efficiency-purity plot for the antineutrino analysis. The 'energy deposited' variable for the antineutrino analysis is in the range of 0 to 20 GeV.

6

Predicting FD NC distribution

6.1 Introduction

The CAFAna framework [113] is the foundation on which NOvA oscillation analyses are built. The NC disappearance analysis is no exception. CAFAna is basically a NOvA customized version of the CERN ROOT data analysis package. In essence, the CAF (Common Analysis File) format summaries the reconstruction of an event. The CAF file does not carry cellhit level information, instead it carry the slice level (interaction level) information. Interactions are resolved based on the space-time information of the cellhits. A slice stores its information in StandardRecord (SR) object, where the SR objects contains various ROOT Tree branches. The CAF files bring the complex interactions into the level of simple ROOT Tree, from there we can extract reconstructed information of a particular interaction according to the analysis requirement. Using the CAF files, the CAFAna framework enables us to do easy plotting and fitting with the help of its handy classes.

NOvA long-baseline oscillation analyses rely on the Far over Near extrapolation method (in short "Extrapolation method") [105, 106, 114–116] to get the FD prediction spectrum to compare with the FD observed spectrum. The next section summarizes the extrapolation method used in NC disappearance analyses.

6.2 Predicting the FD Spectrum through Extrapolation Method

In the extrapolation method, the ND data is used to predict the FD expectation (which is used to fit with FD data). This method of producing

the FD prediction is very effective in canceling out the systematics which affects both detectors in the same way, and one examples being the flux systematics. The sterile extrapolation method proceeds through the following steps:

- Decomposing ND data.
- Extrapolation to get unoscillated FD prediction.
- Applying oscillation weights to get the oscillated FD prediction.

6.2.1 ND Decomposition

The ND MC sample after applying the NC selection, will have a significant amount of CC interaction events that mimic NC signals. Typically these backgrounds are ν_μ CC events with short muon track and ν_e CC events with high hadronic energy deposition. These different components do not oscillate in a similar way. Hence we have to extrapolate each of these component separately.

As a first step, the ND data is decomposed in proportion to the different flavor components in the simulation. So, the data will have the same percentage of a component as that of simulation. This method is known as proportional decomposition.

6.2.2 Extrapolation Method to get an Unoscillated FD Prediction

The backbone of the extrapolation technique is the assumption that the events selected in ND are representative of the event topologies at the FD expectation. This is based on the fact that both detectors are functionally identical. In this step, the ND data is extrapolated to FD, with the help of ND MC and FD MC as shown in Eqn. 6.1. Extrapolation method yields a two dimensional histogram of each oscillation component, with true energy along the Y-axis and reconstructed energy along the X-axis. The FD prediction can be represented in terms of ND data and MC as:

$$\mathrm{FD}^{\mathrm{Pred}} = \quad \mathrm{ND}^{\mathrm{Data}} \cdot \frac{\mathrm{FD}^{\mathrm{MC}}}{\mathrm{ND}^{\mathrm{MC}}} \tag{6.1}$$

Where $\mathrm{ND}^{\mathrm{Data}}$ is the number of ND data events and $\mathrm{ND}^{\mathrm{MC}}$ and $\mathrm{FD}^{\mathrm{MC}}$ are the number of MC events in the ND and FD respectively.

The oscillation channels are classified as survival channels and appearance channels. The NC survival oscillation channel can be represented as, $\nu_\alpha \to \nu_\alpha$. Similarly, there are survival channels for the backgrounds like $\nu_\mu \to \nu_\mu$ and $\nu_e \to \nu_e$. Some fraction of the ν_μ background in the ND can be oscillated into ν_e background in the FD ($\nu_\mu \to \nu_e$), which is an example of the appearance channel.

The survival oscillation channels mentioned above are having $\mathrm{FD}^{\mathrm{MC}}$ corrected in bins of reconstructed energy. FD extrapolation for the NC events are given by,

$$\mathrm{FD}^{\mathrm{Pred}}_{\nu_a \to \nu_a}(E_j^{\mathrm{rec}}, E_i^{\mathrm{tr}}) = \frac{\mathrm{FD}^{\mathrm{MC}}_{\nu_a \to \nu_a}(E_i^{\mathrm{tr}}, E_j^{\mathrm{rec}})\mathrm{ND}^{\mathrm{Data}}_{a,S_{\mathrm{NC}}}(E_j^{\mathrm{rec}})}{\mathrm{ND}^{\mathrm{MC}}_{a,S_{\mathrm{NC}}}(E_j^{\mathrm{rec}})}. \tag{6.2}$$

This is applicable for all survival channel backgrounds and NC signals. NCs are a mix of $\alpha\nu_\mu$, $\beta\nu_e$ and $\gamma\nu_\tau$. Where α, β and γ are the percentage of ν_μ, ν_e and ν_τ in the beam. Under the standard three-flavor model, the values of α, β and γ changes as NC events travel to the FD, but the total amount of NC will be the same. So they are blind to the three-flavor oscillation. The four-flavor oscillation model can accommodate sterile neutrino oscillations. This allow some fraction of ν_μ, ν_e or ν_τ to oscillate into sterile neutrinos. This leads to the suppression of NC event rate at the FD. So we cannot treat NC as other components of oscillation. We have to split the FD extrapolated NC component ($\mathrm{FD}^{\mathrm{Pred}}$), proportional to their initial neutrino flavor.

But for the oscillation channels, the ν_e CC events (background to FD NC events) are appeared at the FD as a result of oscillation from ND ν_μ events. The ν_μ selection is applied at ND and NC selection at FD. So, the $\mathrm{ND}^{\mathrm{Data}}/\mathrm{ND}^{\mathrm{MC}}$ ratio should apply in true energy bins[1] of $\mathrm{FD}^{\mathrm{MC}}$.

[1]
$$\mathrm{FD}^{\mathrm{Pred}}_{\nu_\mu \to \nu_e, S_{\mathrm{NC}}}(E_j^{\mathrm{rec}}, E_i^{\mathrm{tr}}) = \frac{\mathrm{FD}^{\mathrm{MC}}_{\nu_\mu \to \nu_e, S_{\mathrm{NC}}}(E_i^{\mathrm{tr}}, E_j^{\mathrm{rec}})\mathrm{ND}^{\mathrm{Pred}}_{\nu_\mu, S_\mu}(E_i^{\mathrm{tr}})}{\mathrm{ND}^{\mathrm{MC}}_{\nu_\mu, S_\mu}(E_i^{\mathrm{tr}})} \tag{6.3}$$

ND ν_μ background prediction $\mathrm{ND}^{\mathrm{Pred}}_{\nu_\mu, S_\mu}(E_i^{\mathrm{tr}})$ takes the form,

$$\mathrm{ND}^{\mathrm{Pred}}_{\nu_\mu, S_\mu}(E_i^{\mathrm{tr}}) = \sum_k \frac{\mathrm{ND}^{\mathrm{Data}}_{\nu_\mu, S_\mu}(E_k^{\mathrm{rec}})\mathrm{ND}^{\mathrm{MC}}_{\nu_\mu, S_\mu}(E_i^{\mathrm{tr}}, E_k^{\mathrm{rec}})}{\mathrm{ND}^{\mathrm{MC}}_{\nu_\mu, S_\mu}(E_k^{\mathrm{rec}})} \tag{6.4}$$

where E_i^{tr} is ith true energy bin, S_μ is ν_μ selection and E_k^{rec} is reconstructed energy in k^{th} bin. $\mathrm{ND}^{\mathrm{Data}}$ and $\mathrm{ND}^{\mathrm{MC}}$ are ND data and MC event rates.

6.2.3 Getting the Oscillated FD prediction

In this stage, the oscillation probabilities are applied to the true energy bins of the extrapolated 2D spectra. This yields a one dimensional reconstructed energy spectrum. It is impossible to measure $P_{\nu_a \to \nu_{\text{Sterile}}}$ directly, as the sterile neutrinos (ν_{Sterile}) do not interact with matter via any of the standard model interactions. We circumvent it by finding the probability of oscillating the NC events into any active neutrino flavor. Since, $P_{\nu_a \to \nu_{\text{Active}}} = 1 - P_{\nu_a \to \nu_{\text{Sterile}}}$. The FD extrapolated prediction for an NC component with initial flavor a:

$$\text{FD}^{\text{Pred}}_{\text{NC}(a),S_{\text{NC}}}(E_i^{\text{tr}}) = \sum_i \text{FD}^{\text{Pred}}_{\text{NC}(a),S_{\text{NC}}}(E_i^{\text{tr}}, E_j^{\text{rec}}) P_{\nu_a \to \nu_{\text{Active}}}(E_i^{\text{tr}}) \qquad (6.5)$$

where $\text{FD}^{\text{Pred}}_{\text{NC}(a),S_{\text{NC}}}$ is the predicted NC events with initial neutrino flavor component a and the NC selection. The NC component of the prediction is multiplied by the probability of oscillation from a particular flavor to any active flavor ($P_{\nu_a \to \nu_{\text{Active}}}$) which gives the appropriate NC proportion that originate as flavor a. This is done for a= ν_μ, ν_e and ν_τ. The final NC signal prediction is produced by summing individual prediction components with different a. The background prediction is obtained by summing over the extrapolated predictions of other oscillation channels. Finally the total FD prediction, in bins of reconstructed energy, is calculated by summing all of the signal and backgrounds predictions together.

The main analysis components like the analysis framework, event selection, and systematics have been discussed so far. We have to evaluate the performance of our analysis, before looking at the results of the analysis. Sideband study and comparing the ND data/MC distribution are the cross-checks implemented for evaluating the analysis performance and understanding the simulated data well. The following sections are dedicated to these cross-checks.

6.3 Sideband Studies

Sideband studies are conducted in both the FHC and RHC analyses to evaluate their performance. The sideband studies are basically investigating the FD data/MC spectrum, in a region just outside of our analysis. The following subsections are describing the sideband studies for the FHC and RHC analysis.

6.3.1 FHC Analysis

For the FHC analysis, we have looked into the distribution of 'Energy Deposited' in a Mid-BDT range, i.e. the cosmic rejection BDT score is in between 0.42 and 0.62. We have seen that our BDT selection cut is at 0.62 and all the events that fall above this value are selected for the analysis. So we intended to look into the Deposited Energy distribution in a range of BDT values 0.42 and 0.62 The distribution is shown in Fig. 6.4.

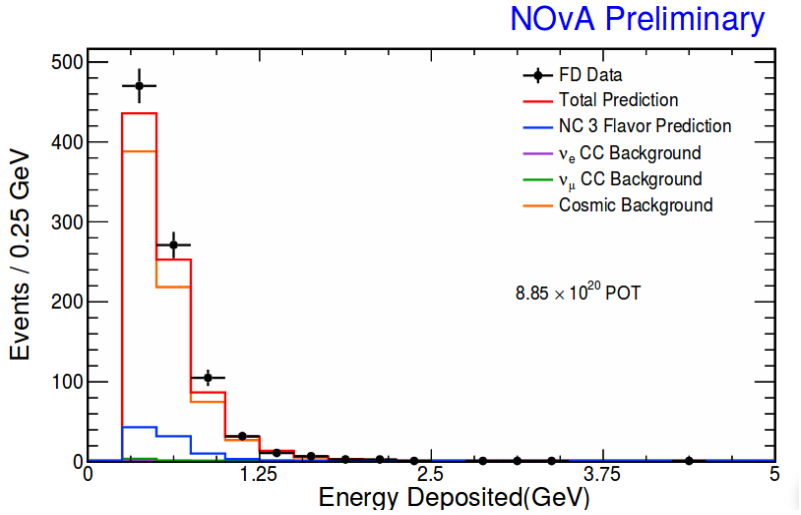

Figure 6.1: Mid-BDT sideband plot for the FHC 2017 analysis.

There are 907 events in this region while 878.98±30.31(stat.)±11.3(syst.) are predicted. Systematic uncertainty is taken from the signal region. The total MC can be divided as 98.93 NC events, 769.39 cosmic events, 7.58 ν_μ events and 2.84 ν_e events.

6.3.2 RHC Analysis

Before examining the FD data in this analysis, we used the ND data to produce a data driven prediction at the FD. This FD prediction is compared with the FD data in the analysis sideband region. The analysis sideband region will be populated with the events which used to fail the BDT selection criteria. Chosen region of low BDT response (< 0.55) would fail cosmic rejection cuts for making sideband plots. The variables energy

deposited, CVN and Number of hits (NHit) are plotted in the low BDT region.

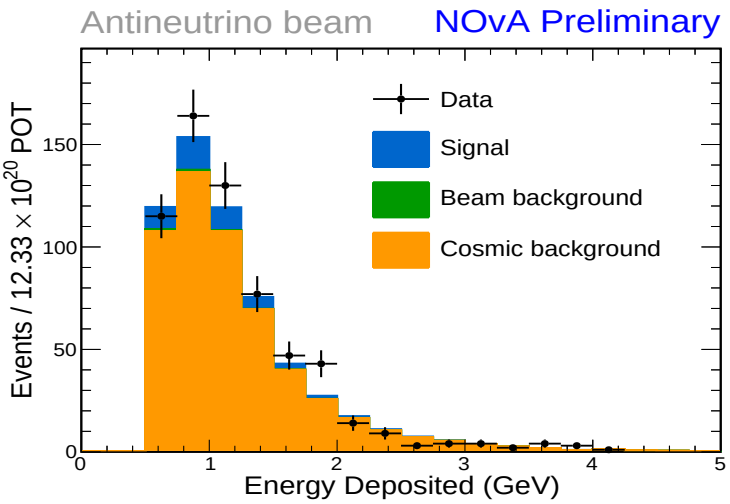

Figure 6.2: Low BDT sideband plot for the variable, Energy Deposited.

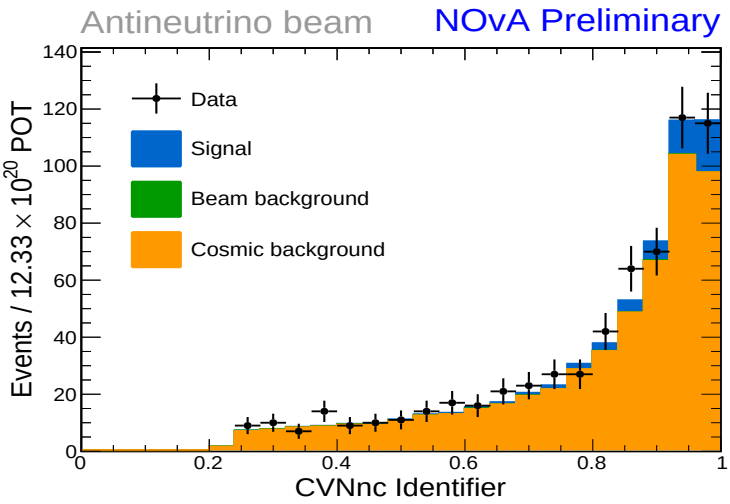

Figure 6.3: Low BDT sideband plot for the variable, CVN.

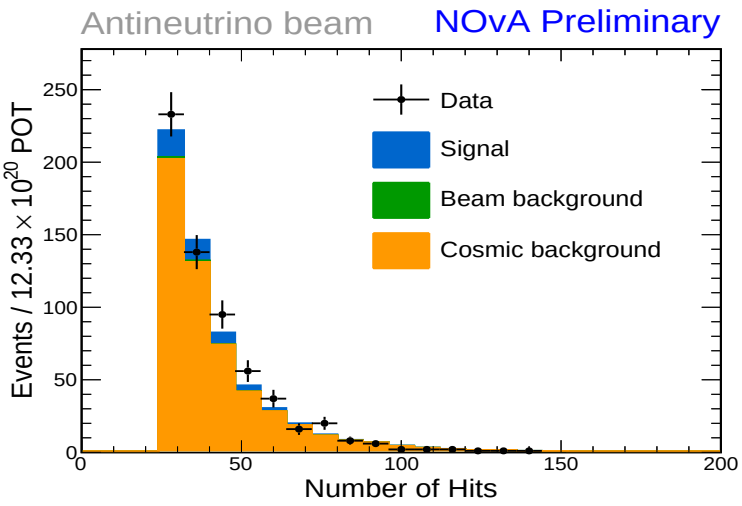

Figure 6.4: Low BDT sideband plot for the variable, number of hits.

We can see an excellent data/MC agreement for FHC and RHC analyses. The data and MC matches within 1σ

6.4 ND Data/MC Comparison

To test whether our analysis is robust, we are comparing the ND data with the MC simulation which is scaled to the data POT. This gives us an insight into how effectively our simulation represents data. The main checkpoint is if our data points are covered in the systematic uncertainty band. It is a litmus test to see how the efforts in upgrading the GENIE neutrino interaction, detector simulation, photon transport, electronics modeling improved our simulation to match with the data.

6.4.1 FHC Analysis

The data/MC comparison plots for the variables used for the selection of NC events are plotted. This gives a measure of the robustness of our analysis. Figs. 6.5–6.7 shows the data/MC comparison the variables that used in developing the NC event selection. The red dotted line in the figure shows where we fixed selection cuts.

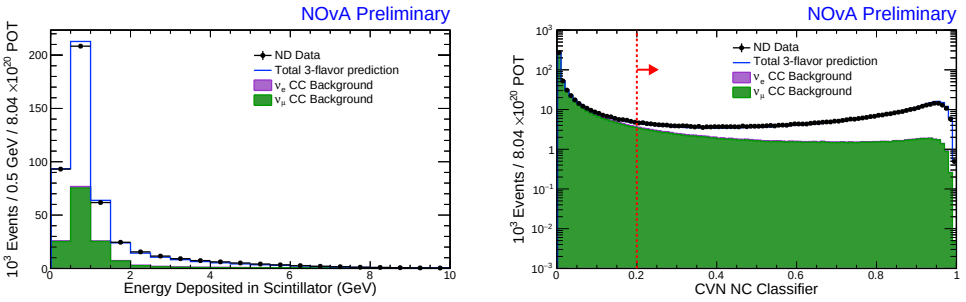

Figure 6.5: These are the data/MC comparison plot of the ND distribution of Energy Deposited (left) and CVN (right).

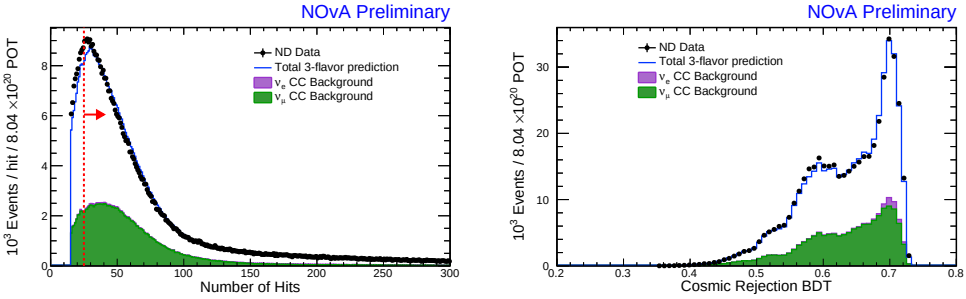

Figure 6.6: The data/MC comparison for ND Number of hits distribution (left) and BDT distribution (right).

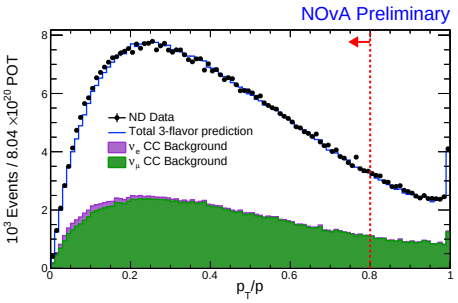

Figure 6.7: The data/MC comparison for the transverse momentum fraction variable.

6.5 RHC Data/MC Comparison Plots

The data/MC comparison for the RHC ND variable distribution is also analyzed to test its robustness. Figs. 6.8 and 6.9 show the ND data/MC comparison of some of the important parameters.

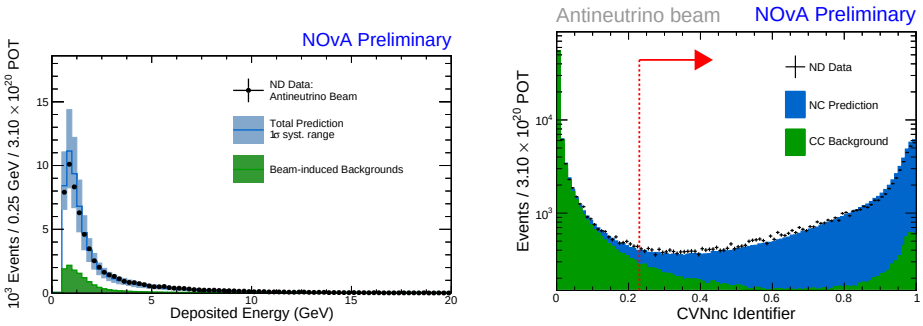

Figure 6.8: The data/MC comparison plot of the ND distribution of Energy Deposited (left) and CVN (right).

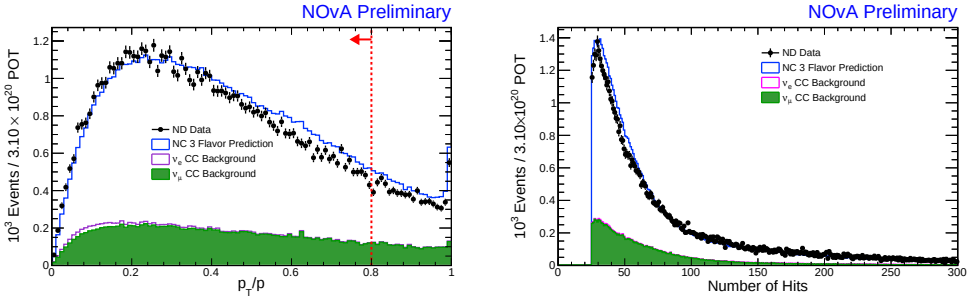

Figure 6.9: ND data/MC comparison of the transverse momentum fraction (left) and the number of hits (right).

7 Systematic Uncertainties

7.1 Introduction

Systematic uncertainties are introduced by inaccuracies (involving either the observation or measurement process) inherent to the system. They play a key role in the measurement of physical quantities and often they are of comparable size to the statistical uncertainties (based on stochastic fluctuations of random measurements). One of the properties that make the systematics uncertainty different from the statistical uncertainty is that for two independent measurements of a physical quantity their systematic uncertainties are correlated. NOvA oscillation measurements come across many potential sources of systematic uncertainties such as beam simulation, detector modeling, neutrino interaction modeling and oscillation parameters. We will discuss more of them in the following sections.

7.2 Systematic Uncertainties in NOvA NC Disappearance FHC analysis

The NOvA NC disappearance analysis is affected by several systematic uncertainties. The effect of each systematic uncertainty on the signal and background are different. The experiment has two functionally identical detectors and ND data is used to constrain the FD prediction. Hence those systematic uncertainties which similarly affect both detectors cancels out. There are some other systematics which affects both detectors separately and do not cancel as well.

The general strategy for the NC disappearance analysis is extracting the FD prediction using the ND data driven technique. So, this analysis adopted the general strategy of finding systematic uncertainty by looking

at the shift between the predicted spectrum produced with and without applying the systematic effect. These systematic effects are applied either by using shifted MC samples or by applying weights to the simulated spectra from standard MC at either or both detectors (for absolute or relative uncertainties). The deviation from the nominal predicted spectra at the FD is then quantified as the uncertainty. The three-flavor oscillation is implemented to make the FD oscillated prediction. Systematic uncertainties estimated for this analysis are:

- Beam systematics.
- Calibration of the detectors.
- Light level systematics.
- Cross section systematics.
- Break down of ND composition.
- Difference in acceptance of ND and FD.
- Three flavor oscillation parameters systematics.

7.2.1 Beam Systematics

The beam systematic uncertainties can be broadly classified as:

- Beam transport systematics.
- PPFX Flux simulation systematics.

Beam Transport Systematics

The uncertainties in the NuMI beam is important in the NOvA oscillation analyses, since it is the input to the entire analysis framework. Beam simulation systematics is one of the major systematic uncertainty when we look at the ND and FD prediction separately. But when we use the extrapolation technique to predict the FD spectrum, the beam simulation uncertainty cancels well between detectors. The beam systematic uncertainty is quantified by varying one of the geometry parameter while simulating the NuMI beam and estimating its effect in the analysis. The main geometric variables those are varied to find the beam transport systematic uncertainties are:

- Varying the Horn current by 100± 2 kA (for FHC) and -100± 2 kA (for RHC).
- The magnetic horn-1 position is shifted by ± 3 mm in X and Y separately.
- The magnetic horn-2 position is shifted by ± 3 mm in X and Y separately.
- The beam position in the target is shifted ± 1 mm in X and Y separately.
- The beam spot size is changed ± 0.2 mm in X and Y (from the nominal value of beam spot size 1.3 mm in X and Y)
- Changing horn water layer by ± 1 mm (the nominal water layer is 1 mm).
- Target z position is shifted along Z by ± 7 mm (the nominal value is -143.3 cm).
- Full stat simulation files with magnetic field in the decay pipe.

The effect of varying all of these together in quadrature can be seen in Figs. 7.1a – 7.1f. The Fig. 7.1a shows the ND simulated NC event distribution, while Figs. 7.1b is the ND simulated CC event distribution. Figs. 7.1c and 7.1d are FD simulated NC and CC distributions. Figs. 7.1e and 7.1f are FD extrapolated NC and CC event distributions.

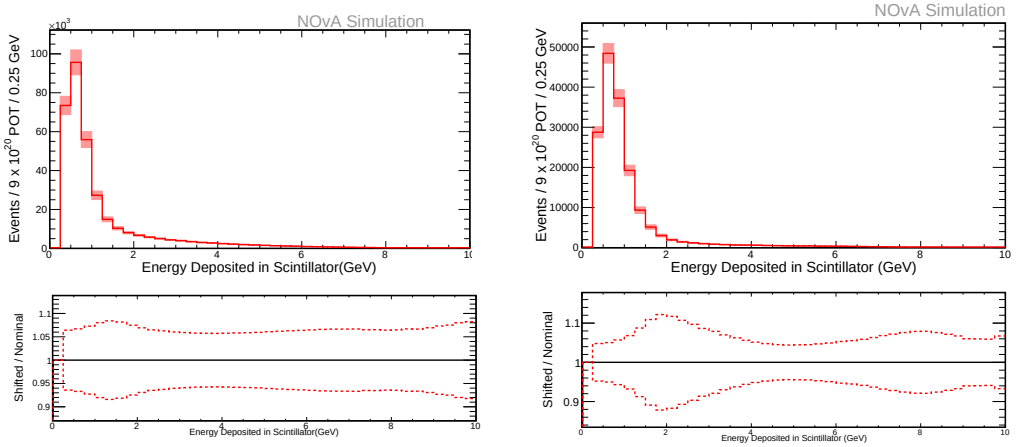

(a) ND simulated NC events

(b) ND simulated CC events

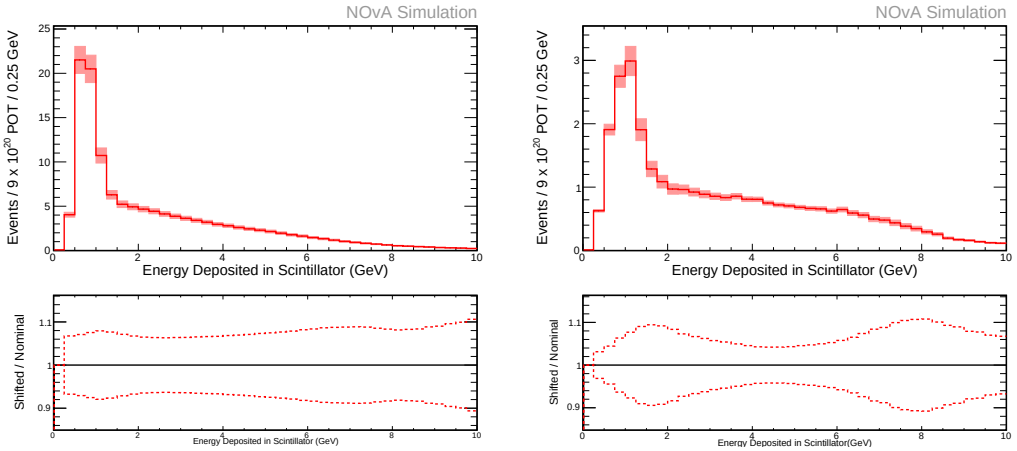

(c) FD simulated NC events

(d) FD simulated CC events

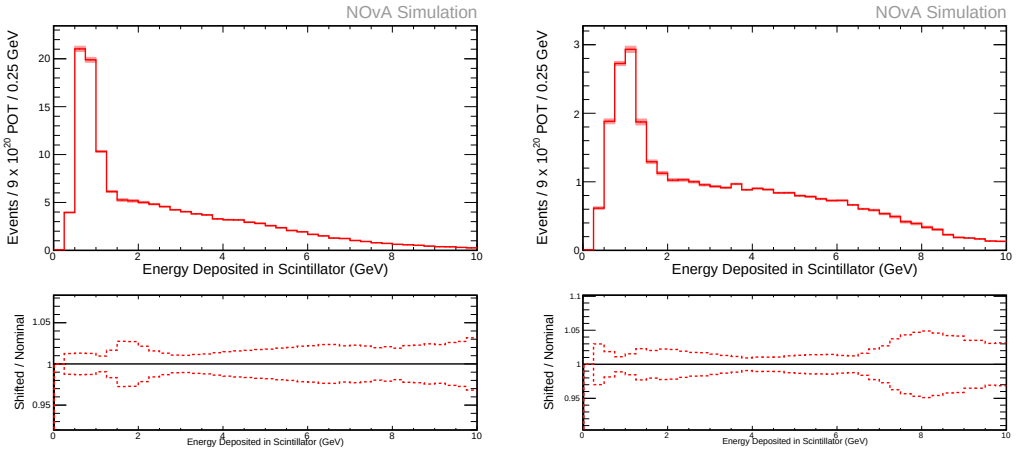

(e) FD NC extrapolated prediction

(f) FD CC extrapolated prediction

Figure 7.1: Total beam transport systematic uncertainty in different samples. The ratio plot represents the number of shifted/nominal events in each bin.

PPFX Flux Systematics

The PPFX Flux systematics deals with the uncertainties in the beam simulation from the target hadron production. It is a data driven technique using the data from the experiment and finds the correction value to the MC. This correction considers the probability of interaction to happen and the probability of getting a particular final-state particle. In this analysis, we have used the multiuniverse technique to propagate uncertainties. Each universe is created by assigning a random value to each free parameter. Here several universes are produced and propagate through the extrapolation framework (detailed in Ch. 6). The procedure followed by this analysis can be listed as:

- An ensemble of 100 universes is created at the ND and the 1σ variation from the central value of the universes is found. The shift of the one sigma boundary from nominal ND spectra is quantified.
- Repeat the same procedure at the FD to find the FD PPFX systematic error.
- The ensemble of 100 ND Universes are passed through the extrapolation framework and then the FD 1σ variation is found. A nominal FD spectra is predicted by extrapolation of nominal ND spectra to FD.

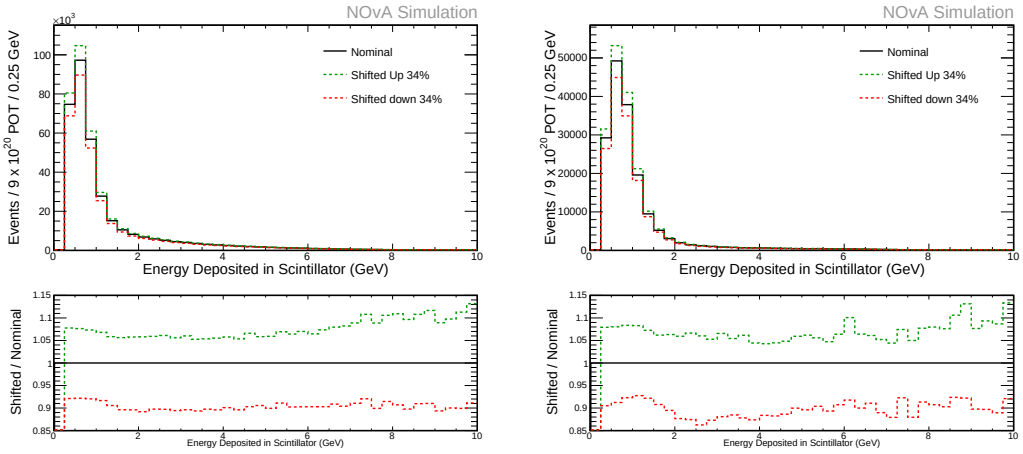

Figure 7.2: Total PPFX systematics in the ND. Left plot is the NC distribution and right plot is the CC background distribution.

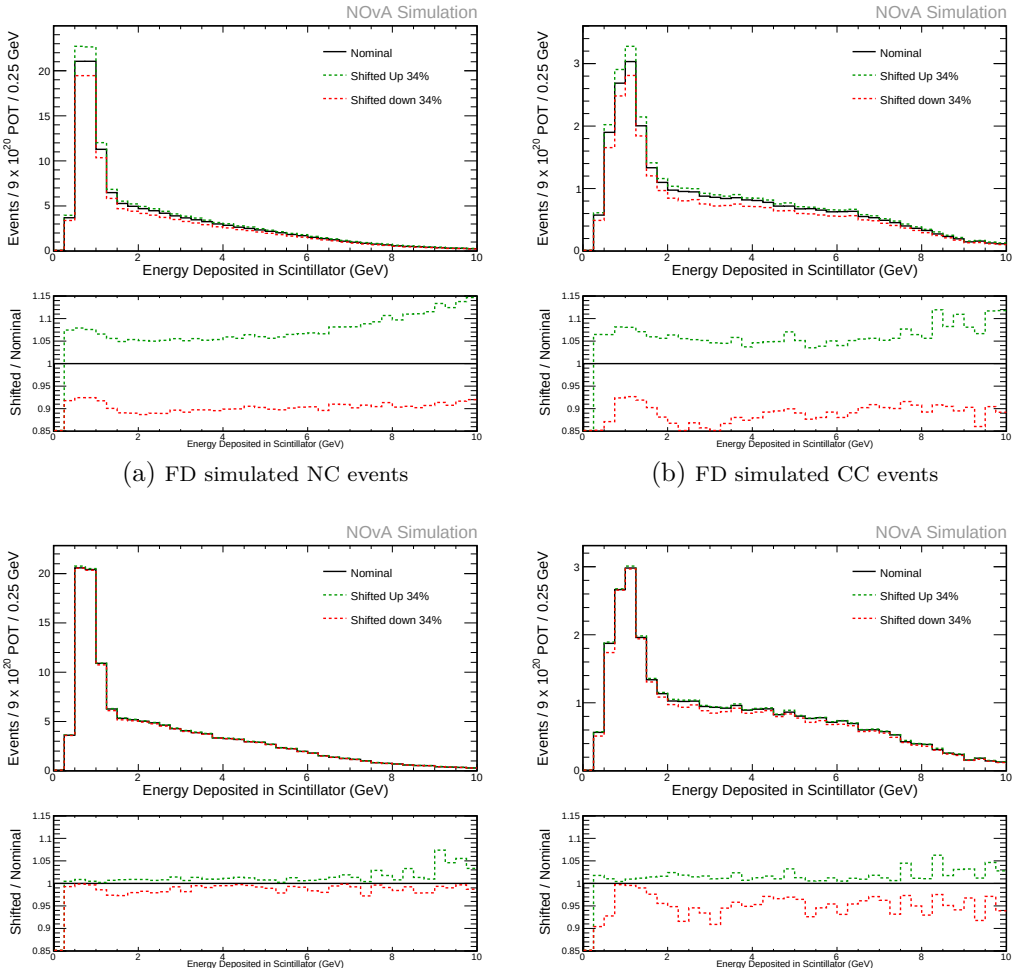

(a) FD simulated NC events

(b) FD simulated CC events

(c) FD NC extrapolated prediction

(d) FD CC extrapolated prediction

Figure 7.3: PPFX systematic uncertainty in different samples. The ratio plot represents the number of shifted/nominal events in each bin.

7.2.2 Neutrino Interaction Cross Section Systematics

The neutrino nucleus interaction is the source of large systematic uncertainties. The neutrino interactions in the NOvA detector are simulated using the GENIE event generator. It is provided with a detailed physics modeling of cross section, hadronization, and final-state interactions. The

GENIE modeling parameters control the systematics fluctuations. GENIE authors have provided the σ shifts for these parameters and these are added as weights in the CAFAna files. This allows us to make spectra within the suggested range and shifted FD predictions. Along with these, there are additional cross section uncertainties based on the NOvA specific cross section tuning. The systematic contribution of the parameter which have a shift far below 1% are summed together. The parameters which have a considerable shift are used individually in the fit. Figs. 7.5a to 7.4 show the total cross section systematic uncertainty for the ND MC simulation, FD MC simulation and FD extrapolated prediction.

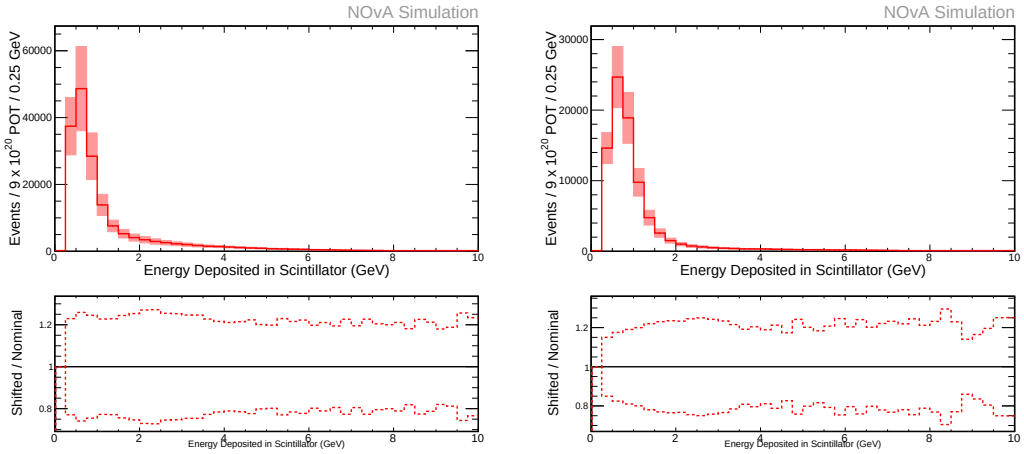

Figure 7.4: Total GENIE systematic uncertainty in the ND MC simulation. Left plot is the NC distribution and the right plot is the CC background distribution.

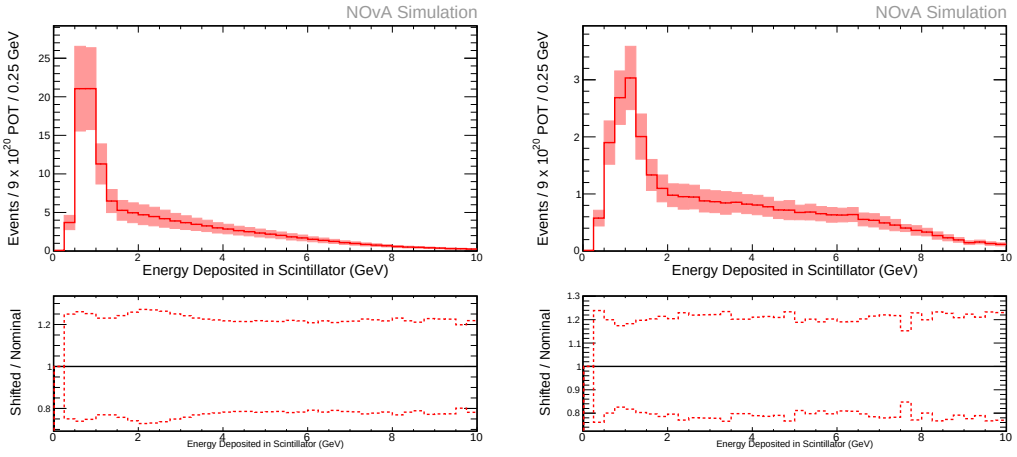

(a) FD MC simulated NC

(b) FD MC simulated CC

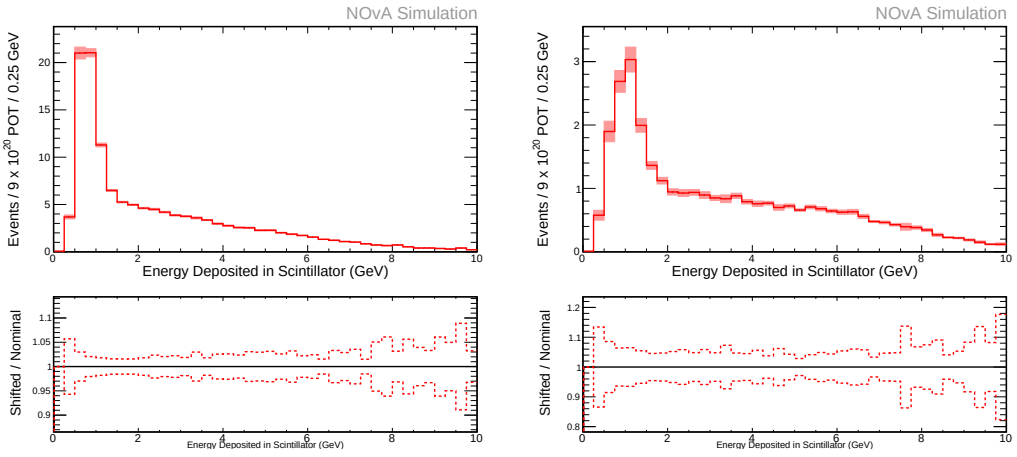

(c) FD NC extrapolated prediction

(d) FD CC extrapolated prediction

Figure 7.5: Total GENIE systematic uncertainty in different samples. The ratio plot represents the number of shifted/nominal events in each bin.

7.2.3 Calibration Systematic

The energy response is not uniform throughout a detector and also, the energy response of the ND is different from that of the FD. Calibration methods are implemented to make the uniform energy response in a particular detector and also between the detectors. The calibration procedure implemented can be a potential source of uncertainty that is known as the

calibration systematics. The calibration systematics is investigated using the MC samples with added miscalibration. This added miscalibration can be a shape variation or a constant overall scale miscalibration. The shape calibration systematics comes from the uncertainty in the PE to PEcorr conversion[1]. The uncertainty in converting PEcorr to MeV can cause a constant overall scale shift.

Absolute Calibration

Absolute calibration systematic uncertainty in each detector is calculated by finding the energy shift from the nominal spectrum to the spectrum produced out of fabricated miscalibration or shifted files. Just inputting one of the shifted files to the extrapolation framework either at the ND or the FD and then finding the difference between the nominal and the shifted spectra would provide the corresponding systematic shift. In addition to that, we have used miscalibrated files that have an engineered systematic shape variation and found the corresponding systematic shift. Figs. 7.6a to 7.6f show the absolute calibration shifts.

Relative Calibration

Relative calibration systematic uncertainty quantify the uncertainty that arises as a result of the difference in energy response between the detectors. These fabricated files are having a constant 5% calibration scale up or down. The resulting files are ND 5% calibration up, ND 5% calibration down, FD 5% calibration up and FD 5% calibration down. Applying one of these shifts one at a time and pick the maximum systematic shift from the nominal spectra. Repeating the procedure with other permutations of the shifted files would give corresponding shifts. The shift in each detector form different permutation of the shifted files is added in quadrature to get overall relative calibration systematics in each detector. Figs. 7.7a – 7.7f show the absolute calibration shifts for different samples.

[1]More details can be found in Sec. 3.1.1

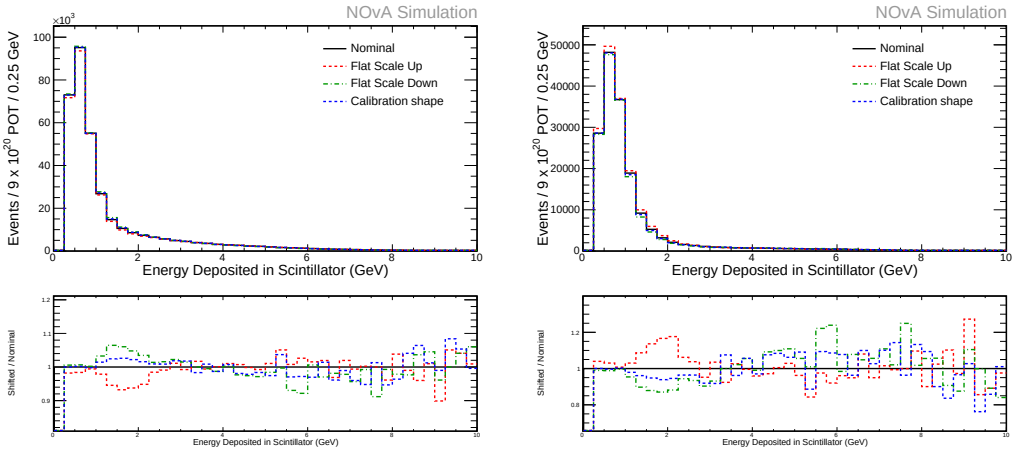

(a) ND simulated NC events

(b) ND simulated CC events

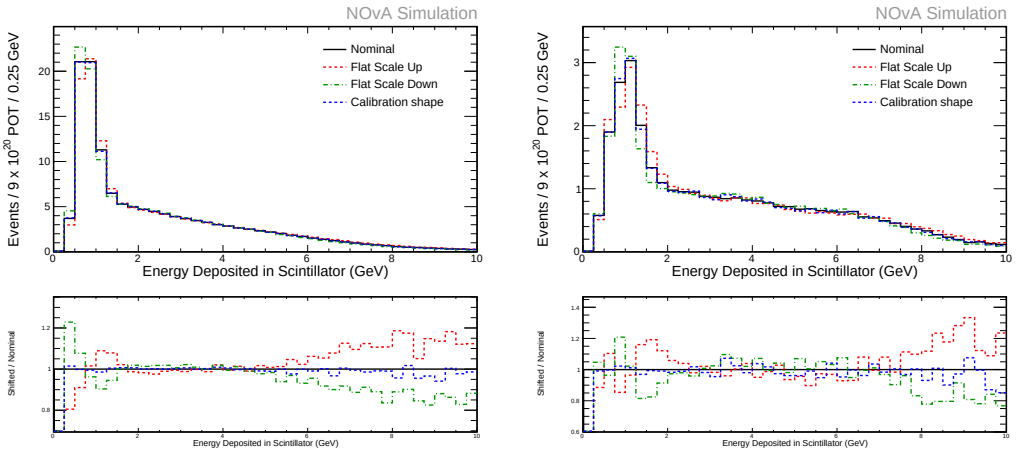

(c) FD simulated NC events

(d) FD simulated CC events

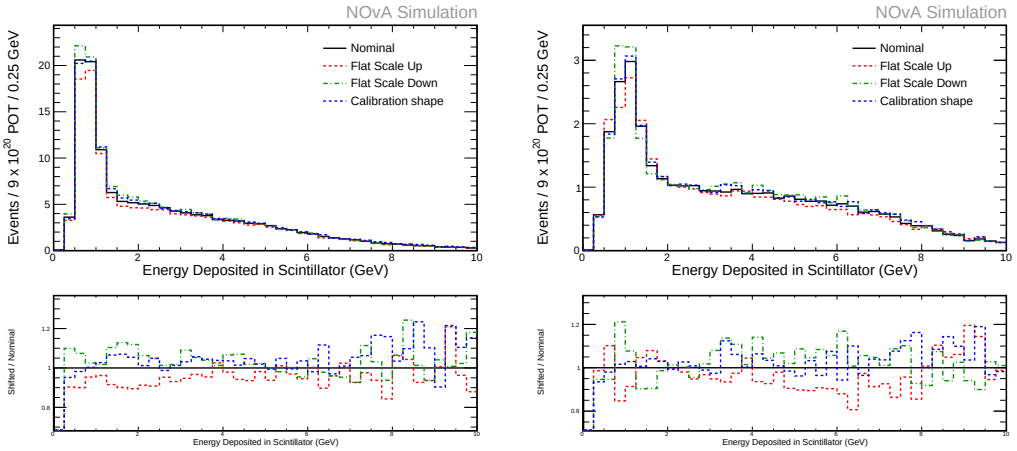

(e) FD NC extrapolated prediction

(f) FD CC extrapolated prediction

Figure 7.6: Total Absolute calibration systematic uncertainty in different samples. The ratio plot represents the number of shifted/nominal events in each bin.

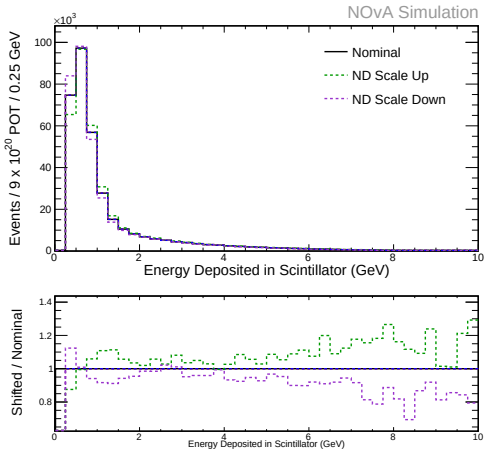

(a) ND simulated NC events

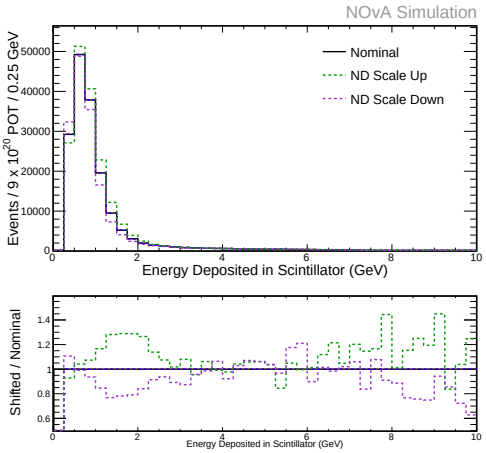

(b) ND simulated NC events

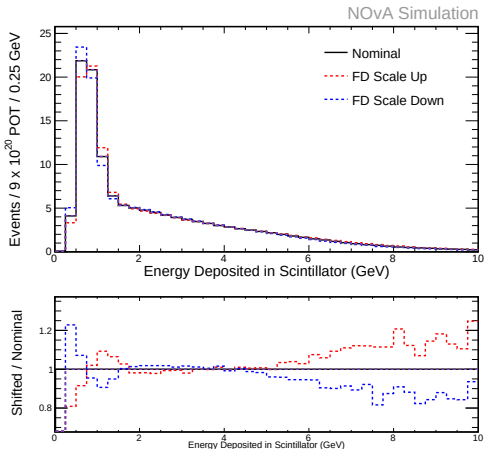

(c) FD simulated NC events

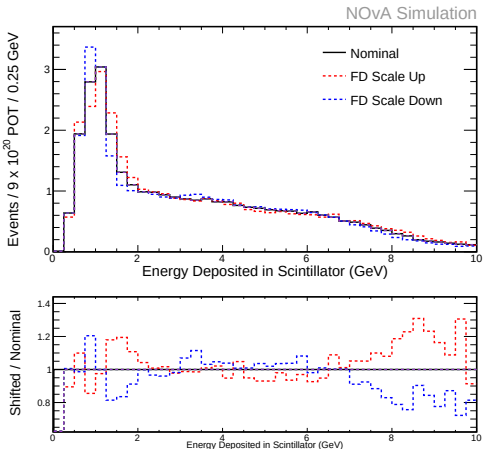

(d) FD simulated CC events

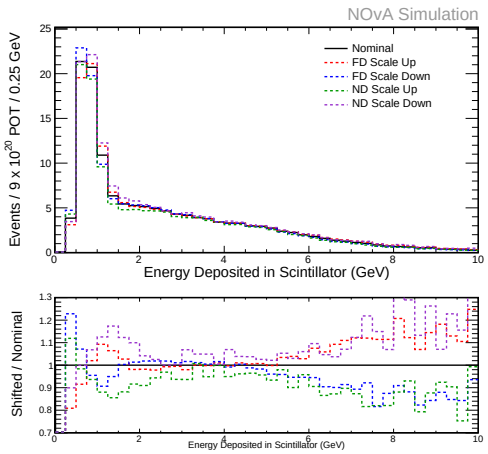

(e) FD NC extrapolated prediction

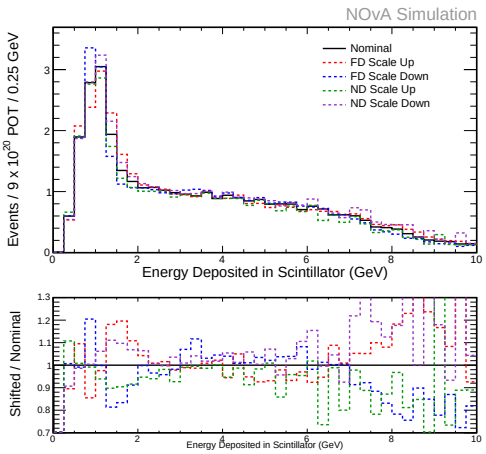

(f) FD CC extrapolated prediction

Figure 7.7: Total Relative calibration systematic uncertainty in different samples. The ratio plot represents the number of shifted/nominal events in each bin.

7.2.4 Cherenkov and Light Level Systematics

In this analysis, a Cherenkov light emission model has been added to the detector simulation [117]. The Cherenkov light response of the detector for the muon energy deposition is not similar to that of the proton energy deposition. So, in this analysis we considered a potential systematic effect that may arise as a result of uncertainty in Cherenkov light modeling. The uncertainty is taken into account for the relative matching of data/MC energy attenuation profile, (dE/dx) between muons and protons. Differences seen are at the 3% level and data is always seen to be lower than the MC so, only a downward shift is included. For this, a suit of fabricated Cherenkov files are produced and the corresponding systematic effects are quantified.

The light level systematic uncertainty is designed to account for the extent of attenuation profiles match in data and MC. A 5% disagreement have seen at the high and low tails when we looked at the PE/path length as a function of the distance to end of readout (taken as W). The uncertainty is taken as a flat shift. The calibrations and overall light levels are shifted in opposite directions to mimic the effect of observing a higher or lower light level. Figs. 7.8a–7.8f show this shift. An additional systematic uncertainty study known as the method systematics is carried out to understand the potential systematic effect, that may arise from the method used to simulate photon transport. The shift in spectra produced is studied using the non-shift files and nominal files. The non-shift files are produced without the current photon transport model in the simulation.

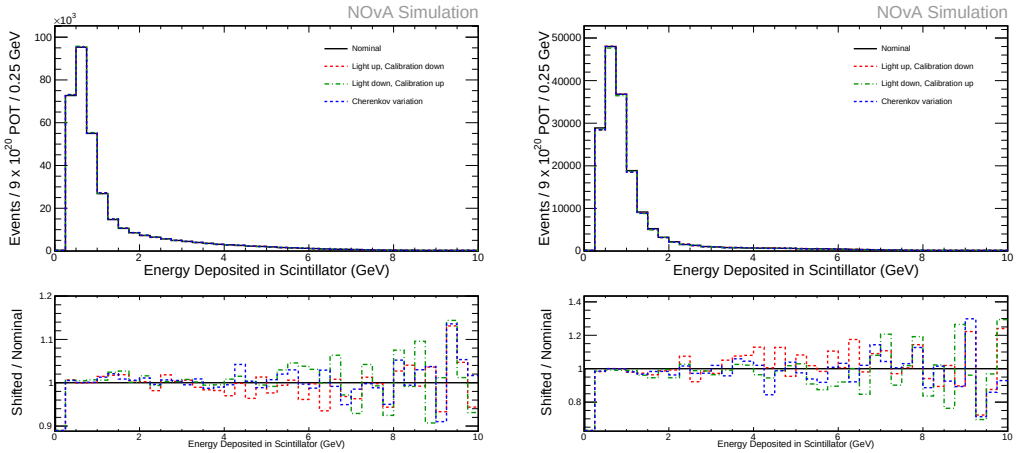

(a) ND simulated NC events

(b) ND simulated CC events

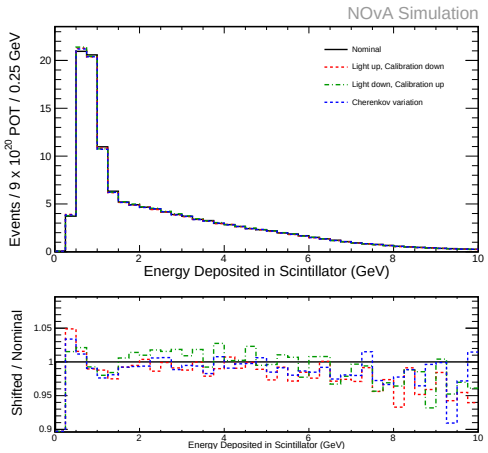

(c) FD simulated NC events

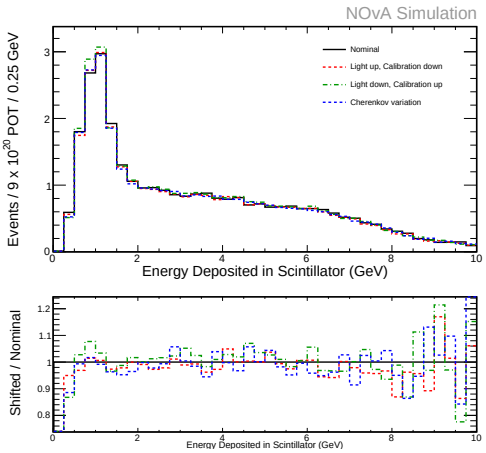

(d) FD simulated CC events

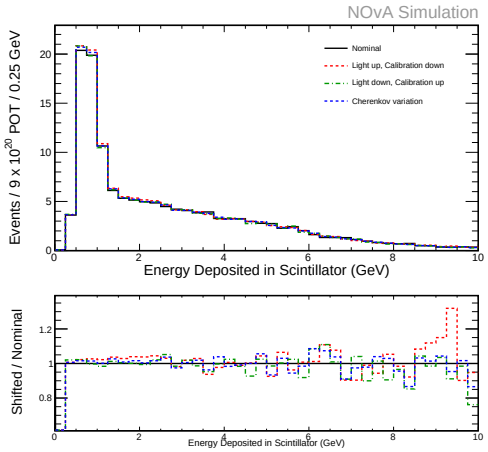

(e) FD NC extrapolated prediction

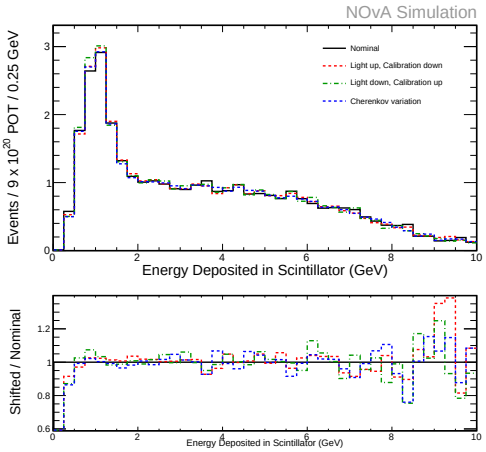

(f) FD CC extrapolated prediction

Figure 7.8: Light level systematic uncertainty in different samples. The ratio plot represents the number of shifted/nominal events in each bin.

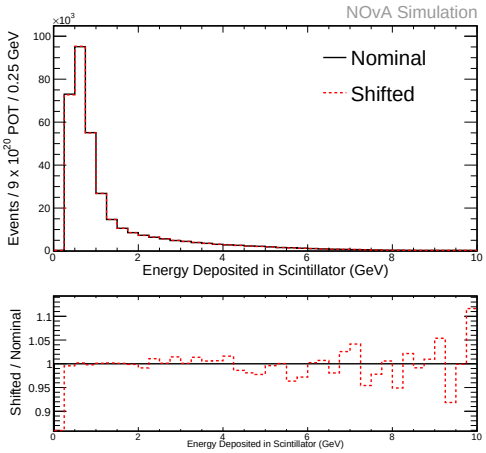

(a) ND simulated NC events

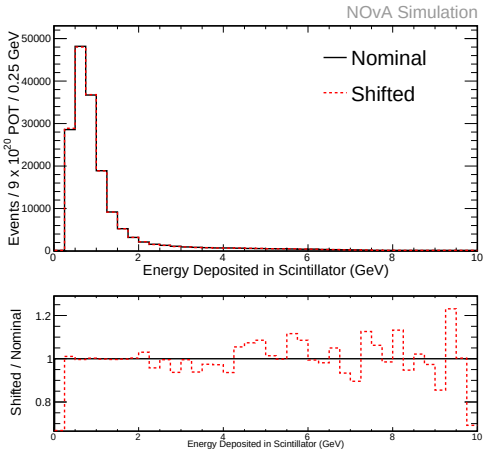

(b) ND simulated CC events

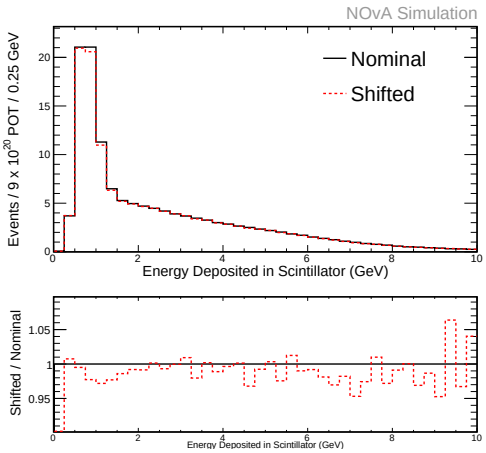

(c) FD simulated NC events

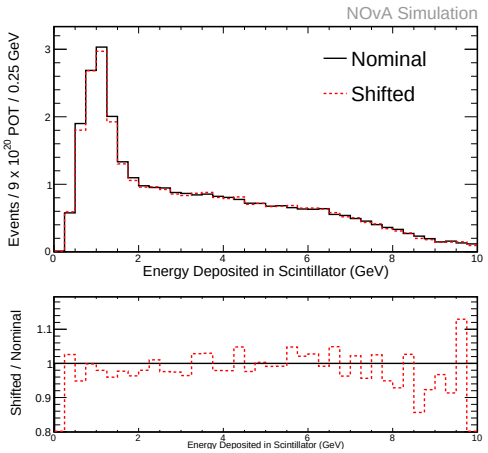

(d) FD simulated CC events

Figure 7.9: Method calibration systematic uncertainty in different samples. The ratio plot represents the number of shifted/nominal events in each bin.

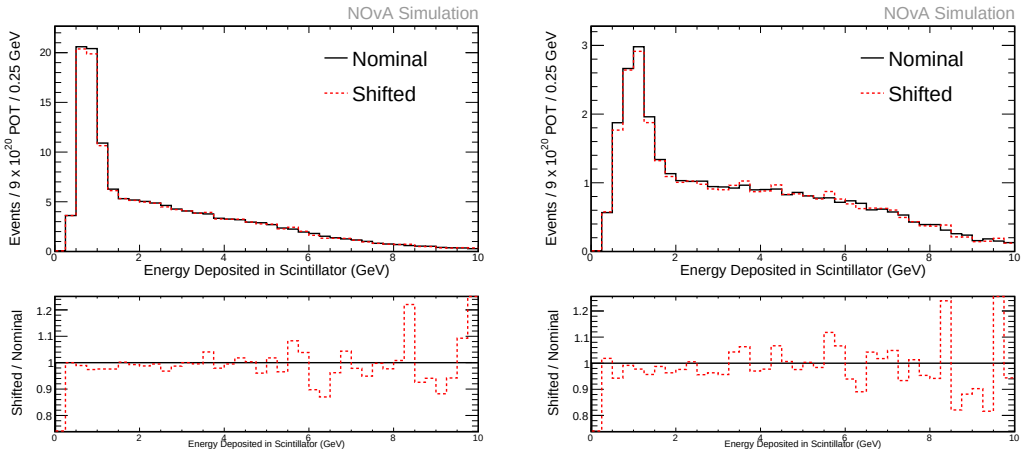

Figure 7.10: Method calibration systematic uncertainty in FD extrapolated prediction. Left plots are for NC distribution and right are for CC backgrounds.

7.2.5 ND Decomposition Systematics

In this analysis, there is an obvious mismatch between the data and MC in the ND. We are proportionally decomposing the ND data to get the FD MC prediction, which is then to be compared with the FD data. In the process of proportional decomposition, the ND data is decomposed into NC signal, ν_μ CC background, and ν_e CC background. This data is used to get the FD MC prediction. It is not well understood that which interaction type contributes to the observed data/MC difference. This should be considered as a systematic uncertainty. In this analysis, we have used the same method as we used in 2016 NC analysis, where the ND data/MC difference is assigned to NC or ν_μ at a time and then extrapolate them to the FD. The difference in the observed events at the FD between the nominal extrapolated prediction and this shifted prediction is taken as the systematic shift. The contribution of the systematic shift from ND NC assigned shift and ND ν_μ shift are added in quadrature to get a total systematic shift.

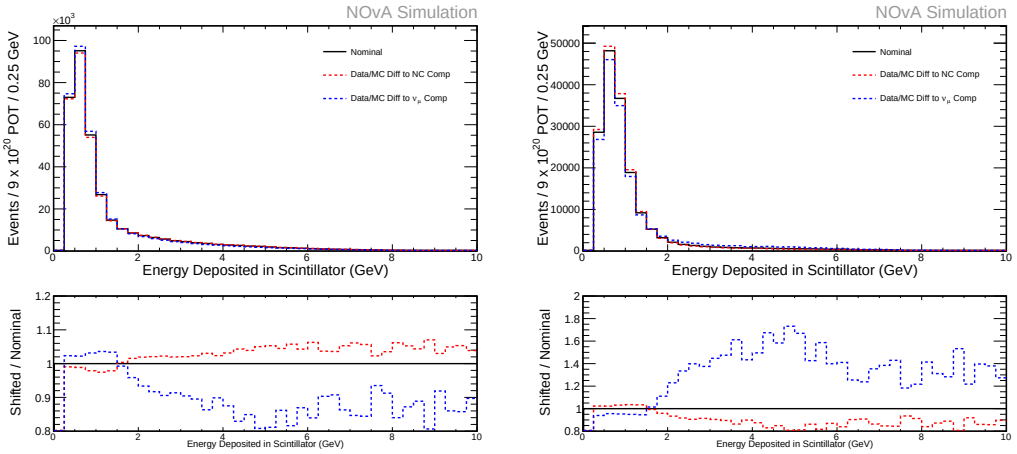

(a) ND simulated NC events

(b) ND simulated CC events

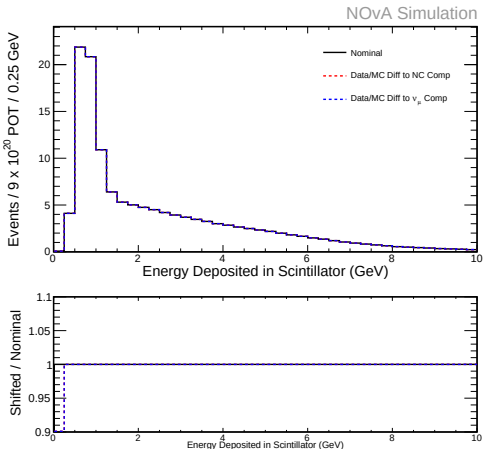

(c) FD simulated NC events

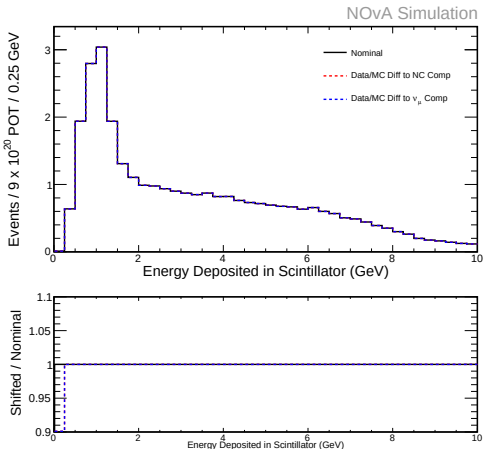

(d) FD simulated CC events

Figure 7.11: Decomposition systematic uncertainty in different samples. The ratio plot represents the number of shifted/nominal events in each bin.

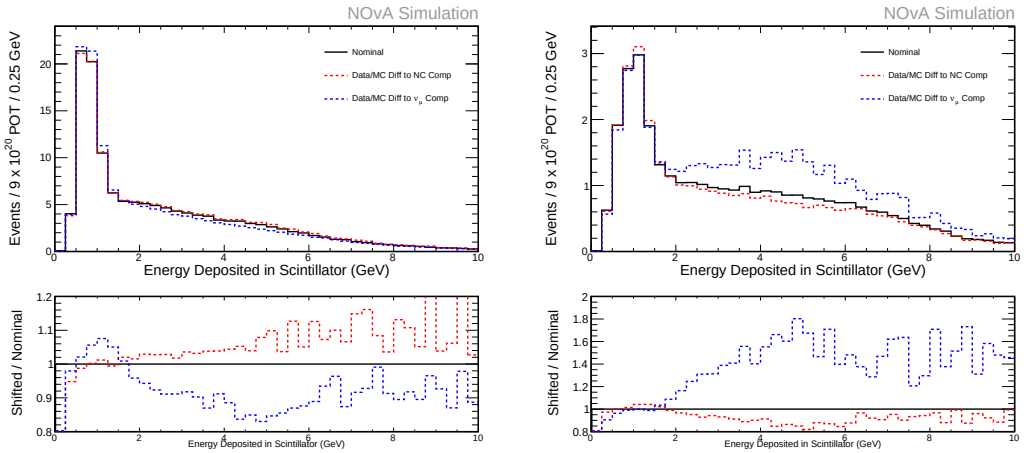

Figure 7.12: Decomposition systematics in the FD extrapolated sample. Left plots are for NC distribution and right are for CC backgrounds.

7.2.6 Acceptance Systematic Uncertainty

The NOvA detectors are placed at 14.6 mrad off the NuMI beam axis, and they are functionally identical. But the ND is small in size compared to the FD. The beam cone sweeps more and more area during its progress.

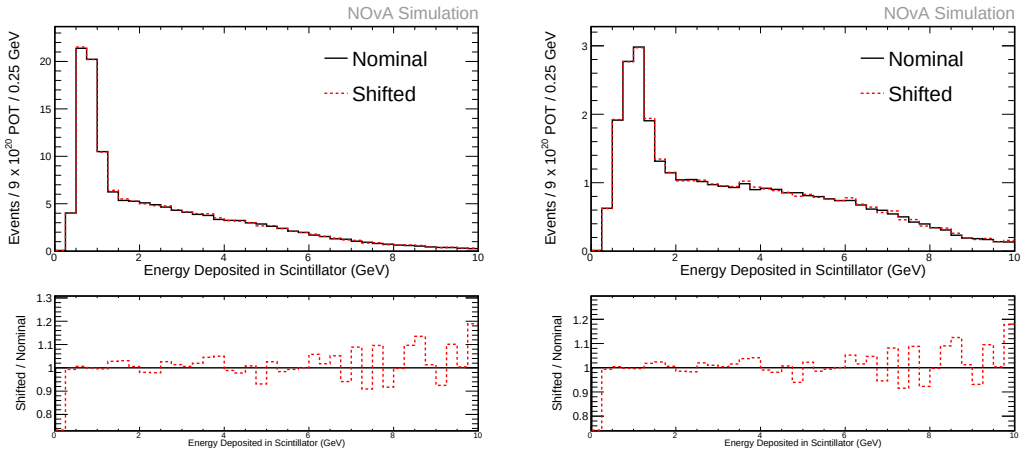

Figure 7.13: Acceptance systematics due to the first ND quadrant. Left plots are for NC distribution and right are for CC backgrounds.

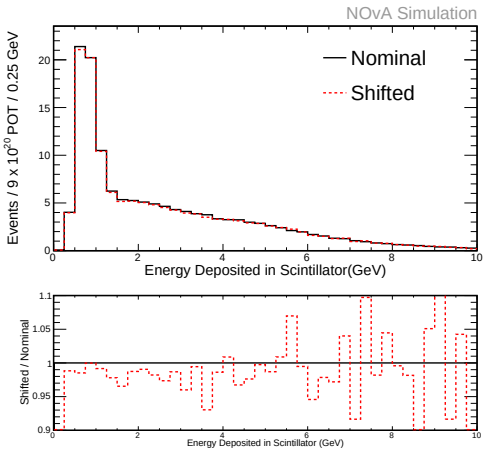

(a) second ND quadrant NC events

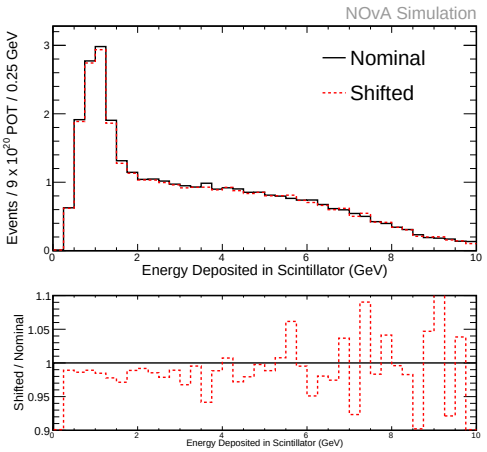

(b) second ND quadrant CC events

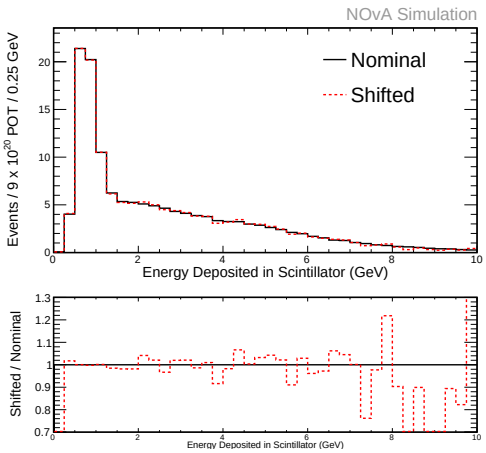

(c) third ND quadrant NC events

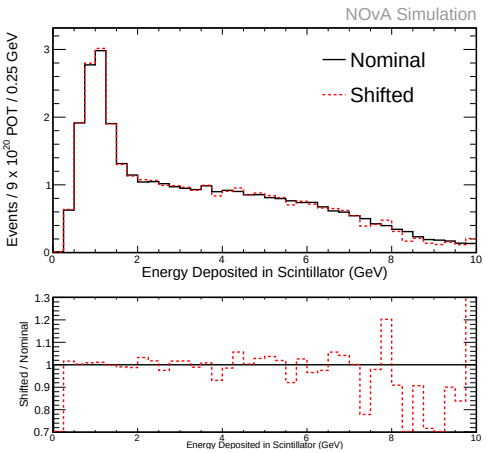

(d) third ND quadrant CC events

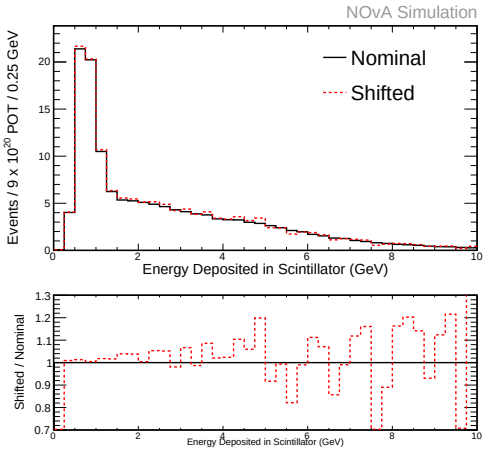

(e) fourth ND quadrant NC events

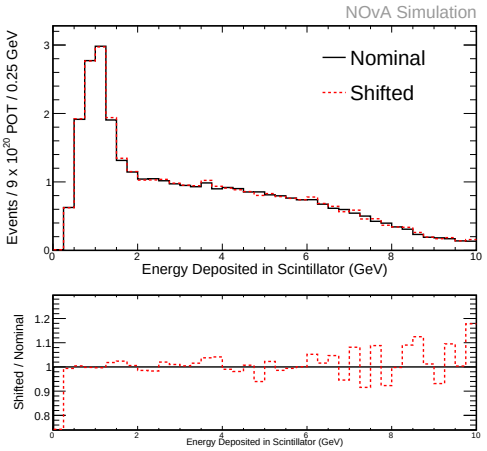

(f) fourth ND quadrant CC events

Figure 7.14: Acceptance systematic uncertainties.

So we should consider the uncertainty that arises due to the acceptance of the detectors. For this, we divide the ND into four regions; cut throw X and Z plane. We extrapolate each of these four ND spectra to FD separately to get the shifted FD extrapolated prediction. The systematic uncertainty is calculated by quantifying the difference between the nominal extrapolated prediction and extrapolated prediction from each of the four ND sections (see Figs. 7.13–7.14f).

7.2.7 Other Uncertainties

Three-flavor Oscillation Parameters

We include the uncertainty on the values of the three-flavor oscillation parameters not included in the fit as uncertainties. They have only a negligible effect on the signal but are large for the backgrounds. This is included as a normalization uncertainty based on the allowed range of signal and background by varying the three-flavor oscillation parameters within the PDG allowed uncertainties.

The Normalization Uncertainty

The normalization uncertainty includes contributions from the POT and the detector mass uncertainty. There is a 0.5% error on the POT counting. The mass uncertainty has been updated for the 2017 NOvA oscillation analyses and details are adapted from Ref. [118]. The new values are:

- FD: ±0.28%, dominated by PVC weighing.
- ND: ±0.28%, dominated by PVC lot variations.
- Muon Catcher: ±0.34%, dominated by PVC lot variations.
- FD/ND ratio: ±0.26%, strongly dominated by PVC lot variations.

Other Systematics Investigated

The rock event systematics – The ND fractional transverse momentum cut removes most of the ND selection sensitivity to the rock events. A 100% uncertainty was taken on the rock rate for 2016 summer analysis which was very conservative.

Category	Signal %	Background %
Genie	2.61	6.09
Acceptance	2.26	2.17
Beam	1.3	2.95
Calibration	8.97	7.91
Light level	2.12	1.54
MC Decomp	3.21	4.81

Table 7.1: The FHC systematics summary.

7.2.8 Summary of FHC Analysis Systematic Uncertainties

The total systematic uncertainty estimated in this analysis is lower than that of the 2016 summer analysis. The analysis improvements are paid off. Total systematic uncertainty values are NC 10.2% and CC 11.8%. Graphical representation of the systematic summary is shown in Fig. 7.16. Fig. 7.15 is the ND data/MC plot overlaid with the systematic band, where we can see that the ND data/MC disagreement is completely covered by the systematic band.

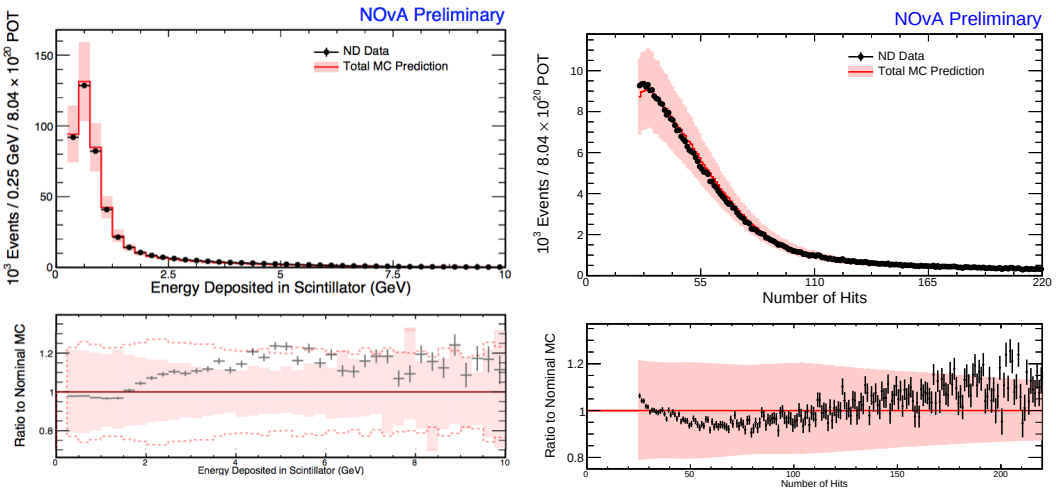

Figure 7.15: Total systematic uncertainty band in ND for the energy deposited in scintillator (left) and the number of hits(right).

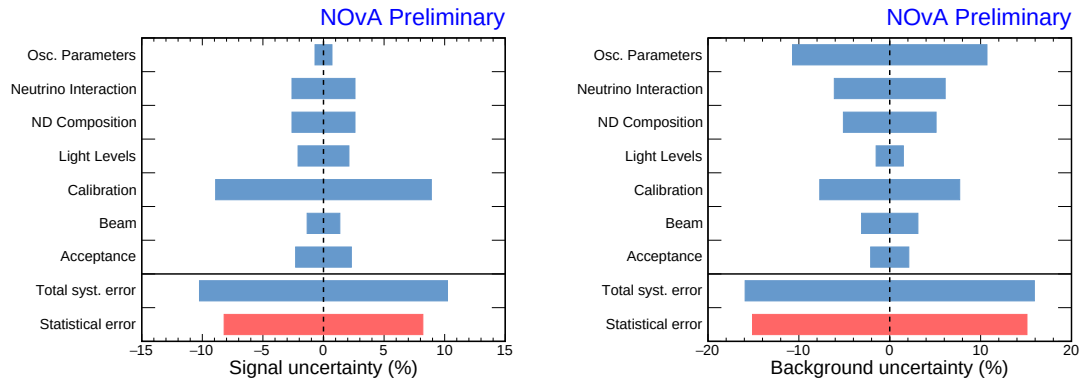

Figure 7.16: Systematics summary of 2017 FHC analysis.

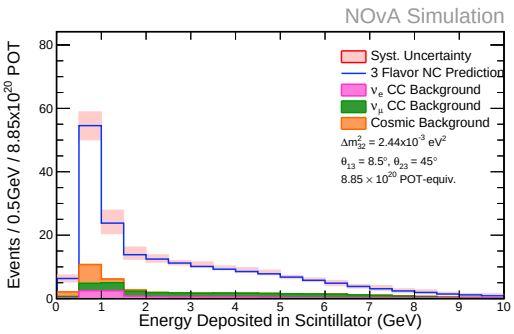

Figure 7.17: FD extrapolated prediction of neutrino events with the systematic band.

The FD extrapolated prediction with the systematic band is shown. The FD neutrino data fit to this spectrum. Events shown in 0.5 GeV energy bins.

7.3 Systematic Uncertainties of the RHC Analysis

The RHC systematic uncertainty estimation methods are very similar to those used for the 2017 FHC analysis. The 2019 RHC analysis retains the underlying simulation and calibration procedures of 2017 analysis. And

reconstruction changes are all incremental[2]. A cosmetic change in the 2017 RHC standard NOvA cross section tune is done as described in Ref. [119]. Some of the systematic uncertainties which we have estimated for the FHC analysis are dropped in this analysis. The ND decomposition, acceptance systematics, and the oscillation parameter systematics are dropped for this analysis. The decomposition systematics is dropped due to a much improved data/MC agreement. The acceptance systematics estimated is very low and can be safely dropped. Similarly, the oscillation parameter systematics is also dropped because our fitting procedure takes care of its effect. Also, the oscillation parameter effect on NC is very feeble. There are some new potential sources of systematic uncertainties in this analysis and are listed below:

1. **Neutron Uncertainty**
   Notably, for the RHC analysis, mismodeling of neutrons could warrant an additional uncertainty [120].

2. **Central Value Tune**
   An additional conservative systematic is included taking the full envelope of the NOvA cross section central value tune. This addresses the concerns that the NOvA cross section tune could be affecting our sensitivity to physics. The results of this analysis are only being interpreted in regions of phase space with no sterile signal, but this negligible uncertainty ensures no bias is included in the fits.

3. **Kaon Uncertainty**
   This analysis fits events in regions of the flux where the beam is dominated by kaons. Evidence from MINOS suggests that the kaon rate and uncertainties may be mismodeled. This 20% uncertainty addresses those concerns.

The other sources of systematics are the same as we have seen for the FHC analysis. Their quantification also follow the same procedure.

7.3.1 Summary of the RHC Systematic Uncertainties

The RHC analysis systematics strategy is similar to that of the 2017 analysis, with some of the additions mentioned above. Total systematic un-

[2]adding new information to the files

certainty of NC is 15.45 % and CC is 19.73 %. The summary plot of all systematics is shown in Fig. 7.19. Fig. 7.18 shows the ND data/MC plot with total systematic band. Here also, the data/MC discrepancy is completely covered by the estimated systematic band.

Category	Signal (NC) %	Background (CC)%
Beam	1.08	2.25
Calibration	13.77	9.15
Cross-section tune	0.32	1.96
GENIE	4.59	10.98
Light Level	4.89	3.84
Kaon	1.63	1.21
Neutron	0.49	0.21
Tau	0.00	12.69
Combined	15.45	19.73

Table 7.2: Summary of the RHC systematics.

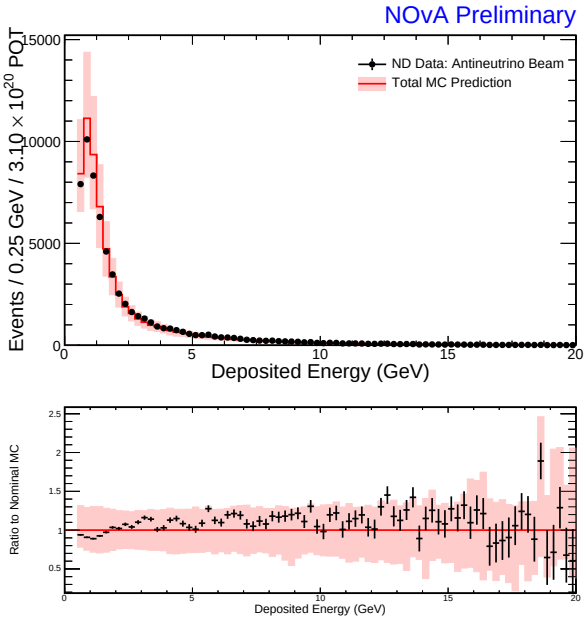

Figure 7.18: The ND data/MC distribution along with the total systematic uncertainty band.

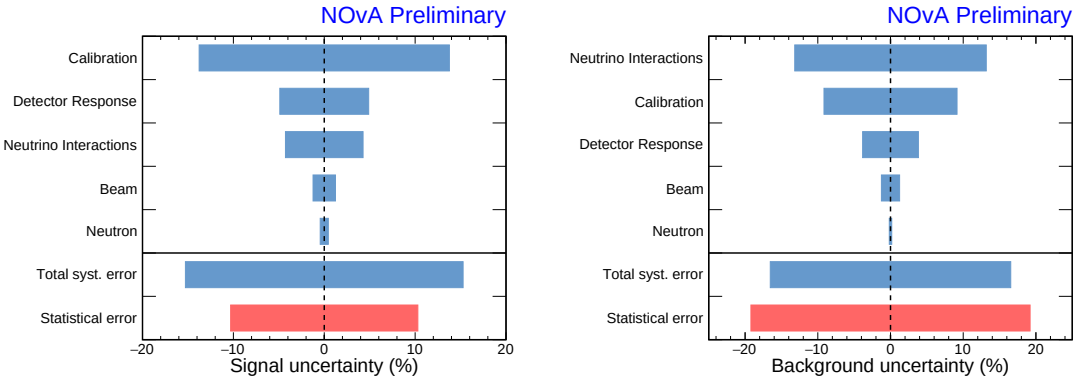

Figure 7.19: A graphical representation of the total systematic uncertainty.The systematic uncertainties on the signal events (right) and the background events (left) pertinent to the 2019 NC/sterile analysis. The size of the uncertainties is also shown alongside the total systematic and statistical errors.

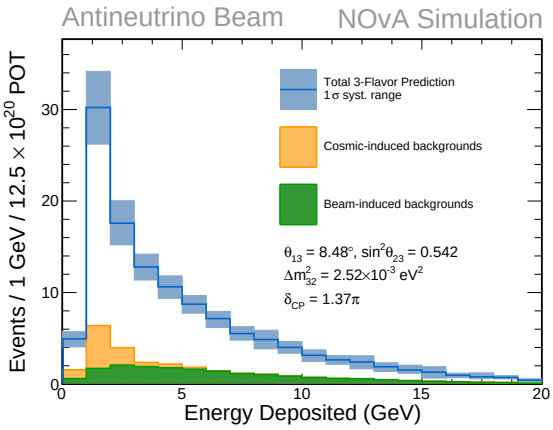

Figure 7.20: FD extrapolated prediction of antineutrino spectrum with systematic band.

8 Results

8.1 Introduction

The search for sterile neutrinos is the primary goal of NOvA's NC disappearance analysis. It has the potential to constrain the mixing of the three active neutrinos with a fourth sterile neutrino. This chapter summarizes the neutrino analysis with 8.85×10^{20} POT data and the antineutrino analysis with 12.5×10^{20} POT data. Since the potential light sterile neutrinos are more massive than the three active neutrinos, they undergo fast oscillation at the long baseline in NOvA and their average effect is seen as an overall depletion in the FD. For both of the analyses discussed in this thesis, the selected parametric region of the Δm^2_{41} is from 0.5 eV^2 to 5 eV^2. So, our analyses are unaffected by short-baseline sterile oscillations that may lead to the suppression of NC events in the ND. Both of these analyses are insensitive to the degenerate solution ($\Delta m^2_{41} \approx \Delta m^2_{32}$).

We will discuss the fitting and Feldman-Cousins (FC) technique (Ref. [121]) in the next section as the general strategy for both analyses. Then we will discuss the results of individual analyses.

8.2 The General Fitting Method

In this analysis, the experimental data is fit to the FD energy spectrum, in contrast to the method discussed in the 2016 PRD paper (Ref. [105]) which was a rate fit analysis. The shape of the predicted calorimetric energy spectrum is fit with the binned data. As we have seen, the calorimetric energy fitted in these analyses are corrected, as we have seen in Sec. 3.3. The predicted events are put in 250 MeV energy bins. In our analysis, binned data has high enough statistics that it is a Poisson distribution.

The Likelihood for the Poisson distribution can be represented as:

$$L(\hat{\eta}) = \prod_{i=1}^{N} \frac{\mu_i^{n_i}(\hat{\eta}) e^{-\mu_i(\hat{\eta})}}{n_i!}. \tag{8.1}$$

Here i represents a specific bin in a collection of total N number of bins, n_i is the number of events in ith bin, $\hat{\eta}$ is the set of tunable parameters and $\mu_i(\hat{\eta})$ is the average number of entries in the ith bin. Maximizing this function yields the maximum likelihood estimate and goodness of fit statistics. The standard likelihood ratio can be defined as:

$$\lambda(\hat{\eta}) = \frac{L(n;\hat{\eta})}{L(n;\mu)}. \tag{8.2}$$

Maximizing the likelihood ratio leads to a maximum likelihood. Here n is the observed number of events and μ is the predicted number of events that maximizes the likelihood function at the denominator of Eqn. 8.2. The log-likelihood function can be represented as:

$$\ln\lambda(\hat{\eta}) = \sum_{i=1}^{N} \left[n_i - \mu_i(\hat{\eta}) - n_i \ln\left(\frac{n_i}{\mu_i(\hat{\eta})} \right) \right]. \tag{8.3}$$

For sufficiently large statistics, $-2\ln\lambda(\hat{\eta})$ approaches a χ^2 distribution. In principle, we also have to consider the effect of systematics in the fit. We can include them in the fit as a vector of nuisance parameters $\hat{\epsilon}$, by adding a penalty term to the Eqn. 8.3. The log-likelihood function used in the NC disappearance analysis fit can be represented as

$$-2\ln\lambda(\hat{\eta},\hat{\epsilon}) = 2\sum_{i=1}^{N} \left[\mu_i(\hat{\eta},\hat{\epsilon}) - n_i + n_i \ln\left(\frac{n_i}{\mu_i(\hat{\eta},\hat{\epsilon})} \right) \right] + \sum_{i=1}^{M} \frac{\epsilon_i^2}{\sigma_i^2} + \left(\frac{\theta_{23} - \mu_{23}}{\sigma_{23}} \right)^2 \tag{8.4}$$

For simplicity, in the following discussion, we will use χ^2 to represent the $-2ln\lambda(\hat{\eta})$, but always the Poisson likelihood will be used. The 2nd term in right hand side of Eqn. 8.4 is penalty term for M systematic errors, where σ_i is the variance and ϵ_i is the fitted value for ith systematic error. The 3rd term in right side of Eqn. 8.4 adds a penalty term for the Gaussian constraint applied for θ_{23} with mean μ_{23} and variance σ_{23} The best fit value can be found by minimizing the χ^2. By the help of this best fit value, the $\Delta\chi^2$ value can be found out for each set of oscillation parameters.

8.3 Feldman-Cousins Correction

In the parameter estimation process, the correct values of the parameters can be estimated by minimizing the χ^2 function. We need to have a test static in order to state what is the significance of rejecting the possibility that other values of parameters are true. The test static, $\Delta\chi^2$ can be used to create confidence intervals:

$$\Delta\chi^2 = \chi^2(\hat{\theta}) - \chi^2(\hat{\theta}_{\text{BestFit}}) \tag{8.5}$$

here $\hat{\theta}$ is the set of oscillation parameters.

Under a Gaussian scenario, $\Delta\chi^2$ converges to χ^2_k, where k is the degrees of freedom. Also the σ can be viewed as $\sigma = \sqrt{(\Delta\chi^2)}$. The χ^2 function is used to determine the goodness of fit. As repeated trials may give different χ^2, we have to determine the probability of finding a χ^2. The "p-value" gives the probability of finding a specific value of χ^2 at least as large as one we measure. The value of the test static at a given p-value is known as the critical value. Now a significance in terms of the critical value of a standard normal distribution can be created.

But in reality it cannot always be possible to approximate to a χ^2. In neutrino physics experiments the data statistics are low and the parameters are not sufficiently away from a physical boundary. So the Wilks' theorem (Ref. [122]) fails and the $\Delta\chi^2$ cannot be approximated as χ^2. So, the advantage of finding significance directly from the test static is lost. The confidence intervals extracted from the Gaussian χ^2 surface do not necessarily cover the true significance of the estimated parameters. We should get a $\Delta\chi^2$ function to extract the confidence intervals with correctly covered true values of the oscillation parameters. The FC technique is developed to circumvent this and all the NOvA oscillation analysis results are FC corrected. The FC technique is an empirical technique used to interpret a $\Delta\chi^2$ value into a correct rejection probability. We are creating a true $\Delta\chi^2$ distribution, from which we can extract the p-value and thus the significance. The steps of FC correction are summarized below and the results are shown in Fig. 8.1.

1. We generate the Poisson fluctuated data (pseudo-experiments) at each point in parameter space (θ_{24} and θ_{34}), with assuming other parameters (Δm^2_{32}, θ_{23} and θ_{13}) are Gaussian sampled with 1σ of

their mean values.

2. For each pseudo-experiment, we perform two fits to the predicted spectrum, i.e.
   - First one is designed to get the global best fit (χ^2_{gbf} while all the variables are kept floated in the fit).
   - For finding χ^2_{true}, θ_{24} and θ_{34} are kept fixed and fits only other parameters (Δm^2_{32}, θ_{23} and θ_{13}).
3. From this, we can find the ($\Delta\chi^2 = \chi^2_{\text{true}} - \chi^2_{\text{gbf}}$).
4. We then find the proportion of the pseudo-experiments above the observed $\Delta\chi^2$.
5. The p-value and corresponding significance can be calculated from it.

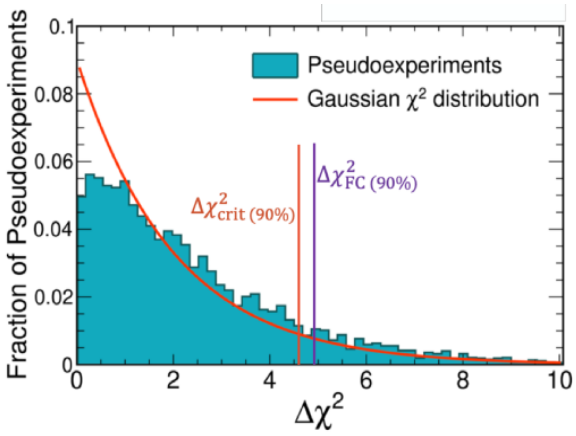

Figure 8.1: Empirical $\Delta\chi^2$ distribution compared with the predicted $\Delta\chi^2$ with two degree of freedom, considering errors are Gaussian. The $\Delta\chi^2_{\text{crit}}$ is the critical value of 4.61 that corresponds to the 90% C.L. for a χ^2 distribution with two degrees of freedom. This is compared to the $\Delta\chi^2_{FC}$ value up to which 90% of pseudo-experiments are included. This Fig. is adapted from Ref. [123]

8.4 Results

The NOvA experiment makes use of an analysis strategy called blinding. Blinding actually masks the neutrino events in the FD files, that fall in the NuMI spill time window (the time window in which the neutrino interactions happen at the detector due to the neutrinos/antineutrinos comes from the NuMI beam). The experiment looks at the data spectrum only after freezing all the analysis components including the event selection, systematics and cross section tuning of MC, and after acquiring permission from the collaboration.

8.5 The FHC Analysis

This analysis is an updated version of the analysis mentioned in the PRD paper (Ref. [105]). The improvements are in cosmic rejection (Sec. 5.1.5), cross section modeling, detector modeling, and NC selection efficiency was also improved. A single parameter correction is done on the slice calorimetric energy, as discussed in Sec. 3.3. We have continued to use the same extrapolation method to predict the FD energy spectrum in this analysis. The three-flavor oscillation parameters used in this analysis are listed in Table 5.1 The deliverables of this analysis are similar to that of the 2016 analysis. They are:

- The ND and FD visible energy spectra and the number of events that qualify the NC selection criteria compared with the three-flavor prediction.
- A sterile model-independent comparison between the number of NC events measured at the FD and the number of events predicted by the three-flavor model, done in terms of the R statistic defined by,

$$R^{E}_{\mathrm{NC}} = \frac{N_{\mathrm{Dat}} - \sum \mathrm{BG}}{S_{\mathrm{NC}}} \tag{8.6}$$

  The R statistic is defined in a specific energy range in the spectrum denoted by superscript E, N is the number of data events is qualified as NC events, $\sum \mathrm{BG}$ is the total predicted background (that includes CC events misidentified as NC events and cosmic events), and S_{NC} is the number of NC events predicted.

- 90% C.L. 2D contours for θ_{24} and θ_{34}
- 90% C.L. 2D contours on $|U_{\mu 4}|^2$ and $|U_{\tau 4}|^2$ The angles θ_{24} and θ_{34} can be translated to $|U_{\mu 4}|^2$ and $|U_{\tau 4}|^2$ using the relations,

$$|U_{\mu 4}|^2 = \cos 2\theta_{14} \sin 2\theta_{24}, \tag{8.7}$$

$$|U_{\tau 4}|^2 = \cos 2\theta_{14} \cos 2\theta_{24} \sin 2\theta_{34} \tag{8.8}$$

  This analysis is not sensitive to θ_{14} and also using the reactor experimental limits [124] we can safely assume θ_{14} is small ($\cos 2\theta_{14} \approx 1$)

The main contribution of this analysis will be the limits on θ_{34} and $|U_{\tau 4}|^2$ that are fairly unconstrained.
The analysis predicted 191.96±13.82(stat.)±21.99(syst.) events at FD and 214 events are observed in the neutrino data. The figure 8.2 shows the data/MC distribution of the Energy Deposited in the Scintillator.

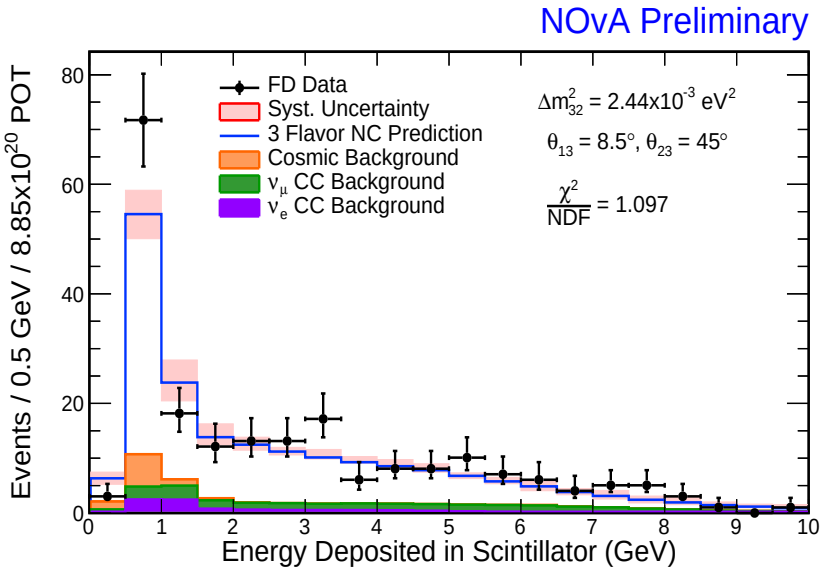

Figure 8.2: Energy Deposited in Scintillator distribution of events which pass the NC selection. 214 data events are observed while the predicted events are 191.2 ± 13.8 (stat.)± 22.0(syst.). The MC matches data runs, and a POT of 8.85×10^{20}.

The Fig. 8.2 is a stack plot for FD with 0.5 GeV energy binning. The analysis region is ranging from 0.5 GeV to 10 GeV. It has a total χ^2 value of 21.93 and the number of degrees of freedom (NDF) equals to 20, this gives $\chi^2/NDF = 1.097$. The oscillation parameters used are shown in the plot. Figs. 8.3 to 8.8 show the FD data/MC distribution for different variables used for the event selection. All plots show reasonable data/MC agreement.

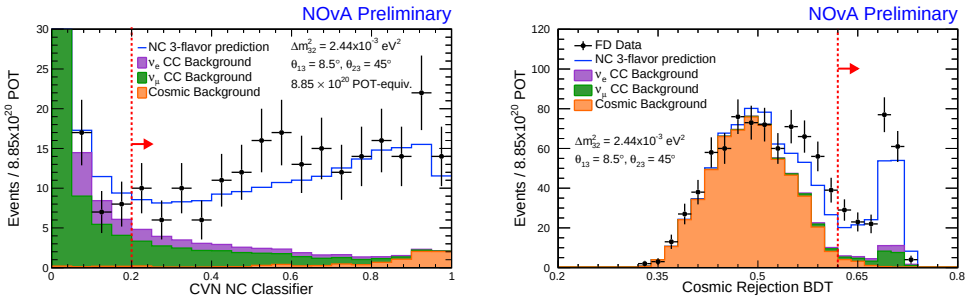

Figure 8.3: Left stack plot is the data/MC comparison plot for the NC cosmic Rejection BDT distribution. The right plot is CVN distribution at FD. The event distribution at the FD that passes through the complete selection process, excluding the cut on the plotting variable. MC is matched to the data run and is 8.85×10^{20} POT.

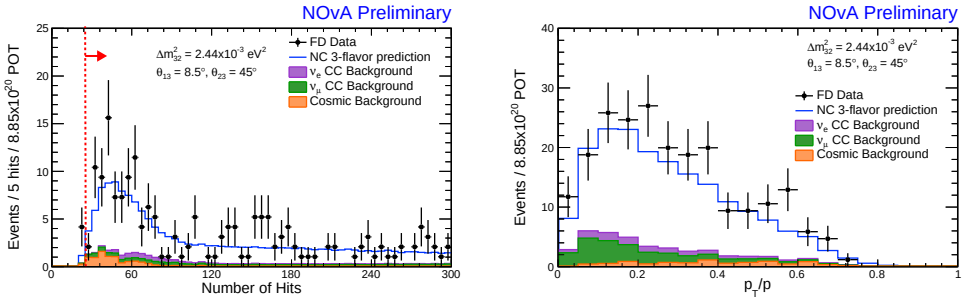

Figure 8.4: Left stack plot is the data/MC comparison plot for the number of hits distribution. Right plot is the transverse momentum fraction. The event distribution at the FD that passes through the complete selection process, excluding the cut on the plotting variable.

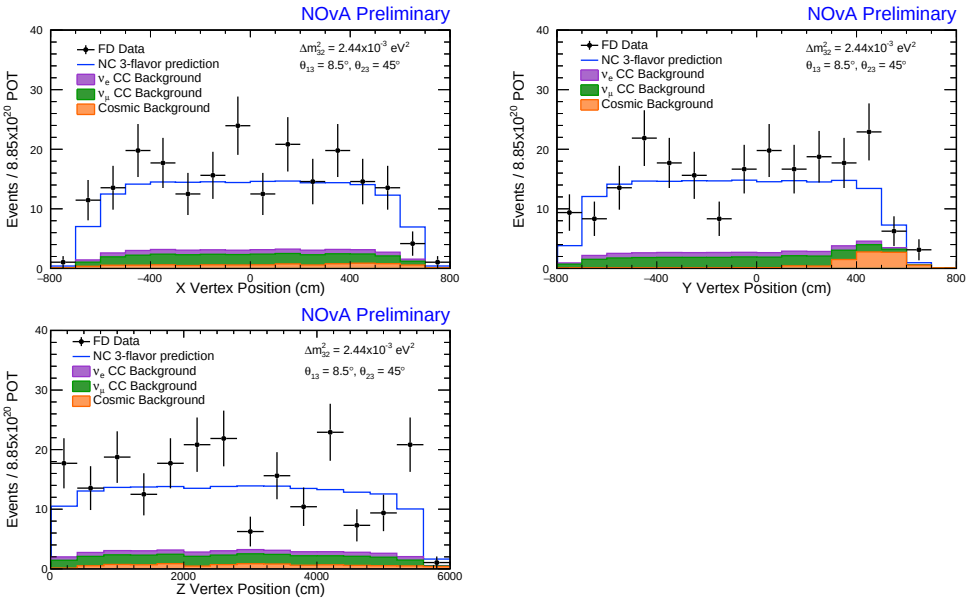

Figure 8.5: These are the data/MC comparison plot for the event vertex at the FD. The event distribution at the FD that passes through the complete selection process, excluding a cut on the plotting variable.

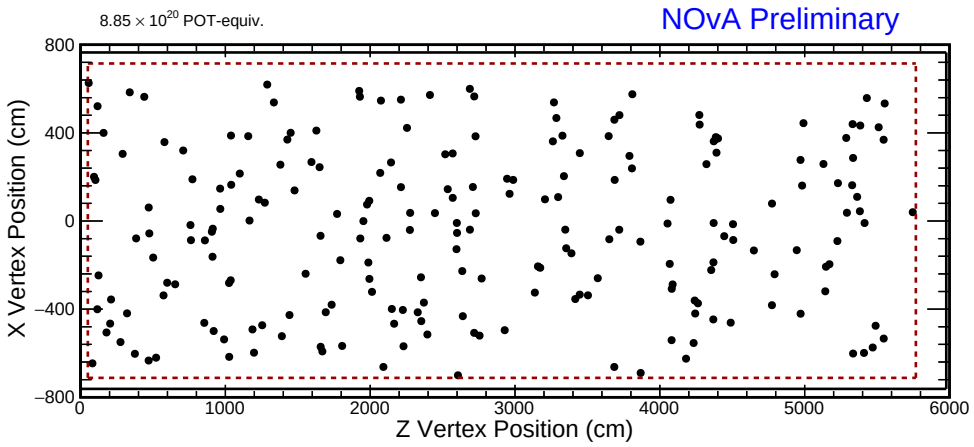

Figure 8.6: These are the data event vertex distribution in XZ plane. The dotted line boundary shows the selection area in the detector.

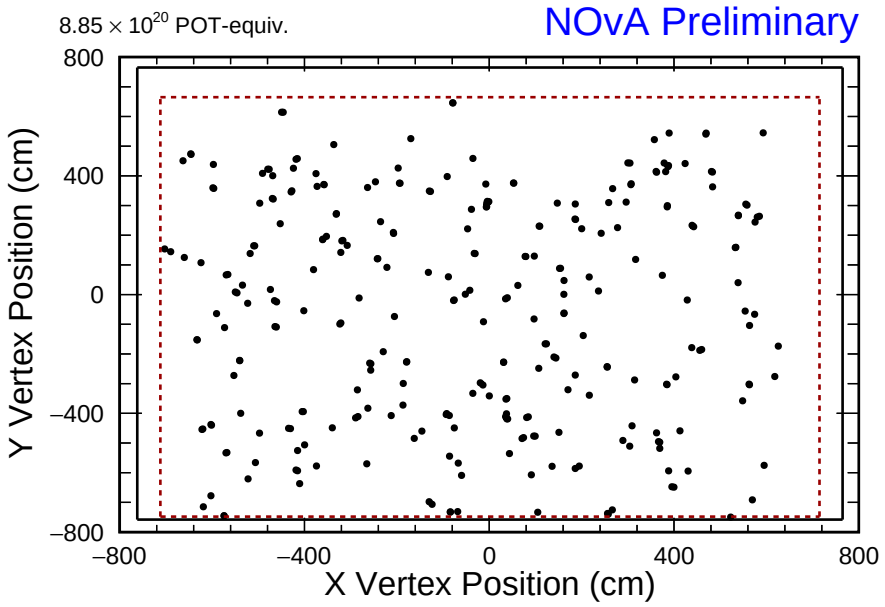

Figure 8.7: These are the data event vertex distribution in XY plane. The dotted line boundary shows the selection area in the detector.

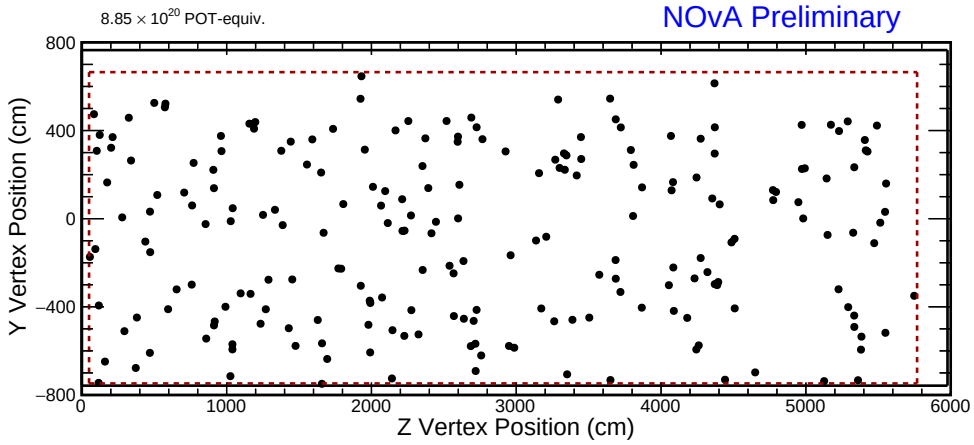

Figure 8.8: These are the data event vertex distribution in YZ plane. The dotted line boundary shows the selection area in the detector.

8.5.1 R-ratio

The R-ratio is a model independent measure of NC disappearance. When R-ratio =1, this leads to the conclusion that there is no NC disappearance. Here the R-ratio is calculated within different energy ranges. The R-ratio is calculated for 0-2.5 GeV and for 2.5-5 GeV ranges. The R-ratio is calculated using Eqn. 8.6 and the values are summarized in Table 8.1.

Item	0-2.5 GeV	2.5-10 GeV	0-10 GeV
R-ratio	$1.19 \pm 0.14 \pm 0.12$	$1.08 \pm 0.14 \pm 0.12$	$1.15 \pm 0.14 \pm 0.12$
Observed events	119	95	224

Table 8.1: The R-ratio and number of events observed. In 2016 analysis, the R-ratio calculated was 1.19 ± 0.16(stat.) $\pm$ 0.10(syst.)

The result is consistent with the null hypothesis of active-sterile mixing. Next section we will see how the sterile mixing angles can be constrained in the parameter space.

8.5.2 Fitting the FHC Data

The fitting is performed on the spectrum with 0.25 GeV binned data. Fig. 8.2 is shown with 0.5 GeV binning just for better visibility. The region that is fitted is limited from 0.5 GeV at the lower end to 10 GeV at the higher end. The 0.5 GeV cut is designed to remove the region with higher threshold effect. Since only 2 events are seen after 10 GeV, it is safe to limit the analysis region up to this.

When the fitting is performed, some parameters are kept floating, some are set to zero while some others are frozen to be at their current best fit values. The angles θ_{24} and θ_{34} are allowed to float between angles 0° and 45°, while the θ_{23} is kept same as that used in 2016 analysis [105] (allowed to float with a small Gaussian constraint with mean 45.8° and 3.2° standard deviation). Other three-flavor parameters are fixed at the values listed in Table 5.1. θ_{14} is taken as zero, referring to the reactor experimental results. The parameters δ_{24} is profiled over. FC correction (discussed in Sec. 8.3) is applied and a final corrected contour is produced.

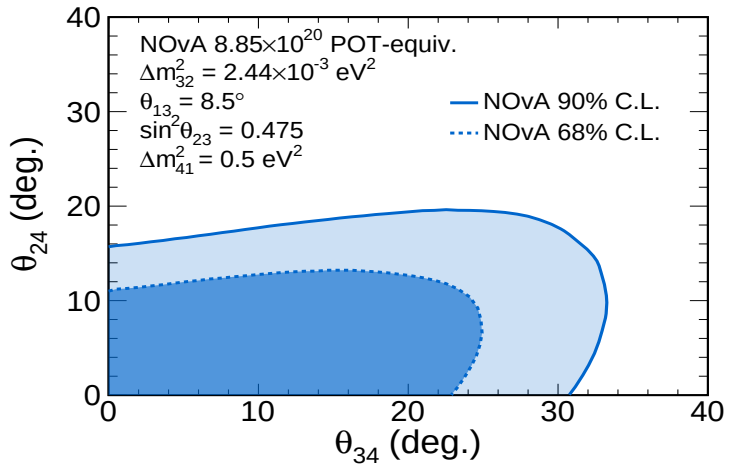

Figure 8.9: Feldman-Cousins corrected 2D non-excluded regions (shaded) at 68% C.L. and 90% C.L. in terms of sterile mixing angle θ_{24} and θ_{34} in the 3+1 model.We set limits of $\theta_{24} < 19.7°$ and $\theta_{34} < 32.6°$ at 90% C.L.

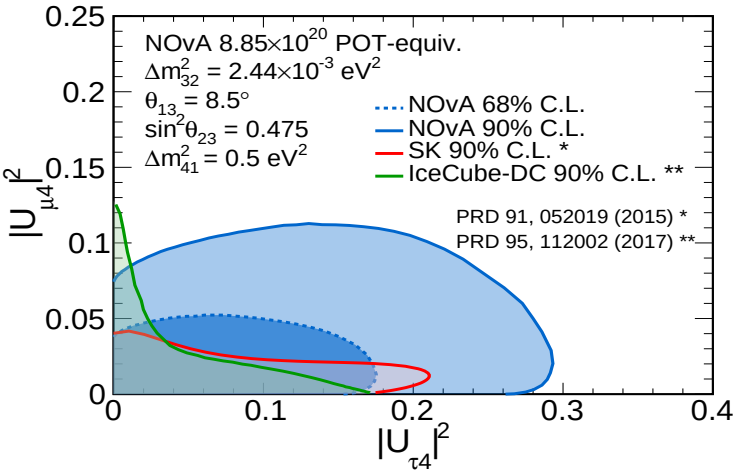

Figure 8.10: Feldman-Cousins corrected 2D non excluded regions (shaded) at 68% C.L. and 90% C.L. in terms of $|U_{\mu 4}|^2$ and $|U_{\tau 4}|^2$ where we assume $\cos^2(\theta_{14}) = 1$. For an exposure of 8.85×10^{20} POT, we set limits of $|U_{\mu 4}|^2 < 0.114$ and $|U_{\mu 4}|^2 < 0.287$ at 90% C.L. Includes a comparison to the SuperK and IceCube-DeepCore results.

8.6 The RHC Analysis

The RHC analysis (antineutrino beam analysis) is conducted with 12.5×10^{10} POT of antineutrino data. Similar to neutrino beam analysis, this analysis also limited to the region 0.05 eV^2 to 0.5 eV^2 in Δm^2_{41}. which is the region of the parameter space where there is no ND sterile oscillation. So the ND-FD extrapolation method is safely applied here. The result of this analysis is supposed to be the very first antineutrino long-baseline NC disappearance result. The analysis predicted 122±11(stat.)±18(syst.) events at FD and 121 events are observed in the antineutrino data. The whole range of variables used in the selection cuts are shown in Figs. 8.12 to 8.17. The three-flavor oscillation parameters used in this analysis are listed in Table 5.15.

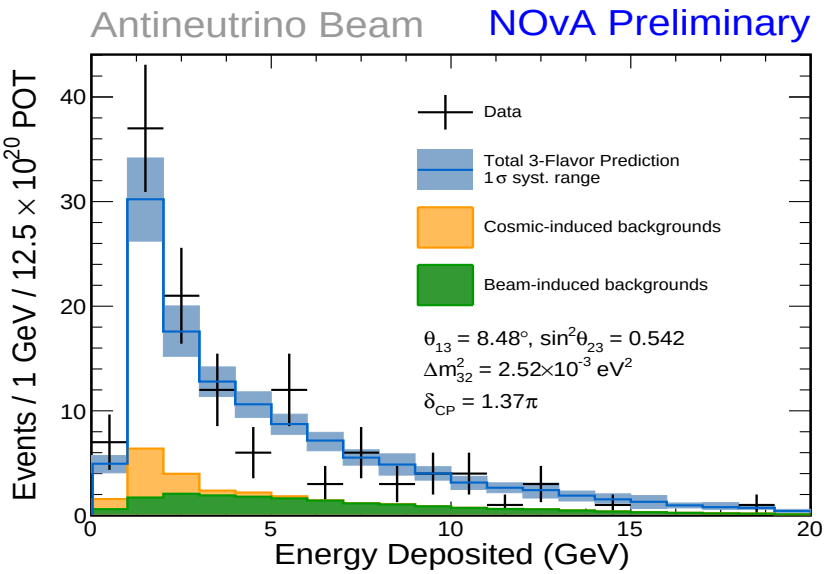

Figure 8.11: The spectrum of the FD events selected by all cuts. The total systematic uncertainty is represented by the blue band. Background from the beam (CC events) and cosmics are shown as a stacked plot. Events are arranged in the 1 GeV energy bins. It have a χ^2/NDF value = 1.04

.

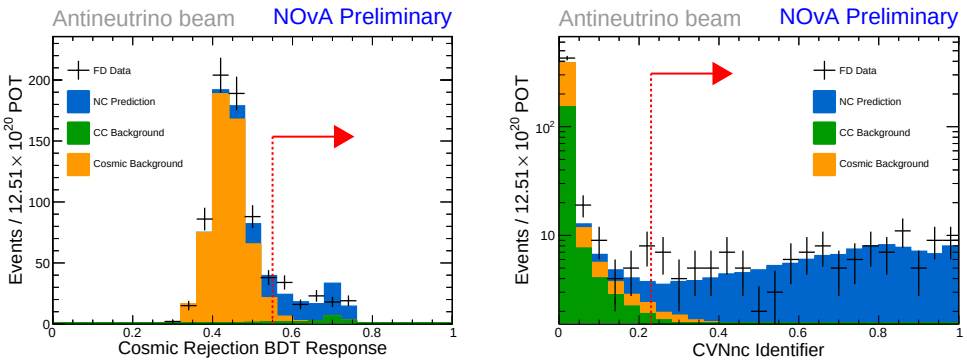

Figure 8.12: Left stack plot is the data/MC comparison plot for the NC Cosmic Rejection BDT distribution. Right plot is CVN distribution at FD. The event distribution at the FD that passes through the complete selection process, excluding the cut on the plotting variable.

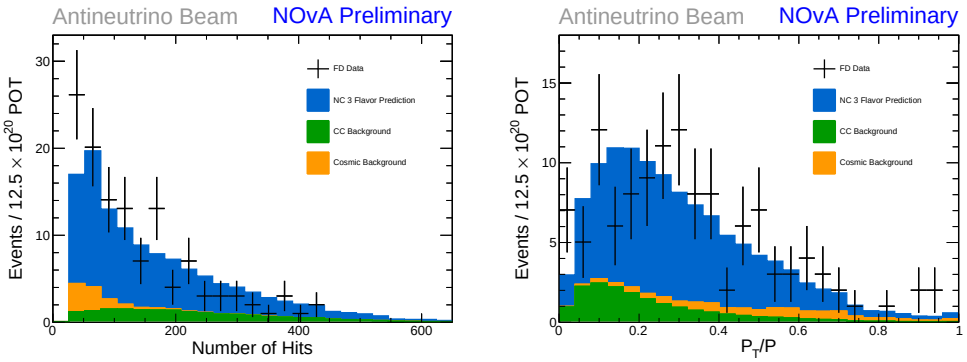

Figure 8.13: The left stack plot is the data/MC comparison of the number of hits variable. The right plot is the transverse momentum fraction. The event distribution at the FD that passes through the complete selection process, excluding the cut on the plotting variable.

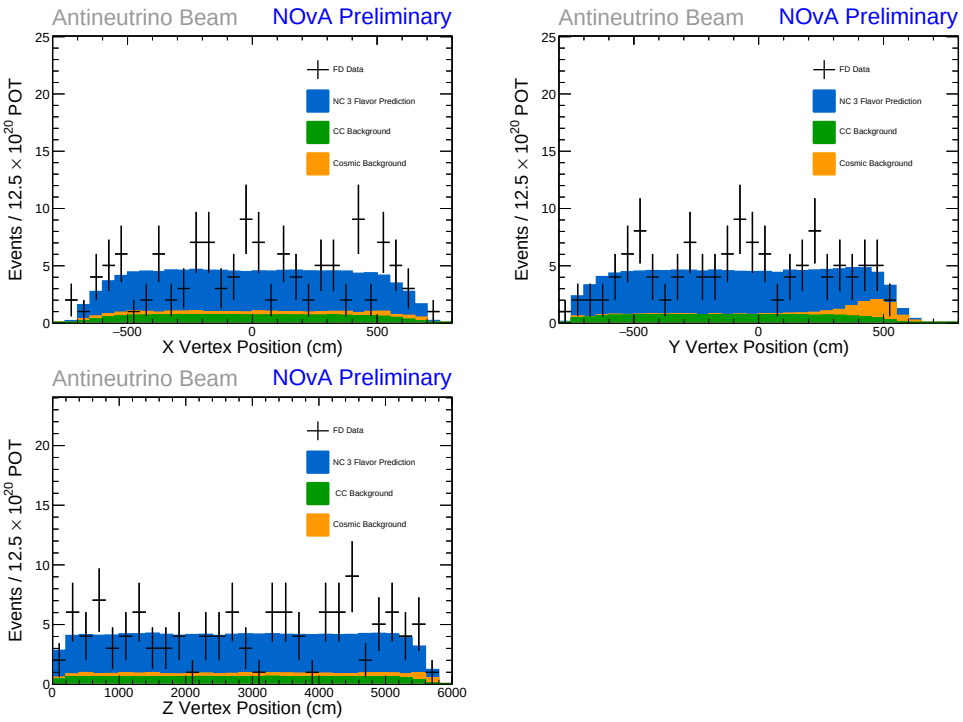

Figure 8.14: These are the data/MC comparison plot for the event vertex at the FD. The event distribution at the FD that passes through the complete selection process, excluding the cut on the plotting variable.

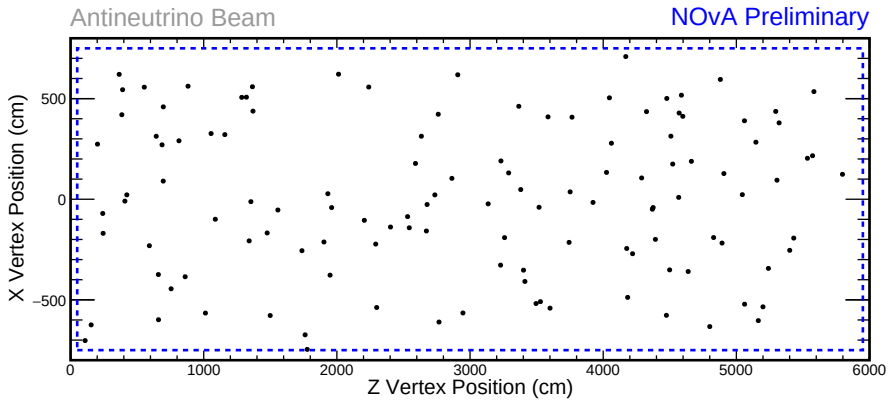

Figure 8.15: These are the data event vertex distribution in XZ plane. The dotted line boundary shows the selection area in the detector.

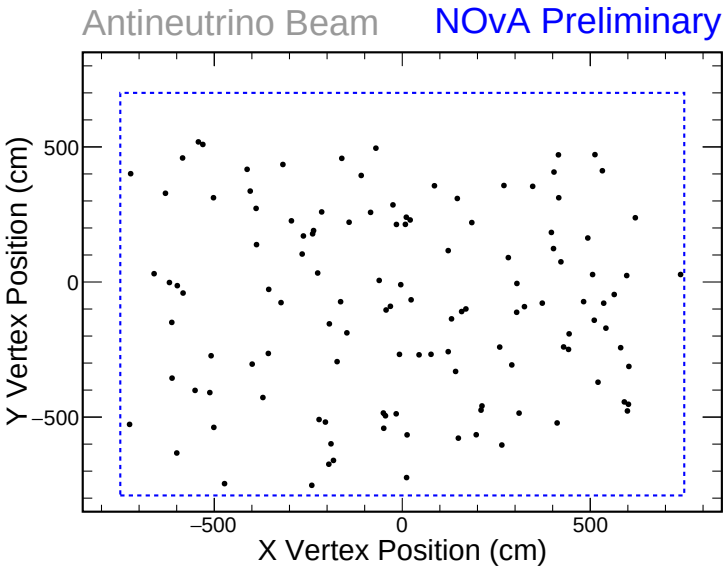

Figure 8.16: These are the data event vertex distribution in XY plane. The dotted line boundary shows the selection area in the detector.

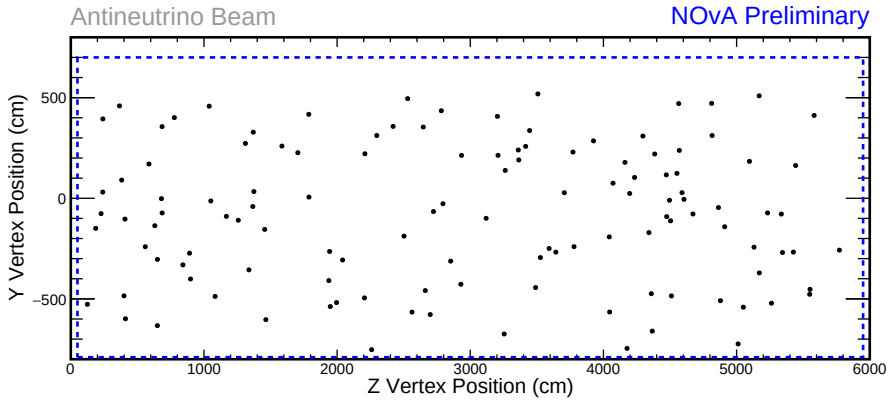

Figure 8.17: These are the data event vertex distribution in YZ plane. The dotted line boundary shows the selection area in the detector.

8.6.1 *R*-ratio

Similar to previous FHC analyses, a model independent *R*-ratio is calculated to test the NC disappearance hypothesis. We use Eqn. 8.5.1 to

calculate R-ratio. The R-ratio obtained is 0.99±0.12(stat.)±0.16(syst.) which is consistent with the three-flavor hypothesis.

Item	2016 FHC	2017 FHC	2019 RHC
R-ratio	$1.19 \pm 0.16 \pm 0.10$	$1.15 \pm 0.14 \pm 0.12$	$0.99 \pm 0.12 \pm 0.16$

Table 8.2: The R-ratio in different long-baseline NC disappearance analyses in NOvA.

8.6.2 Fitting and FC Correction

The mixing angle θ_{14} has been constrained to be small by reactor experiments. The latest global analysis in Ref. [125] fits an upper bound of $\sin^2\theta_{14} = 0.0089$ ($\theta_{14} \leq 5.4°$) after fitting to all reactor data. We set $\cos 2\theta_{14} = 1, (\theta_{14} = 0)$ for fitting purposes. We apply a loose Gaussian constraint for θ_{23} under which it can float (within 1σ range) in the fits centered at the PDG best fit [36]. As the phase δ_{24} has an effect at the FD, we profile over δ_{24} in the fit. The FC correction is done on the θ_{24} vs θ_{34} surface (shown in Fig. 8.18). The process is same as discussed in Sec. 8.3.

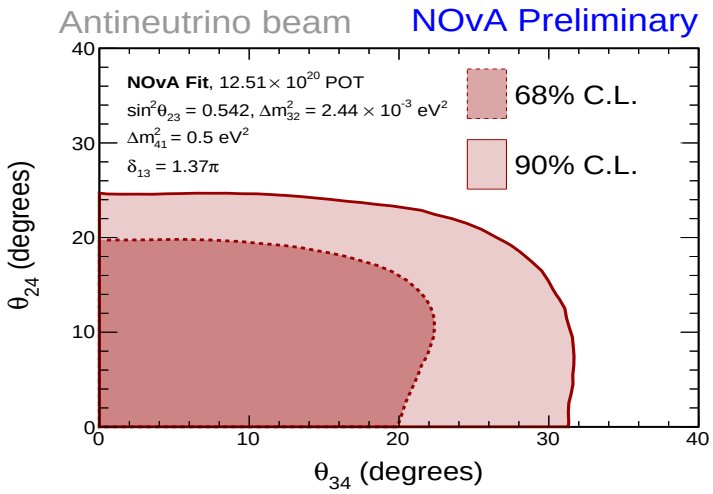

Figure 8.18: Sensitivity of the NC-selected FD data within a 3+1 sterile oscillation framework. The FC corrected 68% C.L. and 90% C.L. contours are shown (the non-excluded region is shaded).

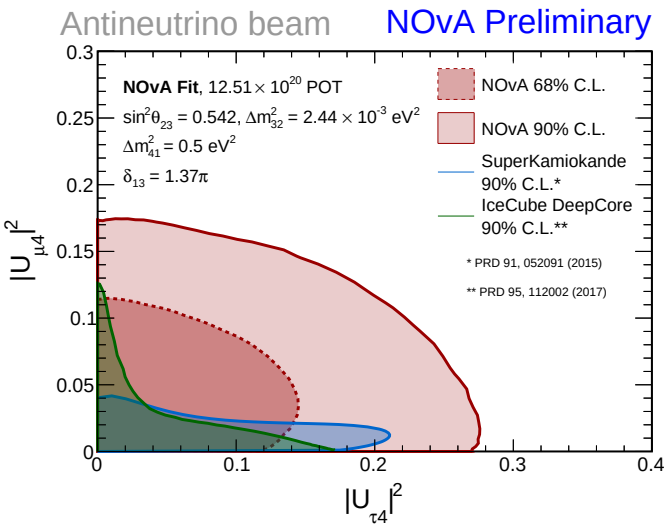

Figure 8.19: $|U_{\mu 4}|^2$ vs $|U_{\tau 4}|^2$ 2D non-excluded region of NOvA overlaid with the SuperK and IceCube-DeepCore regions.

The FHC and RHC results can be compared with the global limits. This is shown in Table 8.3.

Experiment	θ_{24} (in degree)	θ_{34} (in degree)	$\lvert U_{\mu 4}\rvert^2$	$\lvert U_{\tau 4}\rvert^2$
NOvA RHC 2019 (Accelerator $\overline{\nu}$)	24.7	31.7	0.175	0.276
NOvA FHC 2017 (Accelerator ν)	16.2	29.8	0.078	0.247
NOvA FHC 2016 (Accelerator ν)	20.8	31.2	0.126	0.268
MINOS/MINOS+ (Accelerator ν)	4.4	23.6	0.006	0.160
SuperK (atmospheric)	11.7	25.1	0.041	0.180
IceCube(atmospheric)	4.1	-	0.005	-
IceCube-DeepCore (atmospheric)	19.4	22.8	0.11	0.150

Table 8.3: Limits at fixed Δm^2_{41}. The Δm^2_{41} for NOvA, MINOS/MINOS+ [73], IceCube [126] and SuperK [127] are fixed at 0.5 eV^2 while DeepCore [128] is at 1 eV^2.

9

Future Improvements and Conclusion

9.1 Future Improvements

The more data we have in an experiment, the stronger the parameter constraints we can set. Since just $\approx 50\%$ of planned exposure is reached till now, NOvA has the potential to produce a tight limit on the sterile mixing angles θ_{24} and θ_{34}, and also mixing matrix elements $|U_{\mu 4}|$ and $|U_{\tau 4}|$ that will be highly competitive with the results from other experiments such as T2K and MINOS/MINOS+. The improvements in the interaction cross section are another area where there is plenty of space to improve. The high energy tail end of the neutrino energy spectrum shown in Fig. 8.2 is dominated by the inelastic collision where most of the event energy is lost as hadronic showers. Improved cross section modeling will reduce the data/MC discrepancy. The two analyses discussed in this thesis implemented only a single parameter fit to estimate NC event energy. This does not take into account the energy carried away by the outgoing neutrino. Improvement in the NC event energy estimation is difficult but promising. Work is going on to train a CVN that reject cosmic energy deposition in the detector. The better cosmic rejection will improve the analysis.

The existence of sterile neutrinos will distort both the ND and the FD NC energy spectra, with the size and energy region, affected dependent on the mixing angles mainly θ_{24} and θ_{34} and the mass of the sterile neutrino, Δm^2_{41}. For the analyses discussed in this thesis, we have limited our results in Δm^2_{41} to a range where no distortion of the ND spectra is predicted. This limits the region of the Δm^2_{41} parameter space where we can search for the sterile neutrino. Therefore, to maximize our sensitivity across a wide Δm^2_{41} range, we have to use a different method, such as the covariance matrix method that enables a ND-FD joint-fit analysis. This has the potential to search for the sterile neutrinos across a wide Δm^2_{41} range. An analysis is underway that performs the ND-FD joint fit which is expected to further squeeze the probable hiding places of sterile

neutrinos in the Δm^2_{41} parameter space. The longer term plan is a full joint fit that fit for the NC, ν_e and ν_μ spectra in both ND and FD simultaneously.

9.2 Conclusion

The 2017 FHC NC disappearance analysis is an updated version of the 2016 analysis [105] with 50% more data and improvements such as moving from a rate fit to rate plus shape fit analysis, better cross section models, detector modeling, a new NC energy estimator, a new PID for cosmic rejection, CVN improvements, updated estimation of systematics. Reasonable agreement between data and MC has been seen in the ND and the discrepancy is accounted for by the estimated systematic uncertainty. There are 214 events observed in the FD against the predicted number of 191.96±13.82(stat.)±21.99(syst.) events. This analysis set 90% CL limits on the angles θ_{24} and θ_{34} and on the matrix elements $|U_{\mu 4}|$ and $|U_{\tau 4}|$. It successfully improved the limit of angle θ_{24} by 4.6° and θ_{34} by 1.4° compared to the previous NOvA analyses. In addition, it produced a quantitative, model-independent measurement of the agreement between the data and the standard three-flavor oscillation prediction through the R ratio. This R-ratio is consistent with the no NC disappearance hypothesis.

The 2019 RHC analysis is an akin analysis to the NOvA 2019 published $\nu_e/\bar{\nu_e}$ analysis [116]. In this analysis, we searched for the evidence of mixing with light sterile neutrinos through measurements of NC disappearance between the ND and FD for antineutrino events. From the 2017 FHC analysis, this analysis has many analysis improvements such as new CVN architecture, separate CVN training for RHC data, Cosmic rejection BDT trained separately for the RHC data, updated systematic uncertainty assessment, and cross section modeling improvements. This "top-up" analysis includes close to 50% more antineutrino data than the previous 2018 result. We predicted 122±11 (stat.)±18 (syst.) NC events at FD and 121 data events were observed. This analysis produced 2D 90% C.L. limits on the angles θ_{24} and θ_{34} and on the matrix elements $|U_{\mu 4}|$ and $|U_{\tau 4}|$. It set a limit for the angle $\theta_{24} < 24.7°$ and angle $\theta_{34} < 31.7°$. The R-ratio calculated is also in favor of the three-flavor oscillation hypothesis. This analysis is unique in the sense that it conducted the first sterile neutrino search using the antineutrino beam from an accelerator.

References

[1] Wolfgang Pauli, "Letter to the physical society of Tubingen", (1930).

[2] O. Hahn and L. Meitner,"Uber eine typische β-Strahlung des eigentlicher Radiums", *Physikalische Zeitschrift*, 10:741-745 (1909).

[3] E. Fermi, "Versuch einer theorie der β-strahlen", *Zeitschrift fÃijr Physik*, 88: 161-177, (1934).

[4] F. L. Wilson, "Fermi's Theory of Beta Decay", *American Journal of Physics* 36, 1150 (1968).

[5] C. Cowan, F. Reines, F. Harrison, H. Kruse, and A. McGuire, "Detection of the free neutrino: A Confirmation", *Science*, vol. 124, pp. 103-104, (1956).

[6] G. Danby, J. Gaillard, K. A. Goulianos, L. Lederman, N. B. Mistry, et al., "Observation of high-energy neutrino reactions and the existence of two kinds of neutrinos", *Phys.Rev.Lett.*, vol. 9, pp. 36-44, (1962).

[7] Konstantin Goulianos, "Experimental Proof of the Existence of Two Neutrinos", *Ph. D. Thesis, Columbia University*, June (1963).

[8] K. Kodama et al.(DONUT Collaboration), "Observation of tau neutrino interactions", *Phys.Lett.*, vol. B504, pp. 218-224, (2001).

[9] S. Schael et al. (the ALEPH, DELPHI, L3, OPAL and SLD Collaborations),"Precision electroweak measurements on the Z^0 resonance", *Phys.Rept.*, vol. 427, pp. 257-454, (2006).

[10] B. Pontecorvo,"Mesonium and anti-mesonium", *Sov. Phys. JETP*, 6:429, (1957).

[11] V. Gribov and B. Pontecarvo, "Neutrino astronomy and lepton charge", *Phys. Lett. B*, 28:493-496, (1969).

[12] Andre de Gouvea., "Neutrinos Have Mass So-What?", *Mod.Phys.Lett. A*19: 2799-2813, (2004).

[13] Ziro Maki, Masami Nakagawa, Shoichi Sakata,"Remarks on the unified model of elementary particles", *Progress of Theoretical Physics*(1962).

[14] Bruce Cleveland, et al., "Measurement of the Solar Electron Neutrino Flux with the Homestake Chlorine Detector", *The Astrophysical Journal*, vol. 496(1), pp. 505-526 (1998).

[15] John N. Bahcall, Carlos Pena-Garay., "Solar models and solar neutrino oscillations", *New Journal of Physics*, 6:63(2004).

[16] John N. Bahcall, Raymond Davis Jr.,"Solar Neutrinos: A Scientific Puzzle", *Science* vol. 191(4224), pp. 264-267 (1976)

[17] John N Bahcall., "Neutrino astrophysics", *Cambridge University Press*, 1989.

[18] V. N. Gavrin et al., "Measurement of the response of a Ga solar neutrino experiment to neutrinos from an 37 Ar source", *Physics of Atomic Nuclei*, vol. 69(11), pp 1820-1828 (2006).

[19] F. Kaether, W. Hampel, G. Heusser, J. Kiko, T. Kirsten., "Reanalysis of the GALLEX solar neutrino flux and source experiments", *Physics Letters B*, 685(1):47-54,(2010).

[20] Takaaki Kajita., "Atmospheric neutrinos and discovery of neutrino oscillations". *Proceedings of the Japan Academy, Series B*, 86(4):303-321 (2010).

[21] R. M. Bionta et al., "Search for Proton Decay into $e^+\pi^0$", *Phys. Rev. Lett.*, 51:27-30 (1983).

[22] R. Becker-Szendy et al., "Electron and muon-neutrino content of the atmospheric flux", *Phys. Rev. D*, 46:3720-3724 (1992).

[23] WWM Allison et al., "Measurement of the atmospheric neutrino flavour composition in Soudan 2", *Physics Letters B*, 391(3-4):491-500 (1997).

[24] "https://www.quantumdiaries.org/2014/03/14/the-standard-model-a-beautiful-but-flawed-theory/".

[25] Giunti C, Kim CW., "Fundamentals of Neutrino Physics and Astrophysics, Oxford University Press (2007)".

[26] C. S. Wu et al., "Experimental Test of Parity Conservation in Beta Decay", *Phys. Rev.*, 105, 1413 (1957).

[27] Ludmil Hadjiivanov, "Neutrino, parity violaton, V-A: a historical survey", *https://arxiv.org/abs/1812.11629v1* (2018).

[28] R. P. Feynman and M. Gell-Mann, "Theory of the Fermi Interaction", *Phys. Rev.* 109, 193 (1958).

[29] A. Salam and J. C. Ward, "Electromagnetic and weak interactions", *Phys. Lett.* 13, 168 (1964).

[30] G Arnison et al., "Experimental observation of isolated large transverse energy electrons with associated missing energy at s=540 GeV" (UA2 Collaboration),*Physics Letters B*, vol. 122(1), pp.103-116 (1983).

[31] M.Banner et al., "Observation of single isolated electrons of high transverse momentum in events with missing transverse energy at the CERN $\overline{p}p$ collider" (UA2 Collaboration), *Phys. Lett. B*, vol. 122(5-6), pp. 476-485 (1983).

[32] B. Pontecorvo, *Sov. Phys. JETP*, 26, 984-988, (1968).

[33] G. Fantini et al., "The formalisam of neutrino oscillations: an introduction", *arXive: 1802.05781v1 [hep-ph]*, page: 32 (2018).

[34] C. Giganti, S. Lavignac, M. Zito, "Neutrino oscillations: the rise of the PMNS paradigm", *Progress in Particle and Nuclear Physics -Elseiver*, vol. 98, pp 1-54 (2018)

[35] C. Giganti, S. Lavignac, M. Zito, "Neutrino oscillations: the rise of the PMNS paradigm", *Progress in Particle and Nuclear Physics -Elseiver*, vol. 98, page-9 (2018)

[36] M. Tanabashi et al. (Particle Data Group), "The Review of Particle Physics (2019)",*Phys. Rev. D*, 98, 030001 (2018) and 2019 update.

[37] V. Barger, et al., "Matter effects on three-neutrino oscillations", *Phys. Rev. D*, 22, 2718 (1980).

[38] Boris Kayser, "Neutrino Physics", *FERMILAB-PUB-05-236-T*, (2005).

[39] J.A. Formaggio, G.P. Zeller, "Neutrino Cross Sections Across Energy Scales", *Rev. Mod. Phys.*, 84, 1307 (2012).

[40] P Anselmann et al. "Solar neutrinos observed by GALLEX at Gran Sasso", *Physics Letters B*, 285(4):376-389, (1992).

[41] JN Abdurashitov et al. "Results from SAGE (The Russian-American gallium solar neutrino experiment)", *Physics Letters B*, 328(1-2):234-248, (1994).

[42] K. Abe et al. (Super-Kamiokande Collaboration), "Solar neutrino results in Super-Kamiokande-III", *Phys. Rev. D*, 83, 052010 (2011).

[43] B. Aharmim et al.(SNO Collaboration) "Combined Analysis of all Three Phases of Solar Neutrino Data from the Sudbury Neutrino Observatory", *Phys. Rev. C*, 88, 025501 (2013).

[44] M. Apollonio et al., "Search for neutrino oscillations on a long base-line at the CHOOZ nuclear power station", *The European Physical Journal C - Particles and Fields*, vol. 27, page-331-374 (2003).

[45] Y. Abe et al., "Measurement of θ_{13} in Double Chooz using neutron captures on hydrogen with novel background rejection techniques", *JHEP*, 01:163, (2016).

[46] J. K. Ahn et al.(RENO Collaboration), "Observation of Reactor Electron Antineutrinos Disappearance in the RENO Experimentn", *Phys. Rev. Lett.*, 108, 191802 (2012).

[47] F. P. An et al.(Daya Bay Collaboration), "Observation of Electron-Antineutrino Disappearance at Daya Bay", *Phys. Rev. Lett.*, 108, 171803 (2012).

[48] Y. Fukuda et al.(Super-Kamiokande Collaboration), "Evidence for oscillation of atmospheric neutrinos", *Phys.Rev.Lett.*, 81, 1562 (1998).

[49] Y. Ashie et al.(Super-Kamiokande Collaboration), "Measurement of atmospheric neutrino oscillation parameters by Super-Kamiokande I", *Phys. Rev. D*, 71, 112005 (2005).

[50] M. G. Aartsen et al.(IceCube Collaboration), "Neutrinos Below 100 TeV from the Southern Sky Employing Refined Veto Techniques to IceCube Data", *Astroparticle Physics*, 116, 102392 (2010).

[51] T. Walton et al.(MINERvA Collaboration), "Measurement of muon plus proton final states in ν_μ interactions on hydrocarbon at $\langle E_\nu \rangle = 4.2$ GeV", *Phys. Rev. D*, 91, 071301(R) (2015).

[52] C. Athanassopoulos et al. (LSND Collaboration), "Evidence for $\bar{\nu_\mu} \to \bar{\nu_e}$ Oscillations from the LSND Experiment at the Los Alamos Meson Physics Facility", *Phys. Rev. Lett.*, 77, 3082 (1996).

[53] A. A. Aguilar-Arevalo et al., "A Search for Electron Neutrino Appearance at the $\Delta m^2 \approx 1\text{eV}^2$ Scale", *Phys. Rev. Lett.*, 98, 231801 (2007).

[54] P. Adamson et al. (MINOS Collaboration),"Improved Search for Muon-Neutrino to Electron-Neutrino Oscillations in MINOS", *Phys. Rev. Lett.*, 107, 181802 (2011).

[55] P. Adamson et al. (NOvA Collaboration), "Constraints on Oscillation Parameters from ν_e Appearance and ν_μ Disappearance in NOvA", *Phys. Rev. Lett.*, 118, 231801 (2017).

[56] "http://www.nu-fit.org".

[57] Rabindra N Mohapatra and Palash B Pal, "Massive Neutrinos in Physics and Astrophysics", *World Scientific Lecture Notes in Physics*, vol. 72 (2004)

[58] G. Karagiorgi et al.,"Leptonic CP violation studies at MiniBooNE in the (3+2) sterile neutrino oscillation hypothesis", *Phys. Rev. D* 75, 013011 (2007); *Erratum Phys. Rev. D*, 80, 099902 (2009).

[59] V.Barger et al.,"Fate of the sterile neutrino", *Physics Letters B*, vol-489 (3-4), pages 345-352 (2000).

[60] A. Aguilar et al. (LSND Collaboration), "Evidence for neutrino oscillations from the observation of $\bar{\nu_e}$ appearance in a $\bar{\nu_\mu}$ beam", *Phys. Rev. D* 64, 112007 (2001).

[61] A. A. Aguilar-Arevalo et al. (MiniBooNE Collaboration), "Event Excess in the MiniBooNE Search for $\bar{\nu_\mu} \to \bar{\nu_e}$ Oscillations", *Phys. Rev. Lett.*, 105, 181801 (2010).

[62] G. Mention et al., "Reactor antineutrino anomaly", *Phys. Rev. D*, 83, 073006 (2011).

[63] W. Hampel et al., "Final results of the Cr-51 neutrino source experiments in GALLEX", *Phys. Lett. B*, 420:114-126, (1998).

[64] J.N. Abdurashitov et al.,"Measurement of the response of a gallium metal solar neutrino experiment to neutrinos from a ^{51}Cr source ", *Phys. Rev. C*, 59, 2246 (1999).

[65] K. N. Abazajian et al.," Light Sterile Neutrinos: A White Paper", *arXiv:1204.5379v1* (2012).

[66] A. A. Aguilar-Arevalo et al. (MiniBooNE Collaboration),"A Combined $\nu_\mu \to \nu_e$ and $\bar{\nu_\mu} \to \bar{\nu_e}$ Oscillation Analysis of the MiniBooNE Excesses", *Fermilab-PUB-12-394-AD-PPD* (2012).

[67] Th. A. Mueller et al., "Improved predictions of reactor antineutrino spectra", *Phys. Rev. C*, 83, 054615 (2011).

[68] G. Mention et al., "Reactor antineutrino anomaly", *Phys. Rev. D*, 83, 073006 (2011).

[69] J. Kopp et al., "Sterile neutrino oscillations: the global picture", *JHEP* 05, 050 (2013), [arXiv:1303.3011].

[70] C. Giunti, T. Lasserre, "eV-scale Sterile Neutrinos", *Annual Review of Nuclear and Particle Science*, Vol. 69:163-190 (2019).

[71] A. Aurisano., "Validating the Approximation of Sterile Appearance", *NOvA Internal Document, DocDB-16140* (2016).

[72] B. Rebel,"General Form of the Unitary Mixing Matrix for 4 Neutrino Mass Eigen-states", *MINOS-doc-4995* (2009).

[73] P. Adamson et al. (MINOS Collaboration),"Search for Sterile Neutrinos Mixing with Muon Neutrinos in MINOS", *Phys. Rev. Lett.*, 117, 151803 (2016).

[74] R. L. Talaga et al., Report No. FERMILAB-PUB-15-049-ND-PPD.

[75] "Specifications of Kuraray wavelength shifting fibers, http://kurarayps f.jp/psf/ws.html".

[76] "The NOvA APD is a custom variant of the Hamamatsu S8550, http://www.hamamatsu.com/us/en/product/alpha/S/4112/S8550-02/index.html".

[77] D. S Ayers et al., "NOvA technical design handbook. Technical report, Fermilab, Batavia, IL", *FERMILAB-DESIGN-2007-01* (2007).

[78] "Accelerator Division - Operations Department",*Concepts Rookie Book, Tech. Rep.*, Fermilab (2013).

[79] P. Adamson et al., "The NuMI Neutrino Beam", *FERMILAB-PUB-15-253-AD-FESS-ND* (2016).

[80] "Fermilab Creative Services", (2018).

[81] J. Evans (MINOS), "The MINOS experiment: results and prospects", *Adv. High Energy Phys.* 2013, 182537 (2013).

[82] C Athanassopoulos et al., "The Liquid scintillator neutrino detector and LAMPF neutrino source", *Nucl. Instrum. Meth.*, A388, pp. 149-172 (1997).

[83] Gary W. Moran,"Locally-Weighted-Regression Scatter-Plot Smoothing (LOWESS): A Graphical Exploratory Data Analysis Technique", *Masters thesis, NAVAL POSTGRADUATE SCHOOL MONTEREY CA* (1984).

[84] Peter Sigmund, "Particle Penetration and Radiation Effects-General Aspects and Stopping of Swift Point Charges", *Springer Series in Solid State Sciences* (2006).

[85] M Baird et al., "Event Reconstruction Techniques in NOvA", *Journal of Physics: Conference Series* 664, 072035 (2015).

[86] M.Baird., "Introduction to Slicer4D", *NOvA Internal Document, DocDB-9127* (2013).

[87] P. Adamson et al. (NOvA Collaboration), "First measurement of muon-neutrino disappearance in NOvA", *Phys. Rev. D*, 93, 051104(R) (2016).

[88] P. Adamson et al. (NOvA Collaboration), "First Measurement of Electron Neutrino Appearance in NOvA", *Phys. Rev. Lett.*, 116, 151806 (2016).

[89] M. Baird., "Technote for the Multi-Hough transform", *NOvA Internal Document, DocDB-8241* (2012).

[90] M. Messier., "Vertex reconstruction based on elastic arms", *NOvA Internal Document, DocDB-7530* (2012).

[91] L. Aliaga-Soplin., "Neutrino Flux Predictions for the NuMI Beamline", *PhD thesis, William-Mary Coll.* (2016).

[92] L. Aliaga et al., "Neutrino Flux Predictions for the NuMI Beam", *Phys.Rev. D*94.9 (2016) [Addendum: Phys. Rev.D95,no.3,039903(2017)], p. 092005.

[93] S.Agostinelli et al., "Geant4–a simulation toolkit", *Nuclear Instruments and Methods in Physics Research Section A*, vol- 506, Issue 3, page- 250-303 (2003).

[94] C. Andreopoulos et al., "The GENIE Neutrino Monte Carlo Generator: Physics and User Manual", *arXiv:1510.05494v1* (2015).

[95] C. Andreopoulos et al., "The GENIE Neutrino Monte Carlo Generator", *Nucl. Instrum. Meth.*, A614:87-104, 0905.2517 (2010).

[96] C. Hagmann, D. Lange and D. Wright., "Cosmic-ray shower generator (CRY) for Monte Carlo transport codes", *2007 IEEE Nuclear Science Symposium Conference Record, Honolulu, HI* pp. 1143-1146 (2007).

[97] M. A Acero et al.(NOvA Collaboration), "Measurement of Neutrino-Induced Neutral-Current Coherent π^0 Production in the NOvA Near Detector", *arXiv:1902.00558v3* (2019).

[98] J.L. Hewett et al.,"Fundamental Physics at the Intensity Frontier", *ANL-HEP-TR-12-25, SLAC-R-991* (2012).

[99] H. Voss et al., "TMVA, the Toolkit for Multivariate Data Analysis with ROOT", *XI International Workshop on Advanced Computing and Analysis Techniques in Physics Research (ACAT)–Proceedings of Science* (2009).

[100] R. Brun and F. Rademakers, "ROOT: An object oriented data analysis framework", *Nul. Instrum. Meth. A*, 389, 81-86 (1997).

[101] Christian Szegedy et al., "Going Deeper with Convolutions", *arXiv:1409.4842v1* (2014).

[102] A. Aurisano at al., "A Convolutional Neural Network Neutrino Event Classifier", *FERMILAB-PUB-16-082-ND, Journal of Instrumentation*11, P09001 (2016).

[103] G. S. Davies et al., "CVN 2018 Technical note", *NOvA Internal Document, DocDB-27467* (2018).

[104] K. Bays,"NOvA cosmic rejection package and algorithms technical note", *NOvA Internal Document, DocDB-11205* (2017).

[105] P. Adamson et al.(NOvA Collaboration), "Search for active-sterile neutrino mixing using neutral-current interactions in NOvA", *Phys. Rev. D*, 96, 072006 (2016).

[106] P. Adamson et al.(NOvA Collaboration), "Measurement of the neutrino mixing angle θ_{23} in NOvA", *Phys. Rev. Lett.*, 118, No-15, 151802 (2017).

[107] Bannanje Nitish Nayak, "Technote: Cosmic Rejection For Detached Bremsstrahlung Showers", *NOvA Internal Document, DocDB-22439* (2017).

[108] E. Sijith.,"Technote: Cosmic Rejection BDT for Nus2018 Analysis", *NOvA Internal Document, DocDB-28703-v3*(2018).

[109] Lisa Goodenough. "Technical Note on the NOvA Beam Monitoring for 2015 Summer Analysis", *NOvA Internal Document, DocDB-13572*

[110] Kanika Sachdev, "Spill Level Data Quality- Technical Note", *NOvA Internal Document, DocDB-12437*

[111] Kirk Bays, "LiveGeometry tech note", *NOvA Internal Document, DocDB-11470-v5*

[112] Susan Lein, "DCM Edge Metric", *NOvA Internal Document, DocDB-13527-v1*

[113] C. Backhouse., "The CAFAna Framework - Technote", *NOvA Internal Document, DocDB-9222* (2014).

[114] M. A Acero et al.(NOvA Collaboration), "New constraints on oscillation parameters from ν_e appearance and ν_μ disappearance in the NOvA experiment", *Phys. Rev. D*, 98, 032012 (2018).

[115] P. Adamson et al.(NOvA Collaboration), "Constraints on Oscillation Parameters from ν_e Appearance and ν_μ Disappearance in NOvA", *Phys. Rev. Lett.*, 118 No-23, 231801 (2017).

[116] M. A Acero et al.(NOvA Collaboration), "First measurement of neutrino oscillation parameters using neutrinos and antineutrinos by NOvA", *Phys. Rev. Lett.*, 123, 151803 (2019).

[117] Adam Aurisano, "Tech Note: 2017 Light Model", *NOvA Internal Document, DocDB-23228-v2* (2017).

[118] Matthew Strait, "Tech note: Muon Energy Scale Systematic", *NOvA Internal Document, DocDB-20816* (2017).

[119] Kirk Bays, "Cross section tuning - Tech Note for 2019 Analyses", *NOvA Internal Document Docdb-36876* (2019)

[120] Ryan B. Patterson, "Summary of neutron studies for conveners meeting", *NOvA Internal Document Docdb-28520* (2018)

[121] Gary J. Feldman and Robert D. Cousins., "Unified approach to the classical statistical analysis of small signals.", *Phys. Rev. D*, 57:3873-3889 (1998).

[122] S. S. Wilks, "The Large-Sample Distribution of the Likelihood Ratio for Testing Composite Hypotheses", *Ann. Math. Statist.*, vol-9, 60-62 (1938).

[123] Alexandre Sousa et al., "Implementation of Feldman-Cousins corrections and oscillation calculations in the HPC environment for the NOvA Experiment", *CHEP 2018 Proceedings.*

[124] G. Mention et al., "Reactor antineutrino anomaly", *Phys. Rev. D* 83, 073006 (2011).

[125] M. Dentler et al., "Updated global analysis of neutrino oscillations in the presence of eV-scale sterile neutrinos", *arXiv:1803.10661 [hep-ph]* (2018)

[126] M. G. Aartsen et al. (IceCube Collaboration), "Searches for Sterile Neutrinos with the IceCube Detector", *Phys. Rev. Lett.*, 117, 071801 (2016).

[127] K. Abe et al. (Super-Kamiokande Collaboration), "Limits on sterile neutrino mixing using atmospheric neutrinos in Super-Kamiokande", *Phys. Rev. D*, 91, 052019 (2015).

[128] M. G. Aartsen et al. (IceCube Collaboration),"Search for sterile neutrino mixing using three years of IceCube DeepCore data", *Phys. Rev. D*, 95, 112002 (2017).